



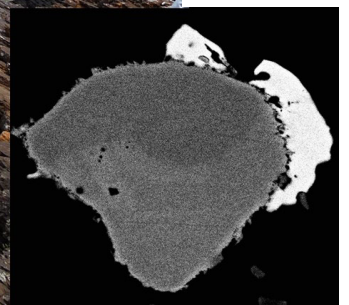
Stockholm
University

Master Thesis

Degree Project in
Geology 60 hp

A Geochemical Investigation of the Port Askaig Ironstones and their Potential for U-Pb-Th Xenotime Geochronology

Patrick Casey



Stockholm 2021

Department of Geological Sciences
Stockholm University
SE-106 91 Stockholm

Abstract

The reappearance of Banded Iron Formations (BIFs) during the Cryogenian (716-535 Ma) after a 1 Ga hiatus and their intimate association with glacial deposits is a crucial line of evidence in the “Snowball Earth Hypothesis” which posits that extreme anoxia developed in the oceans due to a global glaciation and sea ice cover, leading to a buildup of free ferrous Fe in the oceans, which oxidized upon melting of the ice, leading to the brief resurgence of BIFs in the geologic record during the Sturtian glaciation (716-659 Ma).

The focus of this study is on the ironstones and ferruginous diamictites of the Disrupted Beds in the Cryogenian Port Askaig Formation (PAF) of Islay and the Garvellachs, Scotland, and the potential for phosphate group U-Pb-Th to date diagenesis using authigenic xenotime (Y+HREE PO₄). Key data are missing from the PAF, including an absolute date of formation.

Forty two samples of ironstone, ferruginous diamictite and carbonate were analyzed for major and trace elements, and the Fe-rich rocks were compared to other iron formations from the Cryogenian using REE and trace element analysis. The dominant focus of these comparisons is based on the similarities of Cryogenian and older BIFs to the REE trends of modern seawater. The ironstones showed key similarities to Cryogenian and Archean/Paleoproterozoic iron formations as well as modern seawater: positive Gd anomalies, (mean 1.1) superchondritic (>26) Y/Ho ratios (mean 54.6) and depletion of light vs heavy REE. Notably, Cryogenian BIFs lack the positive Eu anomaly ubiquitous to earlier BIFs, which was observed in the ironstones of the PAF (mean Eu/Eu* = .92). A strong positive Ce anomaly was observed in the PAF ironstones, pointing to anoxic conditions during their deposition. REE patterns were also used to determine the source of Fe in the ironstones, which based on the lack of a Eu anomaly pointed to a non-hydrothermal or low temperature hydrothermal source. Hematite in the ferruginous diamictites displayed evidence of diagenetic formation when compared to hematite from other Fe-rich diamictite beds in the PAF based on pore filling morphology and hematite cement between clastic grains. Evidence of Ti mobility during hematite formation in the Disrupted Beds is seen based on hematite/ilmenite solid solution in the hematite of the Disrupted Beds, which is lacking in the Fe-rich diamictites of Member 2 of the PAF. The lack of a hydrothermal signature for the Fe in the ironstones points to possible reduction of Fe sourced from glacial sediments in an anoxic basin that was oxidized upon melting of the ice and introduction of O₂ rich glacial meltwater into the basin. This study concludes that the ironstones in the PAF represent a post-snowball iron formation, evidence of a Sturtian date for formation.

Using scanning electron microscopy xenotime was identified as overgrowths on detrital zircon, an indication of authigenic formation. REE concentrations of 15 xenotime crystals were measured using electron dispersal spectrometry, which demonstrated MREE enrichment, particularly in Dy, Er, and Yb, with depletion in Gd, indications of both a diagenetic and hydrothermal origin, while discounting a metamorphic formation. Chondrite normalized REE patterns of the PAF xenotime demonstrated a trend best fitting diagenetic xenotime observed in other studies based on enrichment in HREE including Lu when compared to hydrothermal xenotime, which demonstrates depletion in Lu. Based on this evidence, the xenotime likely formed during diagenesis, and dating using secondary ion mass spectrometry is expected to provide a date of diagenesis.

Contents

Abstract.....	1
Project background.....	5
Aim of Study.....	5
1. Introduction:.....	6
1.1.1 Onset of a “snowball” Earth.....	6
1.1.2 Global Meltdown.....	7
1.1.3 Constraining the Timing of Snowball Glaciations.....	7
1.1.4 Challenges to the Snowball Earth Hypothesis.....	Error! Bookmark not defined.
1.2 Iron Formations and Snowball Earth.....	8
1.2.1 Iron formation background.....	8
1.2.2 Characteristics of Cryogenian Iron Formations.....	10
1.2.3 REY Properties of Iron Formations.....	10
1.2.4 Formation Mechanisms of Neoproterozoic Iron Formations.....	11
1.3 Geologic background of Islay and the Garvellachs.....	13
1.3.1 Pre-Cryogenian formations.....	13
1.3.2 Cryogenian Stratigraphy.....	14
1.3.3 Age of the Port Askaig Formation.....	20
1.4 Phosphate Group Geochronology.....	21
1.4.1 Phosphate mineral background.....	21
1.4.2 Discrimination of xenotime formation environments.....	22
1.4.3 Dating xenotime.....	23
2. Methods.....	23
2.1 Field methods and sample preparation.....	23
2.1.1 Phosphate mineral analysis.....	24
2.1.2 Electron Microprobe Hematite Analysis Methodology.....	25
3. Results.....	26
3.1 Nomenclature.....	26
3.2 Sample and site descriptions.....	26
3.3.....	29
Islay.....	29
3.3.1 Islay thin section analysis.....	30
3.4 The Garvellach Islands.....	31
3.4.1 Garvellachs thin section analysis.....	34
3.5 Garvellachs Iron Stone.....	35
3.5.1 Garvellachs thin section analysis.....	36

3.6 Hematite petrography.....	38
3.7 Geochemistry of the Islay and Garvellachs Fe formations.....	40
3.7.1 Major oxides	40
3.7.2 Major oxide correlations.....	42
3.8 REY geochemistry	45
3.8.1 REE correlation coefficients.....	48
3.9 Phosphate petrology results	49
3.9.1 Xenotime	49
3.9.2 Monazite.....	50
4. Discussion.....	51
4.1 Background.....	51
4.2 Sedimentology.....	51
4.2 Major Oxides.....	51
4.2.1 Clastic Samples.....	51
4.3.2 Ironstone samples	52
4.2 REE Discussion.....	53
4.2.1 Indicators of seawater origin of REE patterns in the Ironstones.....	53
4.2 Redox conditions during ironstone deposition.....	55
4.2.1 Cerium anomaly	55
4.2.1 U-Mo as an indicator of basin redox conditions.....	56
4.3 Additional REY discussion.....	59
4.4 Diagenetic and Metamorphic Effects on Geochemistry	60
4.4.1 Carbonate diagenesis.....	60
4.4.2 Diagenesis and hematite.....	61
4.5 Model for the formation of the ironstones and ferruginous diamictites of the Port Askaig formation.....	63
4.5.1 Key Observations.....	63
4.5.2 Source of free Fe in the PAF depositional basin	63
4.6 Oxidizing mechanism	65
4.6.1 Sub- ice shelf model of ironstone formation.....	65
4.6.2 Sub ice-sheet model for ironstone formation	68
4.7 Do the Disrupted Beds represent a NIF?.....	69
4.8 Diagenetic or Hydrothermal Origin of Xenotime in the PAF	71
5. Conclusions:.....	75
6. Potential future studies	76
7. Acknowledgements	76

8. Appendices	77
8.1 Whole rock analysis data	77
8.1.1 Major oxide data	77
8.1.2 Trace element data.....	78
8.1.3 REE data.....	79
8.1.4 Anomalies in ironstone and carbonate.....	82
Works Cited.....	83

Project background

The Neoproterozoic Era (1000-541Ma) saw rapid transitions in Earth's climate from warm greenhouse to extreme icehouse conditions with global temperatures dropping to -50°C. Evidence for a pan-glaciation is found in the geological record on every continent, pointing to a worldwide glacial event; the so called “snowball Earth” during which two global glaciations occurred separated by a ~14Ma interglacial: the Sturtian glaciation (717-659Ma) and the Marinoan glaciation (645-635Ma).

The presence of rocks of glacial origin throughout the worldwide stratigraphic record of the late Neoproterozoic was well documented by researchers starting in the 1930s (Hambrey and Harland, 1981). A noted feature of these Neoproterozoic glacial deposits was their incorporation of abundant carbonate clasts into the diamictite as well as the occurrence of carbonate sequences bookending the glacial deposits (Harland, 1964), indicating a rapid transition from warm to cold climate. In the early 1990s these observations, along with a key finding that remnant magnetization of Neoproterozoic glacial rocks from Australia showed that they had been deposited at paleolatitudes near the equator, led Kirshvink (1992) to propose the “Snowball Earth Hypothesis” (SEH) which postulated extreme glaciations during the Neoproterozoic where the entire surface of the Earth was covered in glaciers and the oceans were covered entirely by sea ice for millions of years.

Hoffman et al. (1998) further developed the SEH in their seminal paper in Nature where it was proposed that changes in carbon isotope ratios indicated global scale climate changes leading to a pan-glaciation during which the entire land surface of the Earth was glaciated, and the oceans covered completely by thick sea ice. According to Hoffman et al. (1998) evidence for the snowball theory lay in the presence of this negative ^{13}C isotope anomaly indicating a change in the global carbon cycle, the presence of “cap carbonates” precipitated directly above glacial diamictites, and the reappearance banded iron formations (BIF) after a billion-year hiatus (Hoffman et al., 1998; 2017). Debate over the SEH continues to this day with much focus on whether the Earth was entirely frozen or if unfrozen equatorial waters persisted (Fairchild and Kennedy, 2007; Allen and Etienne, 2008) and on the global synchronicity of the glaciations (Le Heron et al., 2020). Other researchers have suggested that while glaciations did occur during the Neoproterozoic the diamictites represent mass flow events related to tectonically unstable boundaries formed by the breakup of the supercontinent Rodinia through rifting, which occurred roughly synchronously with the onset of Cryogenian (e.g. Eyles and Januszczak, 2004).

The Scottish islands of Islay and the Garvellachs host the Port Askaig Formation (PAF), an extensive and well documented Neoproterozoic glacial succession containing evidence of 28 glacial cycles preserved as glacial diamictites, a cap carbonate and ironstones (Ali et al., 2018). A distinct unit, the “Disrupted Beds” host ironstones and Fe rich diamictites and is located above the “Great Breccia”. The Great Breccia is a diamictite unit believed to represent the hard freeze of the major glacial event and the Disrupted Beds represent the post-glacial melting phase. However, some key data are missing for the PAF including accurate constraints on the time of deposition and geochemical analysis of these Fe rich beds.

Aim of Study

The aim of this study is to investigate the origin of the Fe-formations in the Disrupted Beds of the Port Askaig Formation and to compare the geochemistry of the PAF ironstones and Fe rich

rocks of member 1 and member 2 of the Port Askaig Formation of Islay to other Neoproterozoic iron formations (NIF) Additionally the geochemistry of the iron rich rocks within the Disrupted Beds will be examined to provide evidence about the Cryogenian paleoclimate and the depositional environment including redox state of the PAF. Additionally, this study will investigate the occurrence of the phosphate minerals monazite and xenotime in the ferruginous diamictite of the Garvellachs and Islay and assess their potential to obtain a radiometric U-Th-Pb date for the diagenesis of the Disrupted Beds.

1. Introduction:

1.1.1 Onset of a “snowball” Earth

It is presumed unlikely that there was a single climactic trigger that led to glaciations with the extent of those that occurred during the Cryogenian. Instead several factors acted in concert to cause global changes in the Earth system (Schrage et al., 2002; Hoffman et al., 2017). The precise events that triggered the two global glaciations are still debated, however it is generally believed that a predominance of land surface at low latitudes led to the forcing mechanisms that caused a runaway climate feedback effect. Prior to the initiation of the Sturtian glaciation the continents were arranged as a supercontinent called Rodinia which was beginning to break up via rifting. Evidence from paleomagnetic studies (Li et al., 2007, Li et al., 2013a) indicates Rodinia had been centered at low latitudes (see Fig. 1) and the low latitude arrangement of the continents led to cooling through the increased albedo of the Earth in conjunction with an increase in chemical weathering (Schrage et al., 2002) that led to a CO₂ drawdown. Combined, these two forcing mechanisms are believed to have triggered the snowball glaciations.

The global carbon cycle is primarily driven by volcanic activity and silicate weathering. The chemical weathering process is most effective at tropical latitudes as temperature and precipitation are higher (Berner, 1978), and thus with the Earth's landmass centered at tropical latitudes increased weathering is expected to have occurred during the Neoproterozoic (Schrage et al., 2002; Cox et al., 2016a). An additional factor proposed for the increase in weathering leading to a CO₂ drawdown is the emplacement of a basaltic large igneous province (LIP) related to plume activity during the initial breakup of Rodinia (Cox et al., 2016a). This easily weathered mafic rock would have enabled additional removal of atmospheric CO₂ and may have led to the negative $\delta^{13}\text{C}$ anomaly through the introduction of isotopically light C and additionally provided Fe to the oceans. This increase in weathering thus led to a drawdown in atmospheric levels of CO₂, cooling the Earth.

The Earth receives the highest level of insolation at the equator (1.3w/m²), and the surface of the Earth in the Neoproterozoic had a higher albedo than modern Earth; approximately 0.4 for barren rock and sand (Henderdon-Sellers and Wilson, 1983) as land plants had not yet evolved. Thus a greater amount of solar energy was reflected from the continental landmasses that were centered on the equator, leading to increased cooling due to radiative forcing than would be expected with the modern continental layout.

With the effects of albedo and an increase in chemical weathering working in concert to lower global temperature, glaciers began to form at high elevations near equatorial regions. The formation of glaciers at low latitudes produced a stronger forcing effect on climate than those at a higher latitude due to the higher insolation and the increase in albedo due to ice. Therefore, the cumulative effect of an increase in albedo would be stronger with low latitude glaciation

(Hoffman et al., 2017). The formation of glaciers and ice sheets then led to reduced sea level, which exposed yet more land surface to weathering and to reflect solar radiation back into space, leading to further cooling and glacial advance until the ice sheets reached the critical latitude that led to runaway cooling until the Earth was covered in ice (Schrag., 2002; Hoffman

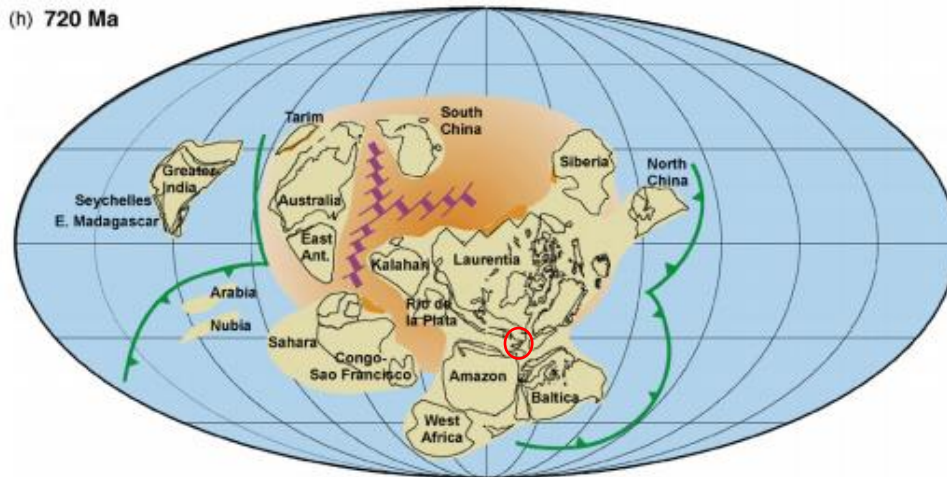


Fig. 1. Configuration of the continents 720Ma with the estimated position of Islay marked by the red circle. (Modified from Li et al, 2007)

et al., 2017).

1.1.2 Global Meltdown

Before the applications of computer models to investigate the Earth system during a snowball Earth, it was assumed that a fully glaciated planet would not be able to recover from total glaciation due to ice-albedo forcing (Hoffman et al., 2017). Kirschvink (1992) proposed that the long duration of the glaciations allowed for volcanic CO_2 to build up in the atmosphere leading to a rapid meltdown of the glaciers. Caldiera and Kasting (1992) estimated that to melt a fully glaciated planet atmospheric ρCO_2 would need to reach 0.12 bar to overcome the effect of ice albedo of a planet-wide glaciation. Due to the complete shutdown of the hydrological cycle, traditional sinks for CO_2 such as carbonate/silicate weathering and atmosphere-sea interaction would not remove CO_2 from the atmosphere as ice and snow do not absorb CO_2 . This allowed for ρCO_2 to build up to high levels after millions of years of volcanic activity with no sink, triggering a runaway greenhouse effect. The melting of a “snowball” Earth is estimated to have been rapid, occurring in only 10-100 kya (Crowley et al., 2001). Melting of the ice enabled calcium carbonate to rapidly precipitate from the water column, forming the cap carbonates, and oxygen was free to oxidize Fe^{2+} that had accumulated in the anoxic oceans, forming BIFs.

1.1.3 Constraining the Timing of Snowball Glaciations.

Geochronology of Precambrian sedimentary rocks is an ever present challenge in geology. The lack of fossils precludes relative dating based on the fossil record and as sedimentary rocks are formed through erosive or chemical deposition, they typically lack newly crystallized minerals such as zircon to provide an accurate date of formation. Intrusive volcanic events can constrain a minimum depositional age, while the presence of extrusive volcanics (i.e. ash and lava flows) interbedded in sedimentary units provide zircon crystals that through U-Th-Pb dating can be used as a geochronometer. The Re-Os dating method has also been applied to Precambrian

organic rich rocks (e.g. Rooney et al., 2011; 2014) providing dates consistent with U-Th-Pb dates from tephra beds. These dates have consistently shown the onset of the Sturtian glaciation at ~716 Ma and deglaciation around 659 Ma. The onset of the Marinoan glaciation is less well constrained and dates range from 650 to 639 Ma and deglaciation occurring around 635 Ma (Hoffman et al., 2017 and references therein). LeHeron et al. (2020) have compiled geochronological data from numerous Neoproterozoic glacial deposits from different continents and identified a trend that may indicate that the glaciations were not synchronous, and occurred at different times on Laurentia and Australia, leading to their proposal that there may have been shifting ice centers on Rodinia throughout the Cryogenian.

1.1.4 Challenges to the snowball Earth hypothesis

The SEH has been challenged by numerous researchers, with some arguing for open equatorial waters based on sedimentary evidence for unfrozen oceans near the equator during the Cryogenian in present day Oman (Allen and Etienne, 2008). Additional alternative explanations for the widespread glacial deposits include the “High Tilt” hypothesis, which posits that extreme obliquity of the Earth focused more sunlight in the polar regions, while low latitudes received less insolation leading to glaciations. The breakup of Rodinia during the late Neoproterozoic coincided with the snowball glaciations. This led Eyles and Januszczak (2004) to propose the “Zipper Rift” hypothesis, which argues that glaciers may have formed on terrain uplifted by spreading centers but that many Cryogenian diamictites interpreted as glacial in origin, including those in Namibia and Scotland, are simply mass flow events from these tectonically uplifted blocks, and iron formation associated with these deposits are products of hydrothermal output due to rifting. Eyles and Januszczak’s work has been criticized by other researchers (e.g. Fairchild and Kennedy, 2007) for dismissing key evidence such as the significance of cap carbonates as evidence for glaciation.

1.2 Iron Formations and Snowball Earth.

1.2.1 Iron formation background

A typical, though not universal feature of Cryogenian glacial deposits from the Sturtian glaciation is the presence of BIFs (alternately Neoproterozoic iron formation (NIF) in the context of the SEH) occurring within the sequence, either intercalated with glacial diamictites or overlaying glacial units (Hoffman et al., 1998; Hoffman et al., 2017; Halverson et al., 2004, Cox et al., 2013). BIFs are defined as a chemical sediment with greater than 15% Fe oxide (Klein, 2005) and commonly thinly layered or laminated, alternating between siliceous layers and Fe rich layers. BIFs are interpreted as the result of an Fe and Si saturated ocean before the presence of free atmospheric O₂ to provide a mechanism for reduction of Fe. The general mechanism proposed for their formation is that the introduction of O₂ in the atmosphere oxidized the free Fe²⁺ causing the oceans to “rust”, forming BIFs (Klein, 2005).

There are three recognized types of BIFs: the Algoma type, which are smallest in size and formed during the Archean through the Neoproterozoic. The Superior type are the largest Fe formations dating to the Paleoproterozoic. The final type is the Rapitan type named after the Rapitan group of Neoproterozoic glacial formations of Canada, and are associated with glacial deposits of the Cryogenian. All three types have been observed in Neoproterozoic stratigraphy (Gaucher et al., 2015), the Algoma type in Wadi Karim of Egypt which have no relation to glacial deposits, (Basta et al., 2011) and a likely Superior type deposit in Shilu, China (Xu et al., 2014). The reappearance of these ancient BIFs in the Neoproterozoic likely points to a return to ferruginous oceans that is possibly related to anoxia due to ice covered seas or changes in ocean chemistry unrelated to glaciation (Canfield et al., 2008; Hood and Wallace, 2015).

Algoma type BIFs first appeared in the geologic record during the Archean, typically found in greenstone belts and are associated with volcanic and hydrothermal activity (Klein, 2005; Gaucher et al., 2015). Algoma type BIFs have a limited lateral extent (<10 km) and thicknesses of <100 m (Kato et al. 2006). Superior type BIFs first appeared in the Paleoproterozoic and are associated with sedimentary units formed along shallow shelves during transgressive events and in isolated rift basins formed from mantle plumes e.g. the Superior Basin. Their lateral extent can be tens to hundreds of km² (Klein, 2005) and provide a major source of iron ore for industry.

The origin of the Superior type has been considered to be the result of an increase in oxygen in the atmosphere as a result of the rapid growth of photosynthetic organisms during the “Great Oxygenation Event” (Klein, 2005). Prior to this, Fe²⁺ occurred as a free ion in the world’s oceans, likely produced from erosion and hydrothermal sources, though the dominant source of Fe has been debated (Isley and Abbot, 1999; Klein, 2005). When free oxygen entered the atmosphere in high concentrations, free Fe²⁺ oxidized to form ferrihydrite, which settled through the water column and accumulated on the sea floor. As the concentration of atmospheric O₂ increased, free Fe²⁺ in the oceans was exhausted and the deposition of large-scale BIFs ceased at approximately 1.8 billion years ago (Klein, 2005). Ferrihydrite has a high adsorption potential and will readily remove phosphate from the water column (Bau and Dulski, 1996), enriching BIFs in phosphate minerals. Ferrihydrites and phosphate also readily scavenge REEs from the water column and sediment pore waters during diagenesis (Rasmussen et al., 1998). These properties mean BIFs provide a record of ocean geochemistry at their time of deposition (Rasmussen et al., 1998; Klein, 2005, Kato et al., 2006). Mineralization of the ferrihydrite to hematite and occasionally magnetite or siderite during diagenesis produced the BIFs (Klein, 2005). Hematite and magnetite in iron formations are resistant to alteration during diagenesis and metamorphism, allowing these formations to preserve their geochemical signal during numerous alteration events (Kato et al., 2006) thus retaining information on Cryogenian conditions.

1.2.2 Characteristics of Cryogenian Iron Formations

Rapitan type BIFs are intimately associated with glacial deposits. They are found overlying or intercalated with glacial diamictites, and often contain evidence of floating ice such as drop stones. Their extent is often limited even when compared to the extent of the glacial diamictites in their host formation indicating that their formation may have been restricted by paleotopography as exemplified in the topographically bound Holowilena ironstone of Australia (Baldwin et al., 2012; Lechte and Wallace 2015). In addition to banded

ironstones, ferruginous diamictites and shales are typical facies of NIFs. The Holowilena Ironstone of Australia (Lechte and Wallace, 2015) and the Chuos formation of Namibia (Lechte et al., 2019) are composed of numerous Fe rich facies pointing to glacial processes occurring during the formation of the BIFs; either a possible glacial re-advance or influx of ice-rafted debris during melting.

1.2.3 REY Properties of Iron Formations

Rare earth element and yttrium (REE+Y) systematics are important tools for determining changes in ocean chemistry and redox state, and in BIFs are believed to record past ocean chemistry (Klein, 2005; Baldwin et al., 2012; Gaucher et al., 2015). REY systematics of the modern ocean are well understood (Lawrence and Kamber, 2006a; Kato et al., 2006; Planavsky et al., 2010) and have been shown to be remarkably similar to paleo-oceans, an indication that the hydrological cycle has been little altered throughout geologic history. Modern seawater is characterized by light REE (LREE) depletion, and enrichment in heavy REE (HREE) with positive La and Gd anomalies and superchondritic Y/Ho ratios (≥ 26) (Zhang and Nozaki, 1996; Bau and Dulski, 1996). The depletion of LREE in marine waters occurs in estuarine environments where these elements are removed through adhesion to organic-metallic particles, thus enriching the HREE relative to LREE in ocean water (Bau and Dulski, 1995; Lawrence and Kamber, 2006).

Algoma and Superior Type BIFs show similar REE patterns with minor depletion in LREE and enrichment in HREE, though an overall flat pattern. Typical features of these types of BIFs are positive Eu anomalies which point to Fe from magmatic hydrothermal sources as hydrothermal fluids are enriched in Eu^{2+} (Klein, 2005). Europium and Ce are used as indicators of oceanic oxygenation. These two elements vary from other lanthanides as they can occur in divalent

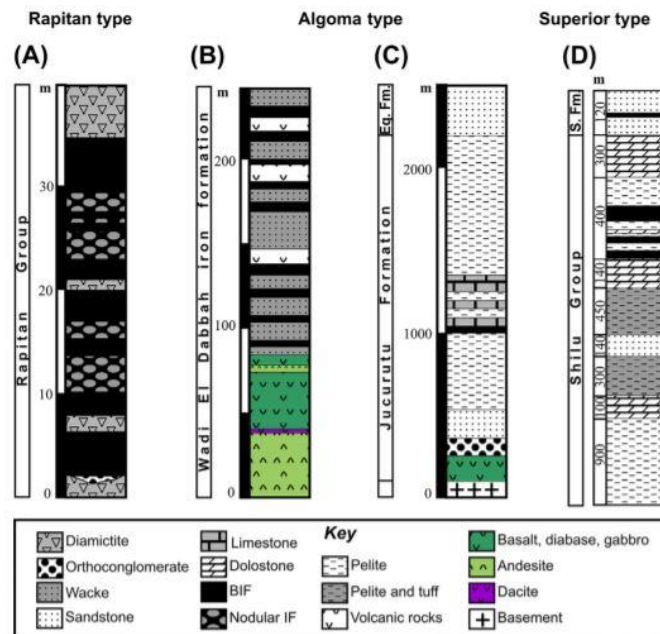


Fig. 2. Typical stratigraphy of the three types of BIFs in the Neoproterozoic. (From Gaucher et al., 2016)

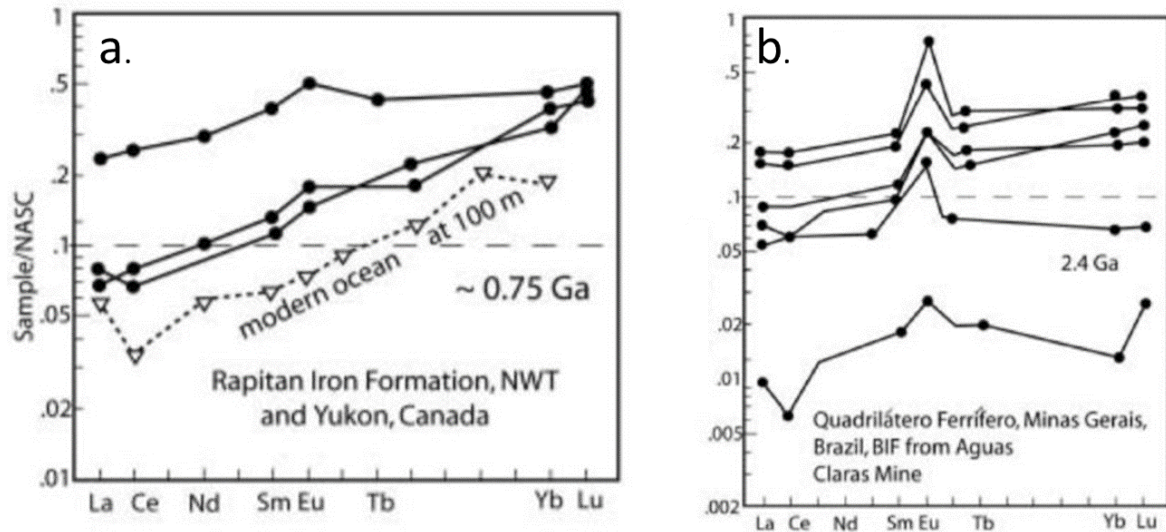


Fig. 3. Comparison of REE patterns between Neoproterozoic (a) and Archean (b) iron formations. Note the lack of distinctly positive Eu values in the Neoproterozoic iron formations. Modified from Klein (2005)

(Eu²⁺) or tetravalent (Ce⁴⁺) states rather than the 3⁺ state of the other lanthanides. Europium 2⁺ originating from hydrothermal vents remained in solution in the anoxic waters of the Archean and Paleoproterozoic. This led to Eu enrichment in sediments such as BIFs when oxygen was introduced (Sverjensky, 1984). Soluble Ce³⁺ oxidizes to Ce⁴⁺, forming CeO₂ which precipitates out of solution in the presence of oxygen. Thus, the later forming Superior type BIFs trend to slightly negative Ce anomalies indicating the beginning of oxidized oceans and show decreasing Eu anomalies, indicating deep ocean anoxia was coming to an end (Kato et al., 2006; Planavsky et al., 2010).

Rapitan type BIFs show a larger magnitude depletion in LREE compared to HREE, giving a steeper trend compared to Algoma and Superior types. Rapitan BIFs tend to show either slight positive or no Eu anomalies. This has been interpreted as potentially indicating a terrestrial source for Fe (Baldwin et al., 2012; Cox et al., 2016b) or a “smoothing” of a distally sourced hydrothermal Eu anomaly by dilution from Eu depleted terrestrial sediments (Klein and Beukes, 1993). Klein and Beukes (1993) and Baldwin et al. (2012) suggest a possible cause for the slightly positive Eu anomalies in some Rapitan BIFs relates to detrital input. They speculate that the anomaly results from plagioclase, as the 2⁺ valence state of Eu allows substitution for Ca²⁺ in the crystal structure, giving plagioclase a positive Eu anomaly that can be reflected in BIFs (Weill and Drake, 1973).

1.2.4 Formation Mechanisms of Neoproterozoic Iron Formations

The hypothesis for the formation of BIFs in the aftermath of the snowball Earth as proposed by Hoffman et al. (1998) reflects the formation of the Superior type BIFs of the Paleoproterozoic. Due to buildup of free Fe²⁺ from hydrothermal sources in an ocean that was isolated from atmospheric-seawater interchange due to total ice cover the oceans became ferruginous (Hoffman et al., 1998; Hoffman et al., 2017). Upon the melting of the sea ice cover, atmospheric oxygen was free to exchange with the anoxic seawater, reducing free Fe²⁺ and precipitating BIFs. Other models of Cryogenian BIF formation suggest Fe²⁺ from hydrothermal vents plays only a minor role and rather terrestrial sourced Fe³⁺ from glacial erosion of continental crust

was reduced by bacteria, producing Fe^{2+} which subsequently oxidized, forming iron-oxyhydroxides close to the glacier grounding line in restricted basins (Baldwin et al., 2012; Gaucher et al., 2015). Oxygen rich meltwater from the ice sheets, and dense oxygenated brines from refreezing of sea ice are a proposed transport mechanism for oxygen into a redox-stratified topographic low, oxygenating the water and oxidizing Fe^{2+} and forming BIFs as shown in Fig. 48 (Baldwin et al., 2012; Lechte et al., 2018).

As noted previously, BIFs are not found throughout the entire Cryogenian record, and are found primarily in the Sturtian glacial strata (Hoffman et al., 2017), though not ubiquitous to these sequences. Few, if any are currently recognized from the later Marinoan (640-635Ma) glaciation. One possible BIF from the Marinoan is the Nantuo formation in China (Ilyvin, 2009) though there is debate regarding the age of this formation, and this BIF is likely to be related to the Sturtian glaciation (Lang et al., 2018).

There are two suggested hypotheses for the lack of BIFs in Marinoan strata: a shorter duration of the glaciation (Halverson, 2004; Hoffman et al, 2017) prevented the buildup of hydrothermal Fe^{2+} in the oceans, and a lack of terrestrial sourced Fe input into the system (Hoffman et al. 2017). The Sturtian glaciation occurred after the eruption of the Franklin Large Igneous Province and Cox et al. (2016b) purposed chemical weathering and glacial erosion of the massive flood basalts would have supplied large amounts of iron to the ocean where it would be reduced to ferrous iron. Halverson (2004) suggested that the increase in sea-floor weathering of MORB due to the break-up of the Rodinia supercontinent, which roughly coincided with the onset of the Sturtian glaciation, would have increased the supply of Fe in seawater. Halverson et al. (2004) suggest that the occurrence of numerous Cryogenian deposits in rift basins provides further support for this hypothesis.

The lack of universal occurrence of iron formations in “snowball” Earth sequences requires close study of the mechanisms of formation and the geochemical properties of the oceans during the Cryogenian. It is possible that due to the non-traditional morphology when compared to earlier BIFs, many Rapitan type BIFs may have been overlooked by studies of snowball Earth deposits. The Port Askaig Formation of Islay and the Garvellachs, Scotland, hosts an example of a potentially overlooked post-snowball ironstone that has only recently received closer attention.

1.3 Geologic background of Islay and the Garvellachs

1.3.1 Pre-Cryogenian formations

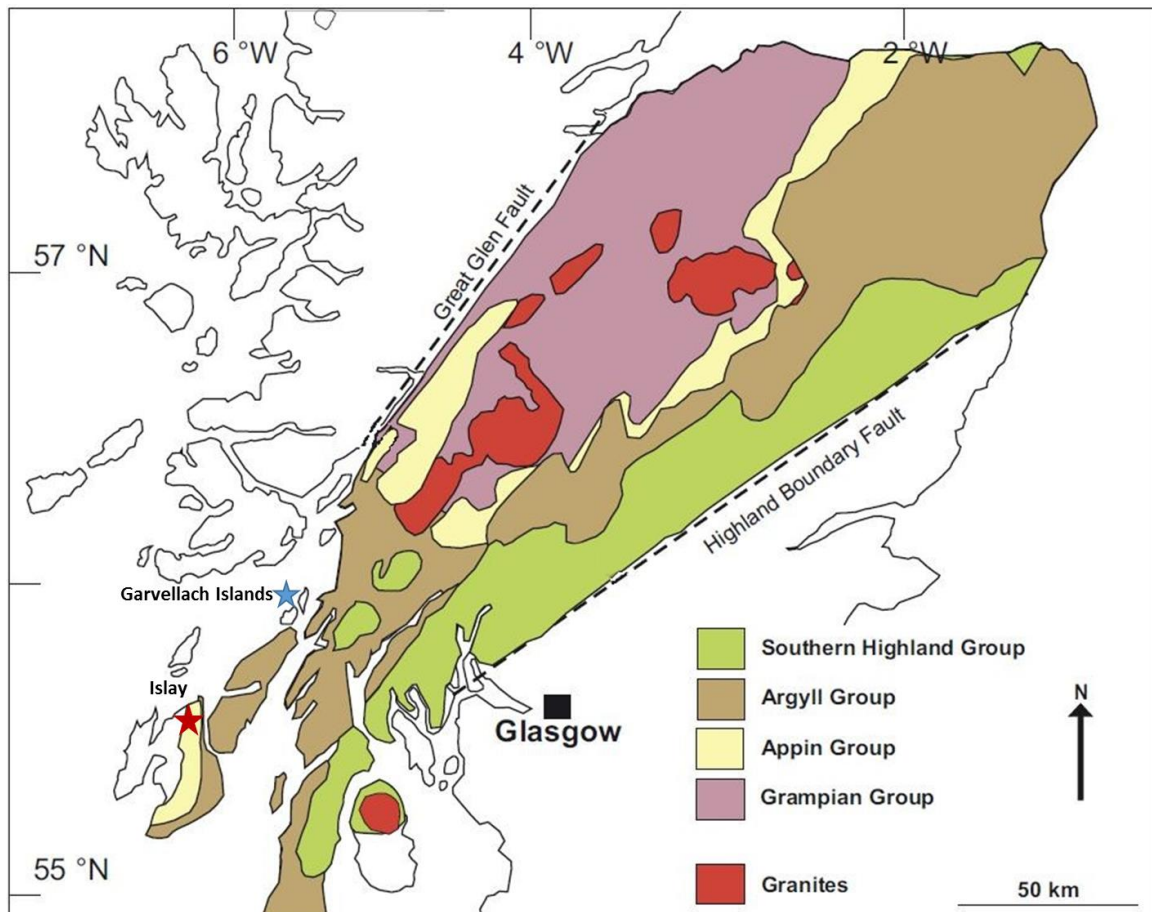


Fig. 4. Map showing the extent of Dalradian Supergroup with Islay and the Garvellachs marked.

Modified from Rooney et al (2011)

The Cryogenian rocks of Islay and the Garvellachs belong to the Dalradian Supergroup, a ~20 km thick sedimentary sequence dating from the Neoproterozoic to the Cambrian deposited on the eastern boundary of Laurentia and metamorphosed to various grades (Beddoe-Stephens, 1990; Skelton et al., 1995). The Dalradian spans the width of mid-Scotland confined by the Highland Boundary Fault and the Great Glen Fault and extends south-west into the northern parts of Ireland. The Dalradian has been interpreted as a rift basin formed during the breakup of Rodina as well as a foreland deepening as a result of the Knoydartian orogenesis.

The bedrock of Islay is part of the Rhinns igneous complex of 1800 Ma, located in southwest Islay. A gap of approximately 1000Ma is represented in the unconformity between the Grampian Group that forms the Colonsay Group and the Bowmore Sandstone, which filled faulted basins, later giving way to the Appin and Argyll group, which were deposited in continental shelf setting. The stratigraphy of the Appin and Argyll group on Islay and the Garvellachs includes the Lossit Limestone (alt. Garbh Eileach formation), with the Port Askaig

Formation (PAF) representing the Cryogenian glacial sequence with the “cap” dolomite of the Bonahaven formation overlain by the Jura quartzite (Webster et al., 2015).

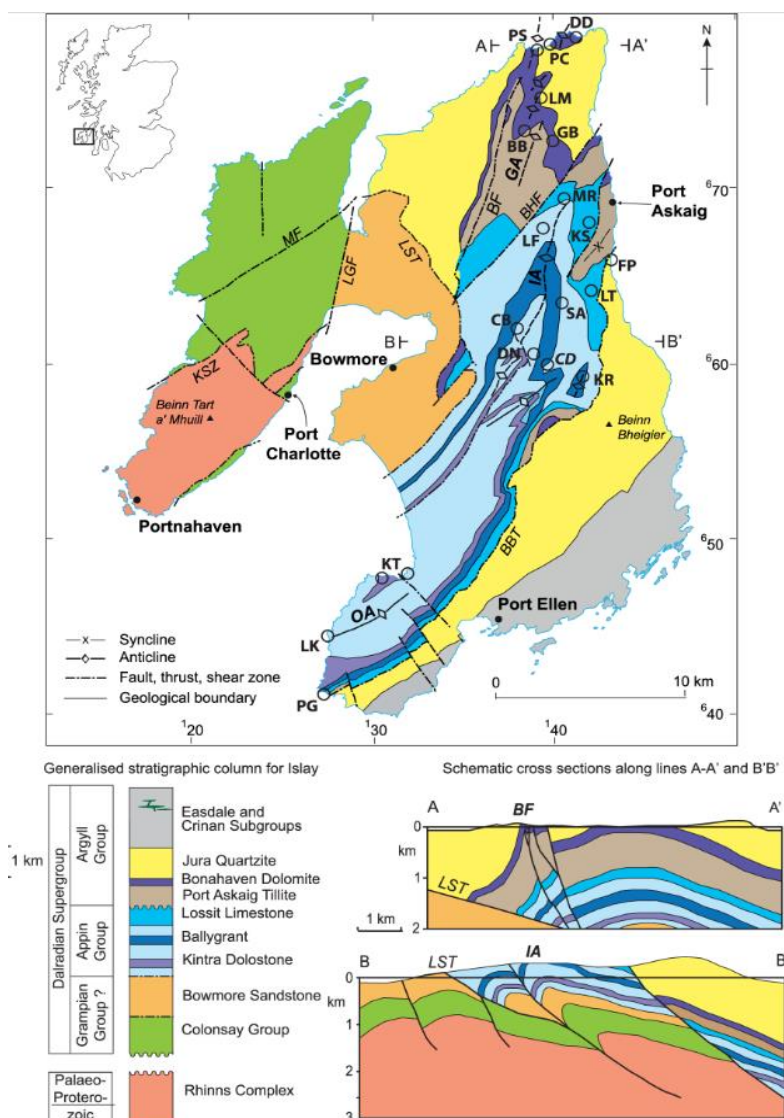


Fig. 5. Geological map of Islay. Modified from Skelton et al. 2015

The Lossit Limestone unconformably underlies the PAF on Islay, and in the Garvellachs the Garbh Eileach Formation, a carbonate unit, conformably underlies the PAF (Fairchild et al., 2011). It is approximately 70 m thick and contains limestone and dolomite. The Lossit Limestone contains oolitic facies and stromatolite fossils, evidence of a warm and shallow depositional environment common to snowball sequences (Hoffman et al., 2017).

The Garbh Eileach Formation records a drop in $\delta^{13}\text{C}$ values, from +10‰ to -5‰, a common geochemical signal found in strata before the onset of the Sturtian glaciation (Hoffman et al., 1998; 2017; Fairchild et al., 2018). The rapid transition from warm water carbonates to glacial diamictites is evidence for a rapid shift from hothouse to icehouse conditions.

1.3.2 Cryogenian Stratigraphy

The PAF was first suggested to be of glacial origin by Thomson (1871) and subsequent work later reaffirmed that supposition (Killburn et al., 1965; Spencer, 1971). Spencer (1971)

identified 5 members of the PAF consisting of alternating carbonate, siliciclastic and diamictite units that show repeated transitions from marine to arid environments as evidenced by evaporite (anhydrite) pseudomorphs, as well as evidence of periglacial processes including sandstone wedges and frost shattered clasts (Spencer, 1971, Fairchild et al., 2018). In total there are 47 recognized diamictites in the PAF believed to record 27 separate climate events (Ali et al., 2018). The Bonahaven dolomite is the uppermost unit of the PAF and is considered to be the cap-carbonate of the Cryogenian sequence as it shows the typical negative Cryogenian $\delta^{13}\text{C}$ excursion, gradually rising to positive values (Fairchild et al., 2018). The Jura quartzite overlays the Bonahaven dolomite and is a several km thick succession of proximal deltaic marine sandstones deposited post-Cryogenian.

Two beds in member 1 (M1) of the PAF are of particular interest for this study, the Great Breccia and the Disrupted Beds. The “Great Breccia” is a carbonate and siliciclastic matrix diamictite unit approximately 50 m thick containing mega-clasts up to hundreds of meters in length (Spencer, 1971; Arnaud and Eyles, 2002), distinguishing the Great Breccia from the other diamictite units of the PAF. The mega-clasts of the Great Breccia show signs of glacio-tectonic deformation. Of these clasts, the most notable is “the bubble”, a large (>100m) dolomite raft on Garbh Eileach interpreted as having been folded by sub-glacial deformation (Benn and Prave, 2006). The nature of the origin of the Great Breccia has been debated. Spencer (1971) along with earlier researchers (Killburn et al., 1965) interpreted the unit as a glacially deposited and glacio-tectonically deformed tillite, with Spencer (1971) comparing it to the Pleistocene Cromer till of Norfolk, England. The current interpretation of the Great Breccia is the representation of the main snowball glaciation, representing a 30 Ma depositional hiatus (Iain Fairchild, personal communication). Other works (Arnaud and Eyles, 2002; Eyles and Januszczak, 2004) argue for a tectonically influenced mass flow along a tectonically unstable rift boundary and discount a glacial origin for the Great Breccia and other diamictite units all together.

The second unit of interest in M1 are the Disrupted Beds. The Disrupted Beds overlay the Great Breccia separated by an approximately 5 m thick dolomite unit on the Garvellachs. The Disrupted Beds are approximately 37 m thick on the Garvellachs and show a limited exposure of only a few meters on Islay. These beds received their name due to soft sediment deformation interpreted as syndimentary (Spencer, 1971; Benn and Prave, 2006). The Disrupted Beds display great heterogeneity over their 37 m thickness on the Garvellach islands, composed of alternating layers of dolostone with dropstones, diamictite, and blue-grey siltstones, and laminated siltstones. Also noted by Spencer (1971) was the presence of “iron ore” bands, thin 2-50 cm magnetite bands near Beannan Buidhe and Dun Bhoraraic on Islay and thicker and more numerous hematite beds on the southern-most island of the Garvellachs. These ironstones were interpreted as detrital magnetite by earlier workers and Spence et al. (2016). Siltstone and dolomite layers in the Disrupted Beds exhibit extensive boudinage (Fig. 7, 8). The interpretation of the deformation as being syndimentary is based on a lack of recrystallization along shear boundaries in thin section (Benn and Prave, 2006) and sandstone dykes originating up-section that cut through the deformed beds (Spencer, 1971). The depositional environment of the Disrupted Beds has been interpreted as both a near-shore marine setting deposited under grounded ice, and as an onshore environment with ephemeral lakes periodically covered by ice (Ali et al., 2018).

Member 2 (M2) of the PAF is situated approximately 100 m above the Disrupted Beds. This unit contains 13 diamictites, of which the two basal units were noted to be exceptionally rich in Fe by Spencer (1971) and shown to contain up to 18% Fe₂O₃ (Dahlgren, 2020). A laminated siltstone rich in Fe is located below D19. Possible ironstone bands were observed in D19 during work in the 1960s (Anthony Spencer, private communication) however these have not been sampled. Periglacial features are observed in these beds including sandstone wedges and frost shattered clasts indicating sub-aerial exposure.

The PAF underwent metamorphism during the Caledonian/Grampian orogeny at upper greenschist facies with peak metamorphic temperatures on Islay found to be between 410-470° C (Skelton et al., 1995) and likely lower further from the Islay anticline. Base metal mineralization (Zn-Pb-Cu) occurred in the Lossit Limestone on Islay during the Carboniferous in the vicinity Ballygrant, including at the sampling site at Beannan Buidhe (Barron and Parnell, 2005).

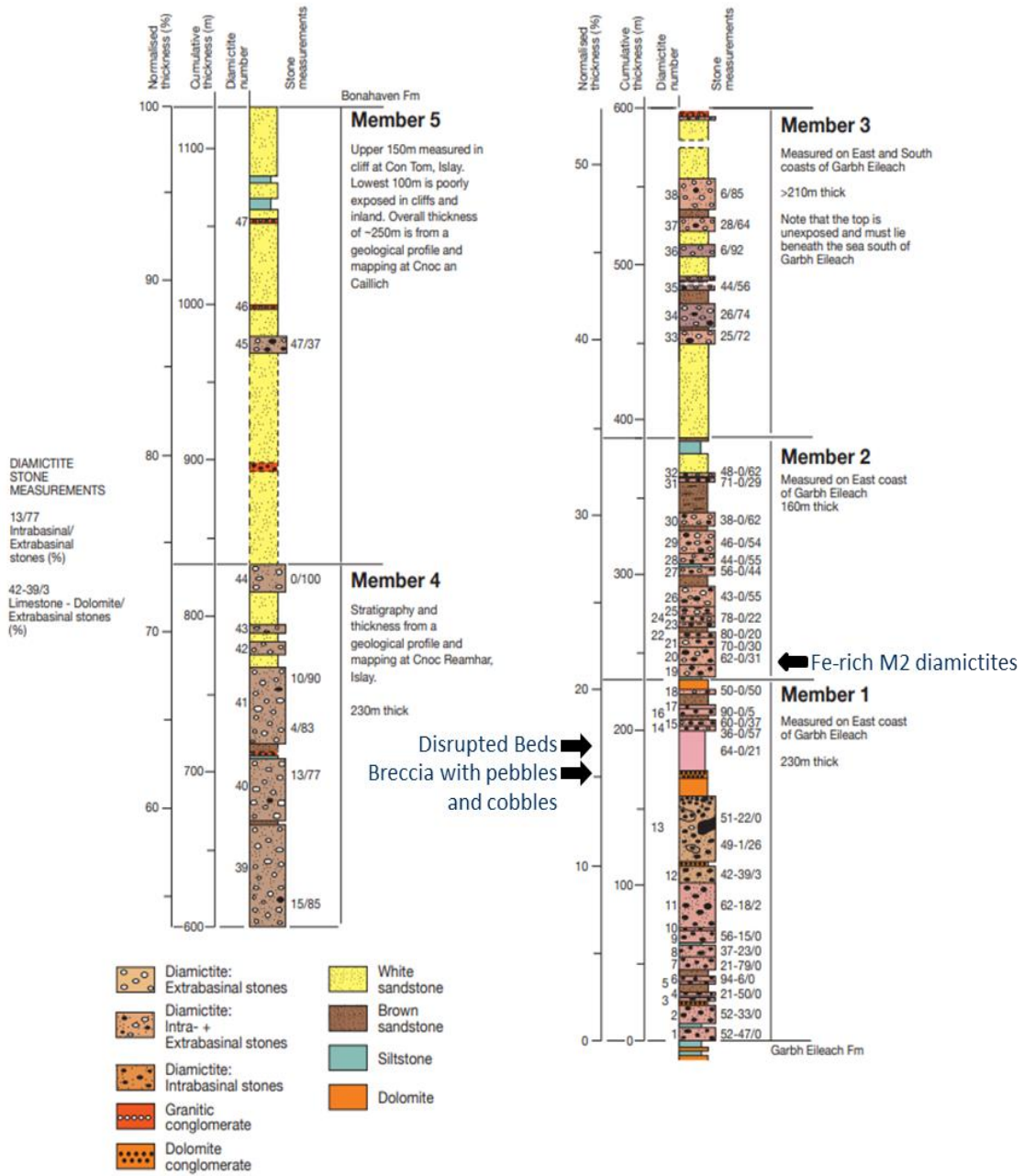


Fig. 6. Stratigraphic log provided by Anthony Spencer of the PAF with sample sites marked.

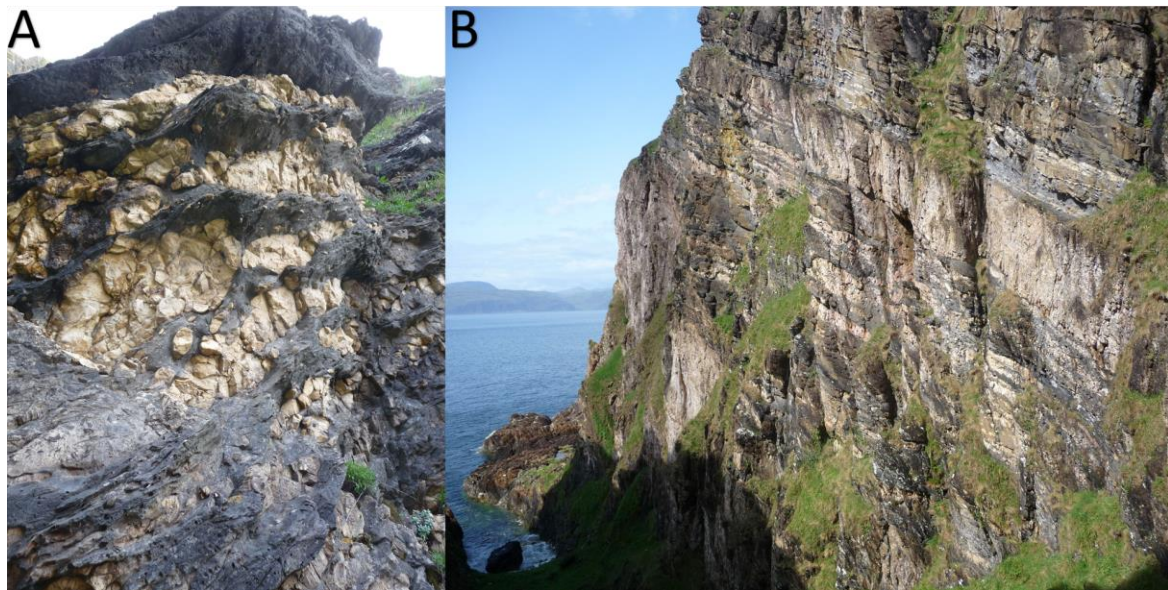


Fig. 7. The Disrupted Beds of Garbh Eileach. A. Boudinaged and fragmented dolomite intercalated with Fe rich siltstone layers. B. View of the Disrupted Beds on a cliff face showing the “disrupted” nature of the sedimentary layers. Photos provided by I. Pitcairn.



Fig. 8. The Disrupted Beds at Beannan Buidhe. The pale orange rocks are dolomite containing drop stones and the dark grey-blue rocks are Fe rich siltstones/diamictite. Photo provided by Alasdair Skelton.



Fig. 9. Dropstone in the siltstone at Beannan Buidhe. Photo provided by David Webster

1.3.3 Age of the Port Askaig Formation

There has been debate over during which of the Cryogenian glacial epochs the PAF was formed. Fairchild et al. (2018) firmly place the PAF in the mid-Sturtian glaciation based on correlation

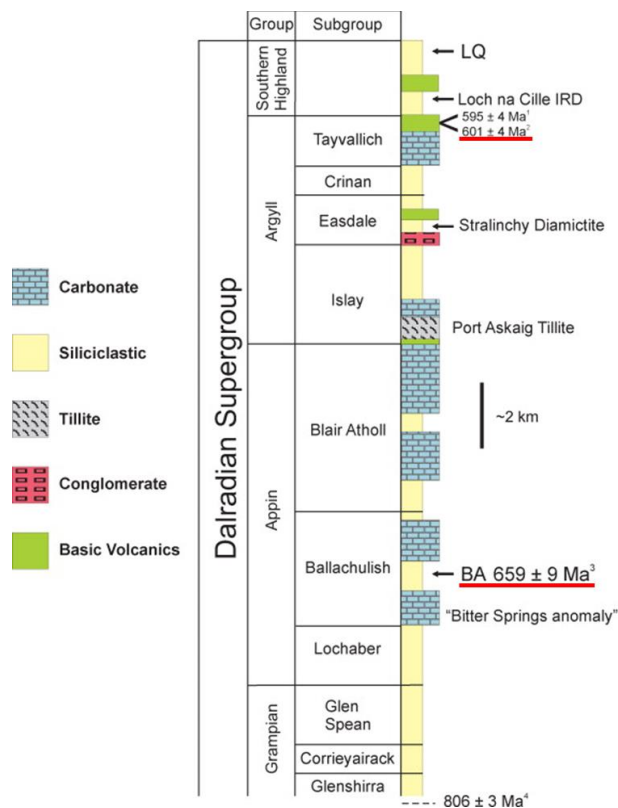


Fig. 10. Stratigraphy of the Dalradian Supergroup showing the dated units underlined in red. Modified from Rooney et al. (2015)

of $^{87}\text{Sr}/^{86}\text{Sr}$ isotope ratios and $\delta^{13}\text{C}$ trends to a dated Sturtian formation in eastern Greenland. The only absolute constraints on the age of the Dalradian Supergroup come from Re-Os dating of the Ballachulish slate of the Appin Group underlying the PAF placing the age at 659 ± 9 Ma (Rooney et al. 2011), and from U-Pb dating of the Tayvallich volcanics of the upper Argyll group which was placed at 595 ± 4 Ma (Halliday et al., 1989) and 601 ± 4 Ma (Dempster et al., 2002). A stratigraphic log from Rooney et al. (2011) in Fig. 10 shows the locations of two dated units of the Dalradian. This log clearly raises questions regarding the interpretation of the correlation of the Dalradian stratigraphy across Scotland, or the interpretation of the PAF as being Sturtian.

As noted previously, the dates of the Sturtian and Marinoan glaciations are fairly well constrained (Hoffman et al., 2017). Numerous studies have placed the onset of Sturtian glaciation at 717.5 to

716.3 Ma and deglaciation occurring 659.9 to 658.5 Ma (Hoffman et al. 2017 and references therein). Therefore, the Re-Os date of the Ballachulish slate dates to the end Sturtian and the slate is situated nearly 5km below the PAF based on stratigraphic correlation. Based on this, Rooney et al. (2011) suggest the onset of deposition of the PAF may have occurred at approximately 650Ma, which correlates to the beginning of the Marinoan glaciation, assuming rapid deposition and accommodation space provided by rifting (Ali et al., 2018). The PAF strongly evidences only one of the two snowball glaciations, interpreted as Sturtian. In the southern most extent of the Dalradian in Donegal, Ireland some glacial deposits and carbonates resembling Marinoan deposits have been observed (Prave et al., 2009) higher in the stratigraphy than the PAF. Prave et al. (2009) correlated these units with deep-water resedimented facies in Scotland, along with evidence of a thin cap carbonate, indicating that the deeper marine conditions prevailed in the Dalradian during the Marinoan, leading to the lack of a record of this later glaciation in Scotland, and thus establishing a relative Sturtian date for the PAF. Direct dating of the PAF using Re-Os or phosphate group geochronology is needed to better constrain the timing of deposition and to firmly establish an absolute Sturtian date for the PAF.

1.4 Phosphate Group Geochronology.

1.4.1 Phosphate mineral background

Phosphate mineral geochronology is a growing method for dating sedimentary rocks (Rasmussen, 2005). The formation of P rich minerals during diagenesis, and their preferential incorporation of U and Th into their structure make them suitable geochronometers for sedimentary rocks. Monazite (Ce+LREE PO_4) and xenotime (Y+HREE PO_4) are phosphate group minerals that are suitable for radiometric dating (Rasmussen, 1998; 2005) with monazite in particular being applied to U-Th-Pb dating, and the use of xenotime geochronology in dating diagenesis is growing (Rasmussen et al., 2010). Both of these minerals are rare earth element (REE) minerals as they readily accept these elements into their crystal structure, as well as U (xenotime) and Th (monazite), while excluding Pb from their lattice. Both minerals have a high closure temperatures, $\sim 1000^\circ\text{C}$ for monazite and 900°C for xenotime (Cherniak, 2006) which prevents Pb loss during low to mid-grade metamorphism.

Monazite is commonly found as an accessory mineral in granites and pegmatites (Chang et al., 1996) and therefore can be found as a detrital component in sedimentary rocks. Monazite is also found in a very-low to low grade metamorphic phase (Rasmussen et al., 2001) and rarely in a diagenetic phase (Evans et al., 2002) and therefore care must be taken to determine which phases are present before attempting to date diagenesis with monazite (Milodowski and Zalasiewicz, 1991; Rasmussen, 2005). Monazite is often dated in conjunction with xenotime as a basis for establishing the diagenetic origin of xenotime, as monazite can constrain low grade metamorphic age (Li et al., 2020).

Xenotime is found in granitic pegmatites and in sedimentary rocks as a detrital component or authigenic growth. Xenotime is isomorphic with the tetragonal zircon which leads xenotime to use detrital zircon crystals as a nucleation point for growth during diagenesis and hydrothermal alteration, though xenotime has also been observed forming on apatite and monazite (Kositcin et al., 2003). Control over the formation of diagenetic xenotime is dependent upon the REE+Y and phosphate budget, porosity of the sediment and availability of substrate (zircon) for formation (Rasmussen, 2005; Aleinikoff et al., 2015.) Xenotime is one of the earliest diagenetic minerals to form as evidenced by xenotime crystals commonly enclosed by silica and carbonate cements in sedimentary rocks (Rasmussen, 2005).

Due to the similar ionic radius to Y, other REE elements, particularly HREEs, readily substitute in the structure during crystallization (Hetherington et al., 2008). Xenotime preferentially incorporates U over Th into its structure, and with the preference for elements with small ionic radii, xenotime is less likely to incorporate Pb into its structure as it forms (Harrison et al., 2002), limiting the presence of initial Pb. Xenotime will however accommodate radio-Pb in its structure as U and Th decay making xenotime an ideal geochronometer (Harrison et al., 2002; Cherniak, 2006).

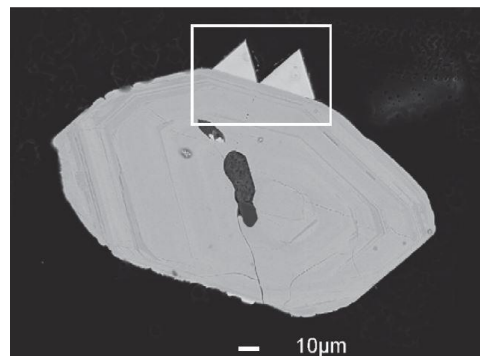


Fig. 11. BSE image of two pyramids of diagenetic xenotime outgrowths on a detrital zircon. From Rasmussen (2004).

Xenotime is chemically and physically stable (Rasmussen, 2005) though it is softer than zircon (4-5) which is evidence for post-depositional growth of euhedral xenotime crystals on zircon (see Fig. 11) as xenotime overgrowths are unlikely to survive abrasion during transport (Rasmussen, 2005). Rasmussen (2002; 2005) observed that during mineral separation and mount preparation xenotime crystals were easily dislodged from host zircon crystals and concluded that diagenetic xenotime is likely to be dislodged from its zircon host during shearing. Therefore, diagenetic xenotime overgrowths are unlikely to survive in rocks that underwent post-depositional deformational events.

Diagenetic and detrital xenotime can be replaced by metamorphic xenotime at temperatures in excess of ~450°C (Rasmussen et al., 2011). Xenotime has been shown experimentally to resist Pb loss at temperatures up to 600°C, though the presence of Na, Ca or F rich fluids caused Pb loss as low as 450°C (Budzyn and Sláma, 2019). The resistance of xenotime to Pb loss at temperatures <600°C (Cherniak, 2006) allows for xenotime to be used for dating diagenesis through upper greenschist to lower amphibolite facies. The response of xenotime to prograde metamorphism has been established experimentally (Cherniak, 2006) as well as thorough studies carried out on Australian conglomerates that have found that xenotime will respond to amphibolite facies metamorphism with dissolution and recrystallization of the outer rim of diagenetic and detrital xenotime, often preserving the original core and age information (Rasmussen et al., 2011).

1.4.2 Discrimination of xenotime formation environments

The use of xenotime in dating diagenesis is hampered by the possibility of a metamorphic origin for the studied xenotime which would provide geologically meaningless data in terms of dating diagenesis (Hetherington et al., 2008). The relatively recent acceptance of xenotime as a geochronometer means there is a relative lack of published analyses of xenotime and in particular discrimination of xenotime origin. Determining the origin of xenotime is thus important before conducting xenotime geochronology. The presence of authigenic xenotime growths on zircon is not 100% diagnostic of diagenetic xenotime (Kositcin et al., 2003). Thus other methods of determining the origin of xenotime include examining the relationship of the xenotime to the cement, as cement overgrowths of xenotime are an indicator xenotime forming during early diagenesis. The presence of compositional zoning, or encapsulation of metamorphic minerals by xenotime is an indication that the xenotime formed during metamorphism and should be determined via examination with SEM and BSE imaging analysis.

One particularly thorough study of multiple origin xenotime in the Witwatersrand basin of South Africa (Kositcin et al., 2003) provides a potential method of discriminating between xenotime of igneous-detrital, diagenetic or hydrothermal origin. Using EPMA Kositcin et al. (2003) identified subtle variations in REE geochemistry, and variations in U/Th ratios between xenotime of different origins (McNaughton and Rasmussen, 2018). Igneous xenotime is characterized by strong negative Eu anomalies as a result of fractionation of Eu in the melt into feldspar phases. Diagenetic xenotime typically shows a slight negative Eu anomaly, while hydrothermal xenotime shows no or very small anomalies and thus Eu enrichment compared to igneous and diagenetic xenotime.

The substitution of Y with M+HREE is common in xenotime of all origins with several weight percent of Y substituted primarily by Dy, Er, Yb, Nd and Gd. Kositcin et al. (2003) and

Aleinikoff et al. (2015) identified Dy as the dominant substitution for Y in igneous and diagenetic xenotime, while Gd was the dominant substitution in metamorphic xenotime. Hydrothermal xenotime, particularly in base metal deposits, shows more ambiguous REE signals that can make differentiating it from diagenetic xenotime a challenge. While Kositsin et al. (2003) and Lan et al. (2013) identified Gd as the primary substitution for Y in hydrothermal xenotime, other studies (e.g. Rasmussen et al., 2007; Aleinikoff et al., 2012; Lan et al., 2019) have demonstrated that both Gd and Dy can be the dominating Y substitution in hydrothermal xenotime making this a less useful diagnostic criterion than that between diagenetic and metamorphic.

The concentration of HREE has been shown (Vallini et al., 2005; Lan et al., 2013; 2019) to be a more useful method of discrimination of hydrothermal and diagenetic xenotime, where hydrothermal xenotime has lower HREE concentrations, particularly of Lu, giving normalized REE concentration charts a steeper right dipping pattern compared to diagenetic xenotime. The mechanism behind these differing REE fractionations is poorly understood, however it has been proposed that dissolution of apatite during metamorphism provides an additional source of MREE (Hetherington et al., 2008) for xenotime formation while HREE removed and fractionated into garnet (Aleinikoff et al., 2015)

Uranium concentrations are an additional useful discriminator between hydrothermal and diagenetic xenotime, where hydrothermal xenotime shows significantly lower U concentrations (<100-500ppm), particularly in low to moderately saline fluid environments compared to diagenetic xenotime.

1.4.3 Dating xenotime

TIMS, and LCP-IMS can be used for xenotime geochronology for larger crystals (Rasmussen, 2005), however the small size of diagenetic and hydrothermal xenotime (>20 μ m) necessitates the use of secondary ion mass spectrometry (SIMS) or sensitive high resolution microprobe (SHRIMP) to measure in situ samples of xenotime. Xenotime, unlike monazite and the traditional zircon geochronometer (with the exception of high U zircons), suffers from severe matrix effects due to variations in composition throughout each measured xenotime crystal (Fletcher et al., 2000; 2004; Cross and Williams, 2018). This matrix effect means that the founding assumption of SIMS U-Pb analysis that emitted secondary Pb/U ions and true Pb-U ratios in the sample and standard are identical is not valid (Cross and Williams, 2018). Matrix effects in xenotime are caused by variations in U, Th, Σ REE and possibly the orientation of crystallographic planes in the unknown and standard. Therefore the use of reference samples with known composition is needed for accurate dating. The current lack of homogeneous xenotime standards necessitates the use of electron microprobe analysis (EPMA) to determine U, Pb, Th and Σ REE of each measured site in the standard and unknown sample (Fletcher et al., 2004; Cross and Williams, 2018).

2. Methods

2.1 Field methods and sample preparation

Field mapping and sampling were carried out on Islay and the Garvellachs islands in spring 2019. Samples were taken of Fe-rich formations of the Disrupted Beds at Beannan Buidhe on Islay. At the Garvellachs samples were taken of the Fe-rich diamictites, ironstones and the carbonate units of Disrupted Beds (see Fig. 17)

Samples of approximately 30g were cut by diamond saw at Stockholm University and sent for crushing and milling by ALS Sweden. Whole rock analysis of the prepared samples was carried out by ALS in Galway, Ireland using lithium metaborate fusion ICP for major oxide and ICP-MS for trace elements. Reference standards MRGeo08, OREAS 102a, OREAS 503c, OREAS 905, GBM 908-10 and AMIS0304 were used for trace element and REE calibration, SY-4, OREAS 102a and AMIS0304 for major element and GS310-7 and GS311-3 for C and S, as well as blank glass disks were used for the calibration of the instrument, giving an accuracy of within 1-3%. Duplicate samples were run of G11, Is-1, G6, G5b, G14, G15, G22, G30 and G30a to test precision, giving results within 1%. Samples were normalized to the UCC of Kamber et al. (2005)

Thirty polished thin sections were prepared by Vancouver Petrographics, Canada and observed under plane and cross polarized light to determine the petrology of the samples. Rock chips were prepared and mounted in 25mm epoxy mounts and polished for scanning electron microscope analysis. Thin sections and epoxy mounts chosen for SEM and EPMA analysis were vacuum coated with carbon at NRM using BAL-Tech CED 030 carbon evaporator at 10^{-2} mbar yielding a .2 micron coating.

2.1.2 Phosphate mineral analysis

Thin sections and rock chips were analyzed using a FEI Quanta FEG 650 scanning electron microscope and mineral chemistry was analyzed with an Oxford Instruments X-max 80mm 2 electron dispersal spectrometry (EDS) detector calibrated to a cobalt metal standard. Additional mineral identification was conducted using a Hitachi TM4000 tabletop SEM.

Xenotime and monazite were identified using BSE and the EDS detector and cut from thin sections using an ultrasonic cutter and plugs were cut from the epoxy disks and remounted in epoxy mounts along with standards for further analysis. Rare earth element, U, P, Si, O and Th EDS analysis of xenotime and monazite from the PAF was conducted using 40s counting times on multiple targets along the profile of each xenotime and monazite crystal. Results were normalized to the chondrite of Sun and McDonough (1989).

Ten EDS measurements were conducted on 10 grains of the monazite standard MNZ 44069 (Delaware) from the Wilmington Complex, with a U-Pb ID-TIMS age of 424.9 ± 0.4 Ma (Aleinikoff et al., 2006). These results were then averaged and compared to the average results of EPMA analysis of the same monazite standard conducted by Rubatto et al. (2014). The EDS results were within 1σ of the EPMA data, indicating good reliability for the EDS analysis (See table 1).

Element	Rubatto 2014 EPMA	EDS (this study)	Difference(%)
O	27.57	27.15	1.55
Si	0.08	0.16	100.54
P	13.62	12.69	6.83
Ca	0.57	0.64	10.59
Y	2.28	2.24	1.80
La	9.76	11.07	13.46
Ce	21.83	23.24	6.45
Pr	3.13	2.72	13.02
Nd	12.39	11.11	10.39
Sm	2.26	2.38	5.06
Eu	0.40	0.35	13.14
Gd	1.97	1.85	6.10
Dy	0.89	0.94	6.09
Th	2.07	3.36	62.56
U	0.38	0.38	0.15

Table 1. EDS analysis results of monazite standard MNZ44069 compared to those from Rubatto et al. (2014) with difference between analysis shown. Si in the monazite standard were at or below

2.1.3 Electron Microprobe Hematite Analysis Methodology

Ten grains of hematite >30µm were selected from thin sections from the Disrupted Beds and M2 of the PAF and analyzed for Fe content for use as an internal standard for LA-ICP-MS analysis on the JXA-8530F JEOL Superprobe electron microprobe analyzer at Uppsala University. The mineral grains were analyzed for Fe and Ti with a count time of 20 seconds. Titanium represented a common accessory phase in the hematite, and analysis of Ti in addition to Fe provided total analytical values between 98-101.4% for total element weight which was considered to be the range of reliable results from the analysis.

3. Results

3.1 Nomenclature

For the purpose of this study, any non-clastic sample >15% Fe is referred to as ironstone. Diamictite samples above the average shale value of 5% (Taylor and McLennon, 1985) are classified as “ferruginous diamictite”. BIF will be used to refer to Fe formations as a whole, while NIF (Neoproterozoic iron formation) will refer specifically to Cryogenian Fe formations as is generally accepted in current literature. So in this study, the references to the Disrupted Beds unit, which do not meet the definition of a formation, as established by the North American Commission on Stratigraphic Nomenclature (2005), as an iron formation is used solely as a descriptor of the beds in their similarities to other iron formations (*sensu* James, 1954; Trendall, 1983)

3.2 Sample and site descriptions.

Thirty samples from the Disrupted Beds of the Garvellachs islands and six from Islay were collected and analyzed.

Four thin sections from other Fe rich beds from M1 and M2 were obtained from Martin Dahlgren to determine REE patterns of hematite and magnetite.

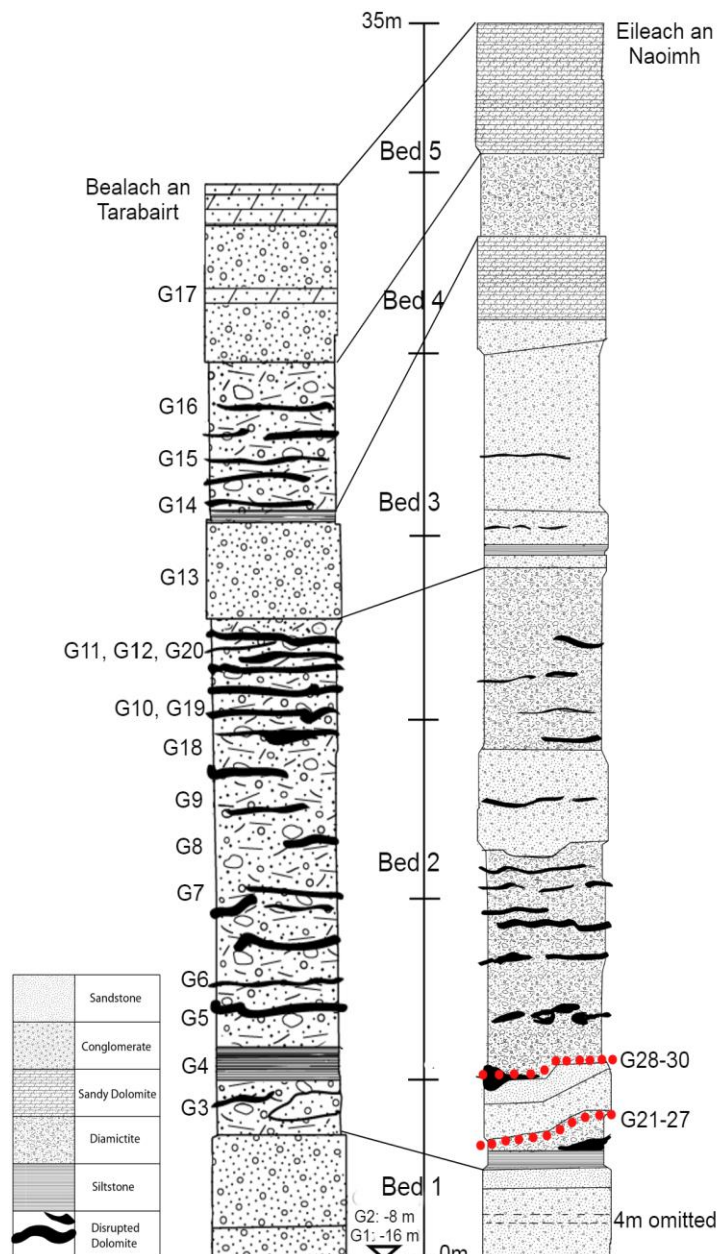


Fig. 12. Stratigraphic columns of the sample sites on the Garvellachs. Redrawn after Spencer (1971) with sample locations indicated. Red dotted line = ironstone bands. Each tick represents 5 m.

Table 2. List and description of samples collected for this study. TS = thin section made, WRA = whole rock analysis conducted. Clastic samples with analyzed clasts are denoted with ‘A’ (diamictite) and ‘B’ (clast)

Garbh Eileach Samples N56° 14' 42.1" W005° 46' 06.2"	
G1	Main Dolomite unit roughly 16m under lowest ferruginous diamictite WRA
G2	Main Dolomite 8m under lowest ferruginous diamictite WRA
G3	A. First ferruginous diamictite in sequence. Layered greyish with red dolomite siderite veins. Signs of graded bedding visible. TS+ WRA Fig. 18C;19;27B B. Carbonate layer 10cm above
G4	Pale grey laminated siltstone with dropstones TS+ WRA Fig. 18A;20
G5	A. Fe-oxide diamictite with dolomite clasts TS+ WRA Fig. 18C; 21; 27A. B. Large dolomite clast TS+WRA
G6	Ferruginous diamictite formation with clasts TS+WRA
G7	A. Ferruginous diamictite with large carbonate clast TS+WRA B. Large carbonate clast TS+WRA
G8	Ferruginous diamictite with granite clasts TS+WRA
G9	Dolomite layer
G10	Massive fine ferruginous diamictite with clasts TS+WRA
G11	Ferruginous diamictite 1m above G10. Mostly carbonate clasts WRA
G12	Dolomite clast from beside G11 WRA
G13	1 st coherent dolomite unit.
G14	Fine Grained ferruginous diamictite above first coherent dolomite WRA
G15	Final ferruginous diamictite TS+WRA
G16	Ferruginous diamictite with carbonate/clastic matrix TS+WRA
G17	Carbonate matrix diamictite with crystalline clasts and pyrite WRA Fig. 18D.
G18	Blue siltstone with clasts TS+WRA
G19	Clastic ferruginous diamictite below zone of large dolomite blobs TS+WRA
G20	Coherent fine grained blue siltstone WRA

	Eileach an Naoimh Samples N56° 12' 59.5" W005° 49' 04.3"
G21, 21a-22-23a-23b-24-25-26	Ironstones. G23b (Fig. 24A.) and G26 (Fig. 24B.) contained abundant siderite veins TS+WRA
G27	Ironstone from upper layer of ironstone formation WRA TS+WRA
G28	Iron oxide layer with unknown structure at layer boundaries WRA Fig. 23D.
G29	Fe oxide breccia TS+WRA Fig. 26.
Gaa	Ironstone collected from south coast of Eileach an Naoimh by Alasdair Skelton TS+WRA Fig. 18B;25A+B.
Gab	Ironstone collected from south coast of Eileach an Naoimh by Alasdair Skelton TS+WRA
G30	Upper most ironstone sample WRA
	Islay Samples N55° 48' 25.23" W 6° 7' 54.23"
IS1	Siltstone collected from Beannan Buidhe, Islay TS+WRA Fig. 14.
IS2	Siltstone collected from Beannan Buidhe, Islay TS+WRA Fig. 14; 29C.
IS3	Siltstone collected from Beannan Buidhe, Islay TS+WRA Fig. 15.
IS4	Siltstone collected from Beannan Buidhe, Islay TS+WRA Fig. 29D.
DL-01-19a	Siltstone collected from Beannan Buidhe, Islay by David Webster WRA
DI-02-19b	Siltstone collected from Beannan Buidhe, Islay by David Webster WRA
	Dahlgren Samples N56° 14' 07.00" W005° 45' 07.40"
19-G-45	Ferruginous Diamictite (M2) D19 Fig. 22;28A
19-G-46	Ferruginous diamictite D20 (M2) Fig. 28B.
19-IS-43	Breccia with pebbles and cobbles (M1) Islay. Fig 29A+B.

3.3 Islay

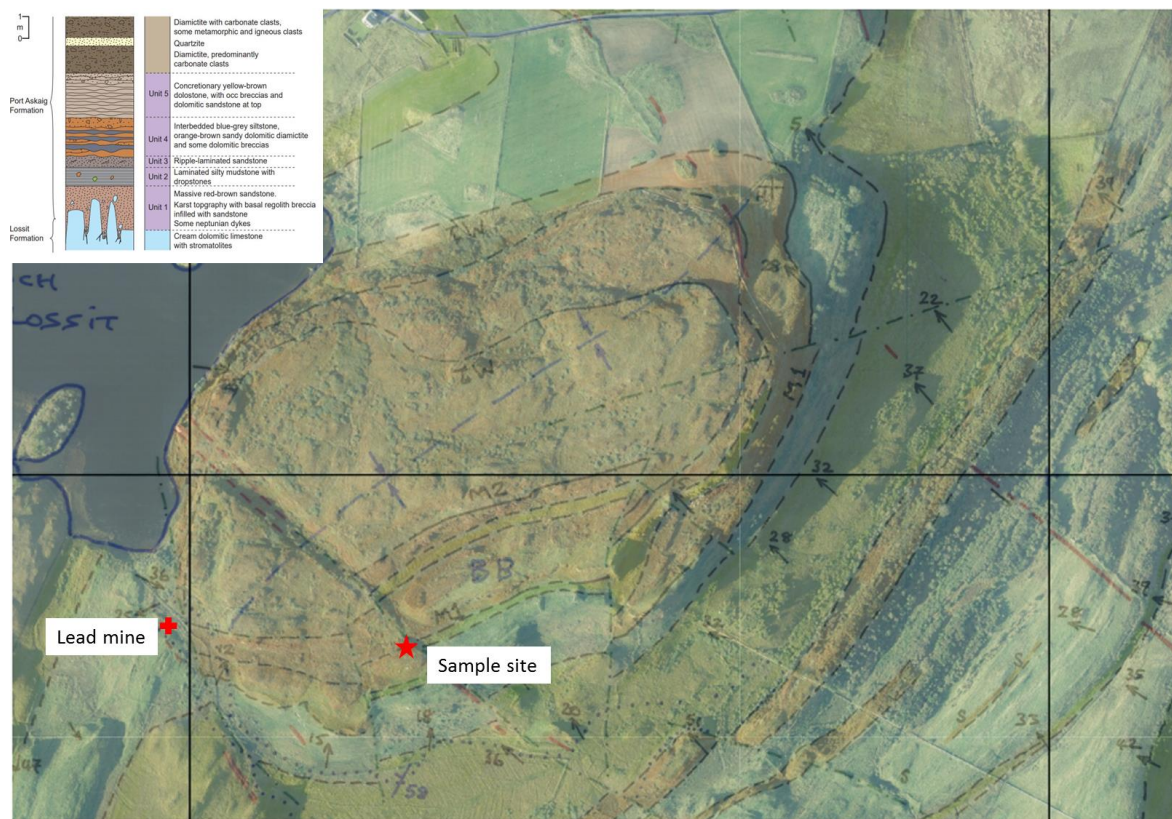


Fig. 13. Beannan Buidhe aerial photo with stratigraphy overlay and stratigraphic column. Grid overlay British Ordnance Survey (1km²). Provided by Ian Fairchild and Anthony Spencer. Stratigraphic column of Beannan Buidhe by David Webster.

Sampling on Islay was conducted at Beannan Buidhe, an exposure of approximately 5 m of the Disrupted Beds located near Ballygrant, Islay close to Loch Lossit. The exposure of the PAF at this location is truncated, missing the lower diamictites of member 1 including the Great Breccia, and rests unconformably on the Lossit Limestone (see stratigraphic column in Fig. 13). The lower units of M2 are also exposed at this site. The Disrupted Beds at this site alternate between pale orange dolomite and iron rich grey-blue layers that are referred to as a siltstone in literature and will be referred to as such here (Spencer, 1971; Arnaud and Eyles, 2002; Benn and Prave, 2006). Boudinage like structures can be observed in the disrupted dolomite bodies that were described in previous works as syndepositional deformation (Spencer, 1971, Benn and Prave, 2006).

The Islay siltstones are a fine grained pelitic unit containing macroscopic dolostone and occasional crystalline clasts at the base of each unit, fining upwards with some evidence of lamination visible (Fig. 14.). Some of the large clasts at Beannan Buidhe are interpreted as dropstones based on deflection of laminae (see Fig. 9). In thin section the siltstones show a fine texture with abundant sub-rounded to sub-angular quartz grains. EDS analysis of the samples identified hematite and goethite as the predominant Fe phases. Biotite and chlorite were not readily apparent in thin section and were only identified with EDS analysis, indicating greenschist facies metamorphism. The siltstone contains elevated levels of phosphate when compared to UCC (see section on geochemistry) and phosphate minerals are common. Phosphate phases are predominantly apatite with minor monazite, goyazite and xenotime.

Xenotime is predominantly found as overgrowth on detrital zircon (see Fig. 26a), indicating authigenic formation. Kaolinite is present likely indicating weathering post-dating metamorphism based on its association with biotite.

3.3.1 Islay thin section analysis

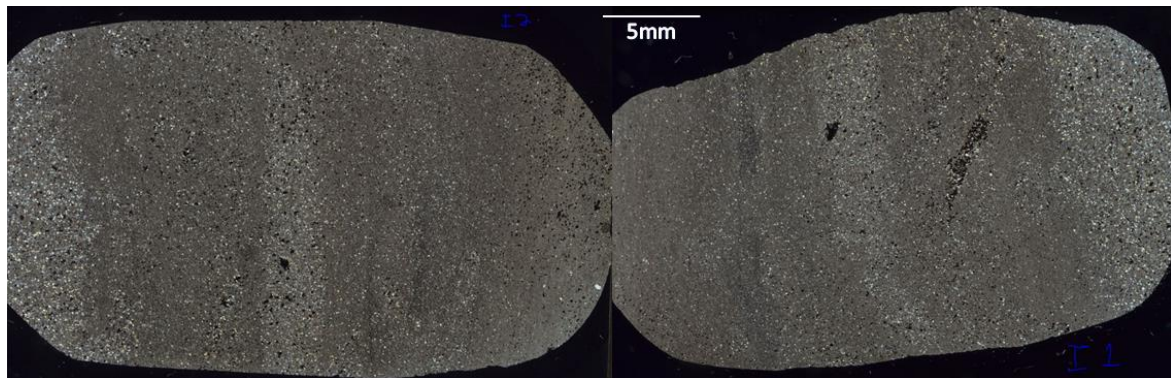


Fig. 14. Thin section scans of siltstone sample IS1, IS2 showing apparent lamination throughout the siltstone beds.

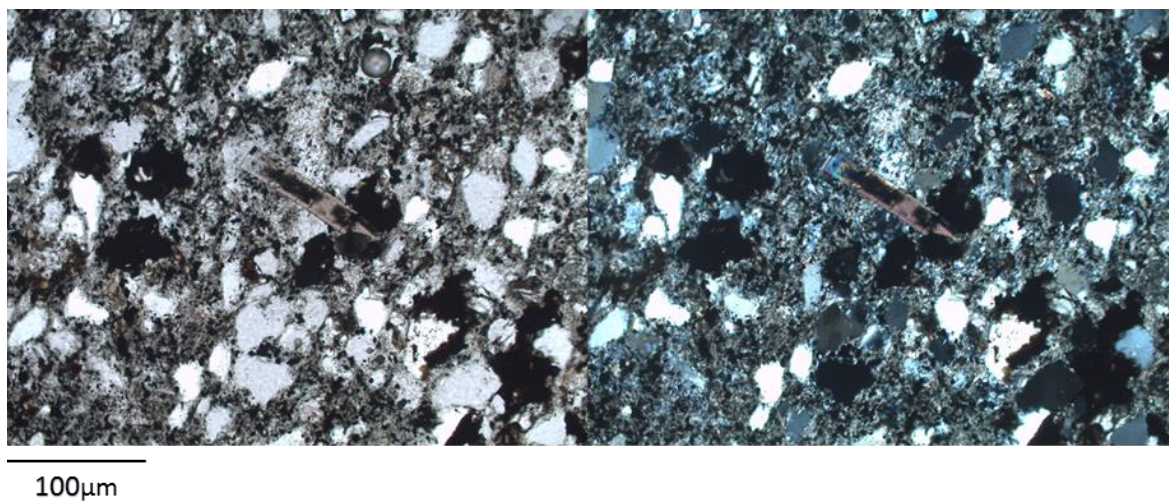


Fig. 15. Thin section of siltstone IS3 from Beannan Buidhe with subrounded quartz grains and euhedral tourmaline crystal.

3.4 The Garvellach Islands

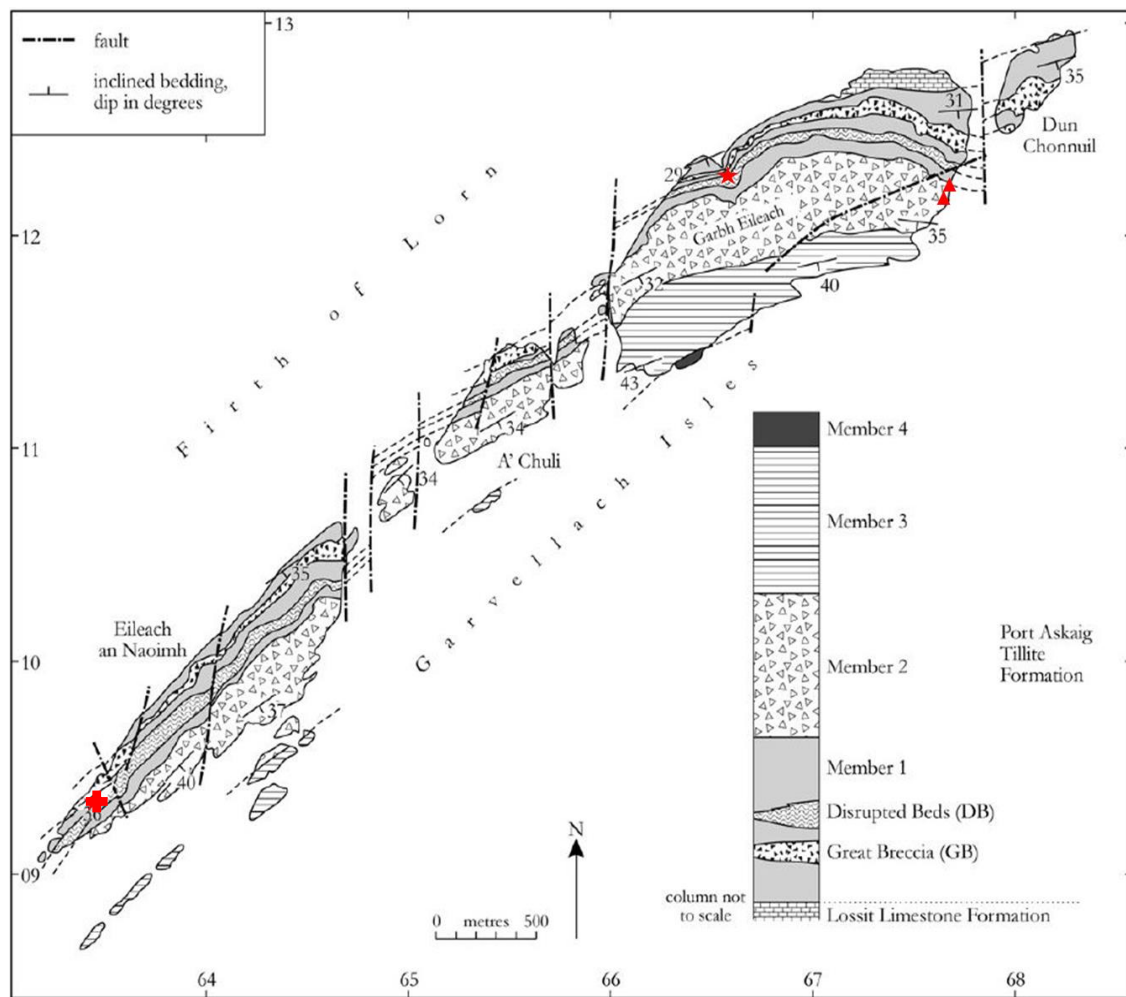


Fig. 16. Map of the Garvellachs showing the sample sites at Bealach an Tarabairt (★) and Eileach an Naoimh (⊕) M2 sample localities marked with (▲). Modified from Benn and Prave (2006)

Samples collected from the Garvellach islands included dolostone, laminated siltstone, diamictite, ferruginous diamictite and ironstone. The samples were taken from the Disrupted Beds at Bealach an Tarabairt on the island of Garbh Eileach, and the ironstone samples were collected on Eileach an Naoimh (see map in Fig. 16). Additional samples were collected from Fe rich diamictites in M2 by Martin Dahlgren in 2019 and are compared with the Fe rich diamictites of the Disrupted Beds.

Bealach an Tarabairt is a gully with well exposed outcrops of the Disrupted Beds. The samples from Bealach an Tarabairt were collected along the stratigraphy starting at the Main Dolomite bed approximately 8 m below the Disrupted Beds, and moving upwards through beds to the upper dolomite of the unit (See Fig. 17). Sampling consisted primarily of the ferruginous diamictite and carbonate clasts.



Fig. 17. Sampling sites at Bealach an Tarabairt with sample locations marked. Photos provided by Iain Pitcairn.

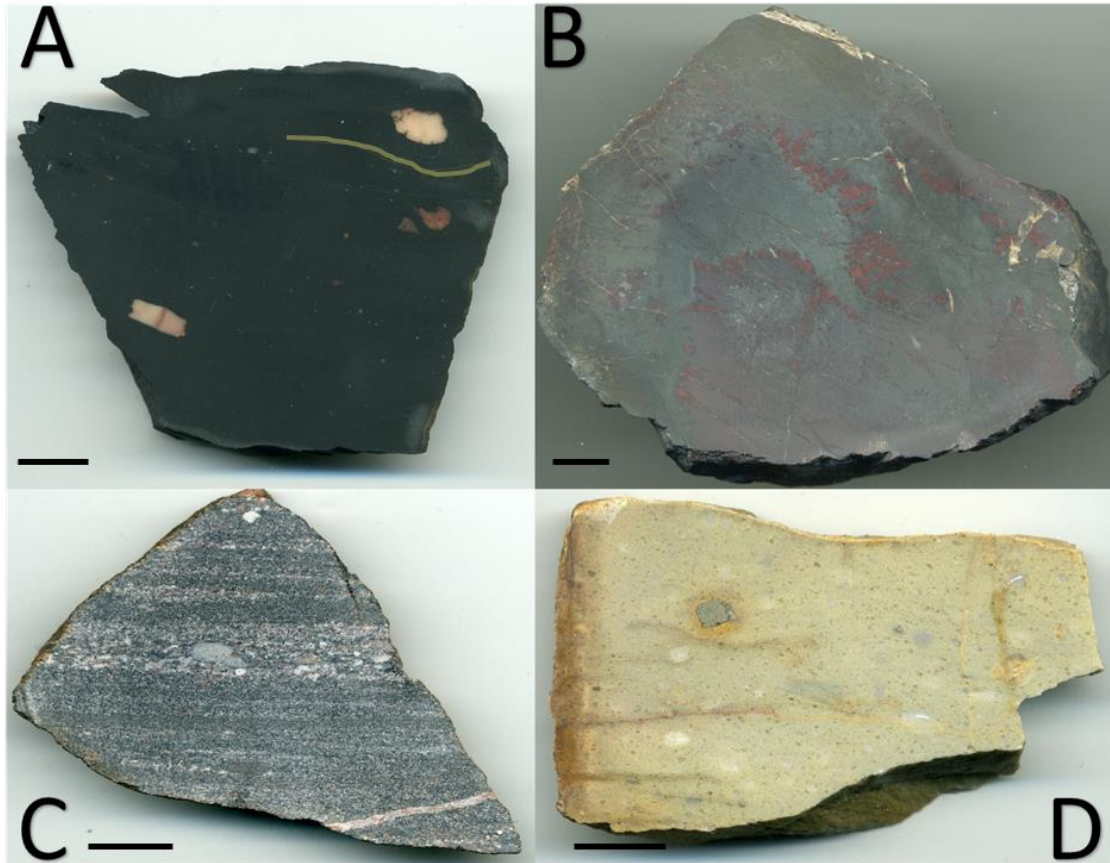


Fig. 18. Images of hand samples taken from the Garvellach Islands. A. Laminated siltstone G4 with rafted clasts (line traces deflection in the laminae). B. Ironstone from Eileach an Naoimh showing lack of banding. Grey=hematite, red = jasper. C. Lowest diamictite G3 showing stratification and upwards fining with sharp erosional contacts. D. Dolomitic diamictite with carbonate and crystalline clasts. Note the large euhedral pyrite crystal. Scale bars = 1 cm.

The ferruginous diamictites of the Disrupted Beds on the Garvellachs are supported by a hematite rich matrix. The hematite crystals are typically anhedral often filling pore space, and occasionally enclose other minerals, particularly ilmenite, similar to the Islay samples.

Clasts are predominantly composed of carbonate, with the abundance of crystalline clasts increasing up section. EDS analysis showed the dominant metamorphic mineral was illite with minor muscovite. Deformational structures are observed in thin section and hand sample with evidence of shear of the matrix around the clasts and till pellets interpreted to be glacio-tectonic in origin based on mesoscale observations of glaciotectonism in the Disrupted Bed diamictites (Spencer, 1971; Eyels and Eyels, 1996). Evidence of metasomatic fluid flow can be observed along grain/ clast boundaries where muscovite and illite have been formed.

BSE and EDS analysis of the ferruginous diamictites showed abundant phosphate minerals, including apatite, goyazite, monazite and xenotime. Similar to the Islay samples, most xenotime is present as overgrowths on detrital zircon, with some lone xenotime crystals with hematite inclusions observed. One clear rounded detrital xenotime grain $>40\mu\text{m}$ was observed (see Fig. 36B). The Ce-carbonate bastnäsite was also observed in several samples.

3.4.1 Garvellachs thin section analysis

Presented below are a selection of thin sections prepared from the Garvellachs samples from Garb Eileach and Eileach an Naoimh

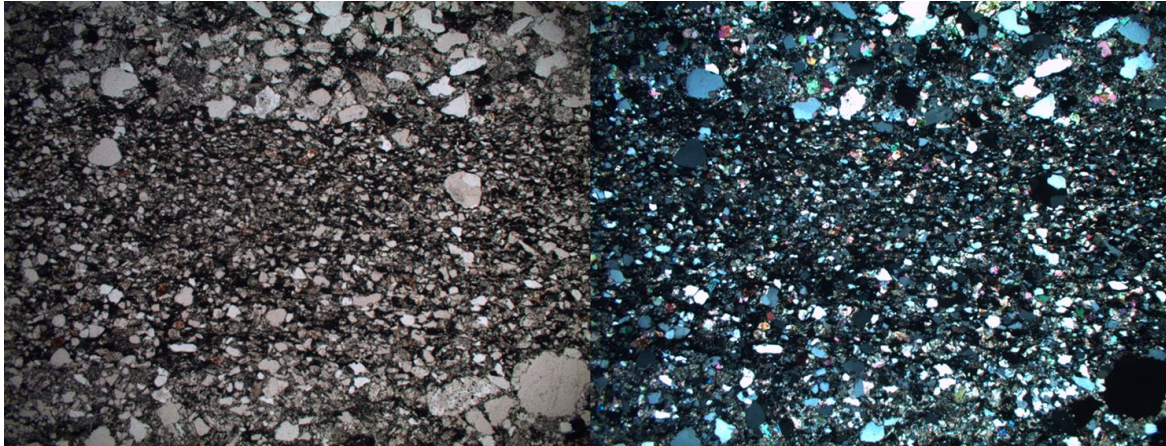


Fig. 19. Thin section in PPL and XPL of the bedding in sample G3, the lowest diamictite sample from the Disrupted Beds showing graded bedding with a coarsening upwards sequence and sharp contacts.

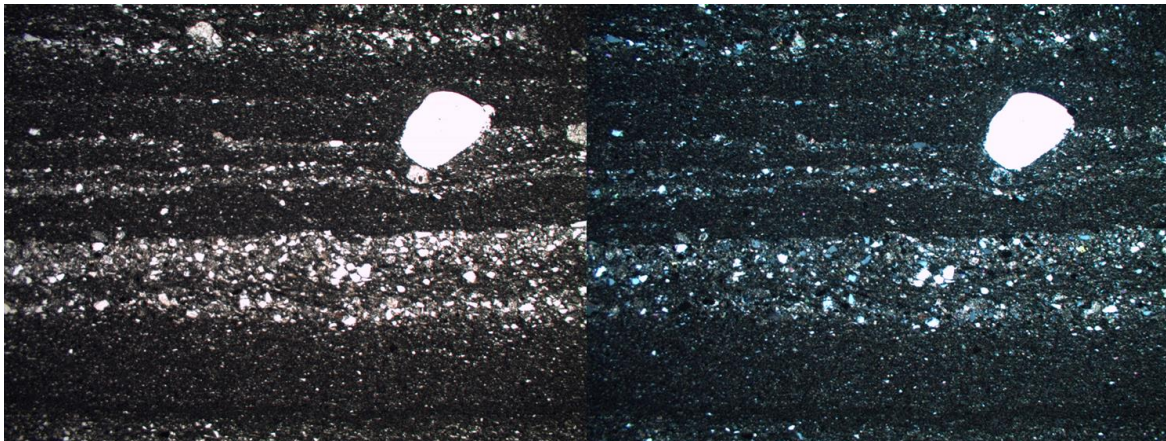


Fig. 20. Thin section in PPL and XPL of bedding in siltstone sample G4 showing fine laminations with an outsized clast interpreted as a dropstone based on deflection of underlying layers.

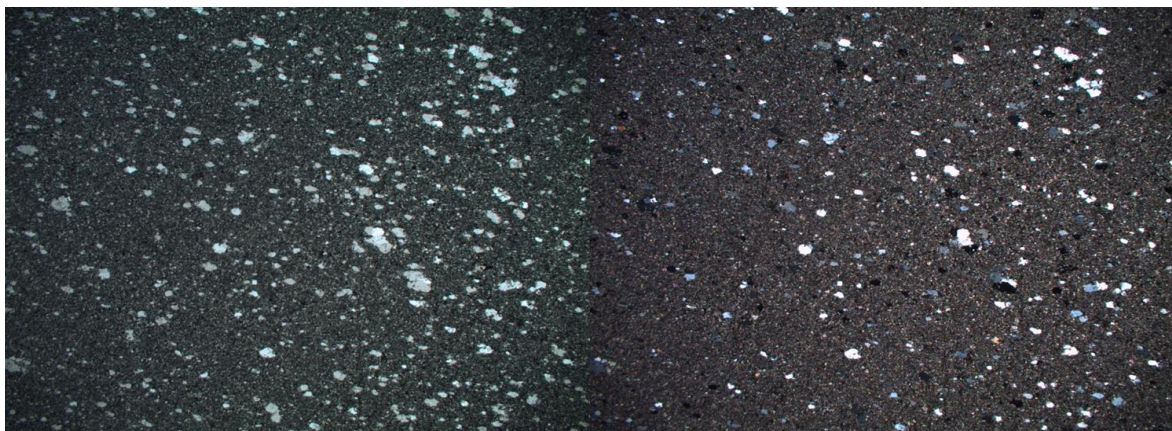


Fig. 21. Thin section in PPL and XPL of sample G5, the first unstratified diamictite. Note the lack of bedding in the sample.

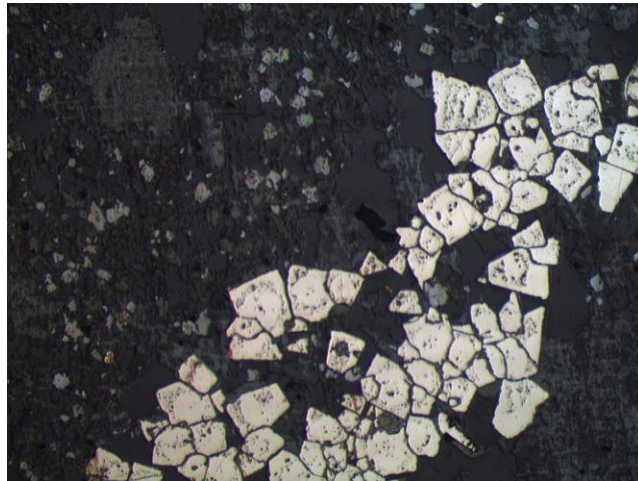


Fig. 22. Euhedral pyrite crystals from D19 in reflected light of M2 from the Garvellachs.

3.5 Garvellachs Iron Stone

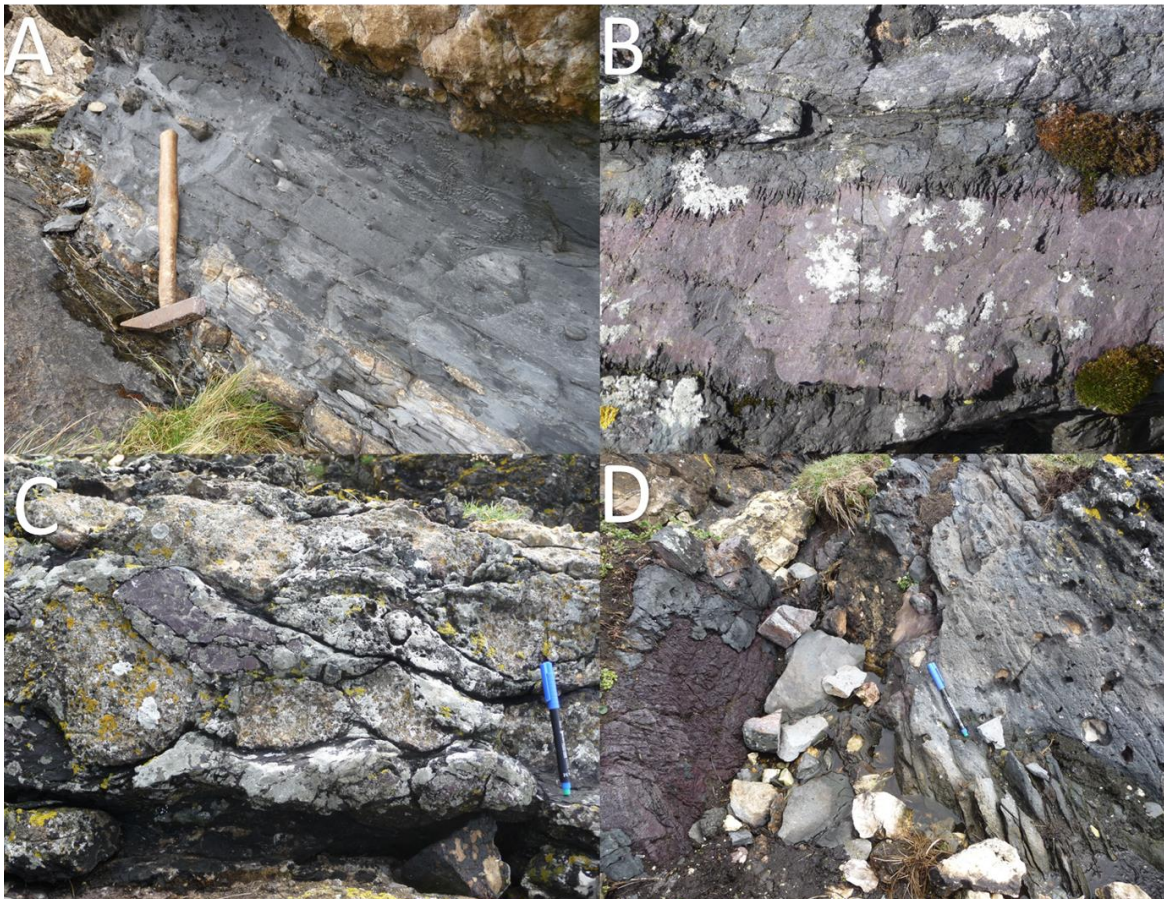


Fig. 23. Ironstones at Eileach an Naoimh. A. Iron rich siltstone with dropstones B. Ironstone in contact with ferruginous diamictite showing a reaction texture of unknown origin C. Podded Fe stone approximately 3 m above main ironstone beds. D. Contact between ironstone and ferruginous diamictite

Ironstone samples were collected from a locality on the south-western coast of Eileach an Naoimh. The ironstone units consist of two sets of thin beds between 5 cm to 50 cm with approximately 3m between the major beds (See stratigraphic column in Fig. 12). The ironstones occur in a sequence of the blue siltstones (Fig. 23A), and are bounded by coherent dolomite units. The layers appear to pinch and swell throughout the beds. The uppermost ironstone bed is an Fe-oxide matrix breccia. Occasional irregular “podded” and deformed ironstones are observed, as seen in Fig 23C and the cartoon in Fig. 49. The ironstone is predominantly composed of hematite with minor quartz, dolomite veins.

Large euhedral hematite and occasional siderite crystals are observed in relation to these veins, showing recrystallization of Fe-oxides (see Fig. 24). Banding is not readily apparent at outcrop scale, or in hand sample, but can be observed in thin section (see Fig. 25B). BSE showed microplaty hematite composing the dominant Fe mass of the samples and EDS analysis of the ironstones showed hematite as the dominant Fe phase. Apatite is the dominant phosphate mineral with the Sr-Al phosphate goyazite abundant in numerous samples, with minor monazite present. Neither xenotime nor detrital zircon were observed in any of the ironstone samples.

3.5.1 Garvellachs thin section analysis

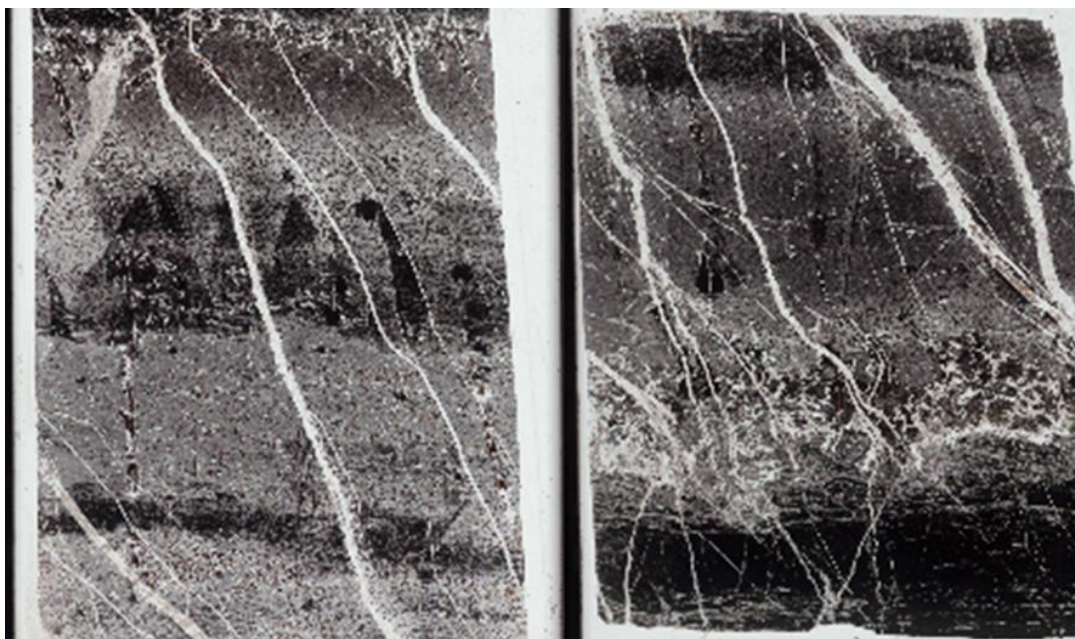


Fig. 24. Thin section scans of ironstones showing banding and carbonate veining.

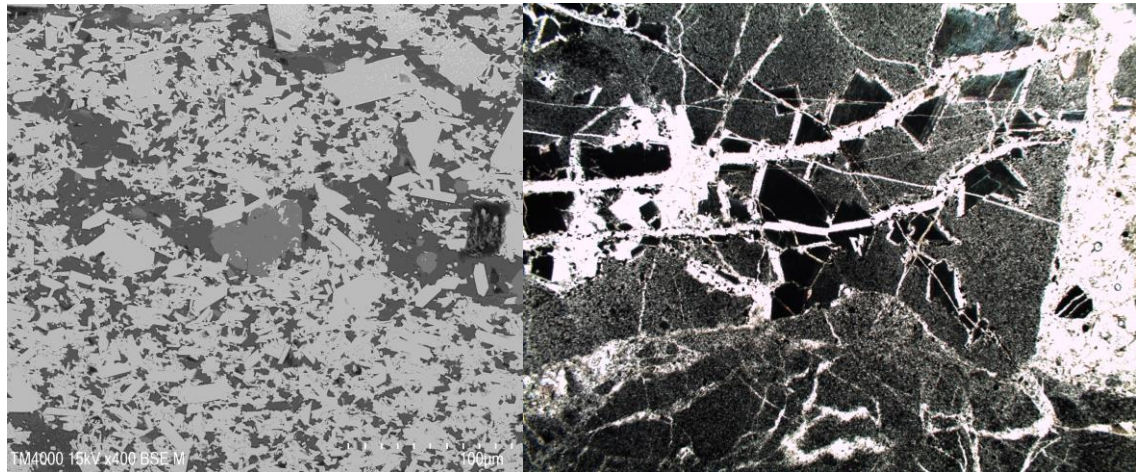


Fig. 25. A. Ironstone in SEM showing microplaty hematite and recrystallized hematite. B. Ironstone in reflected light showing recrystallization of hematite/siderite along carbonate veins

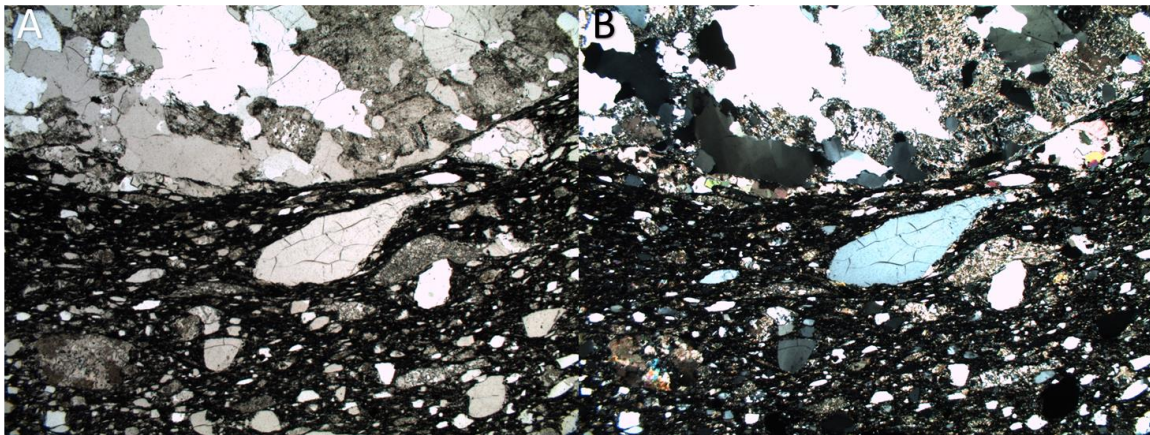


Fig. 26. Iron oxide breccia sample G29 showing preferred orientation of elongated clasts/grains.

3.6 Hematite petrography

Hematite in the ferruginous diamictites and siltstones sampled from the Disrupted beds displays a differing morphology than hematite from the breccia with pebbles and cobbles layer of M1 and D19 and D20 of M2. Figures 27-29. show the differing morphologies of hematite throughout the Fe rich beds. Figures 27A;B show a sample from the ferruginous diamictites of the Disrupted Beds, where large, pore filling hematite can be seen in the center and upper right of the image and hematite cement can be seen surrounding clastic grains. Figures 28 A and B show hematite from D19 displaying a rounded to sub-rounded morphology, and lack of hematite cement between clastic grains. In the Disrupted Beds ilmenite was often observed as exsolution lamellae in large hematite grains and as “armored” grains surrounded by hematite (Fig. 29C;D.)

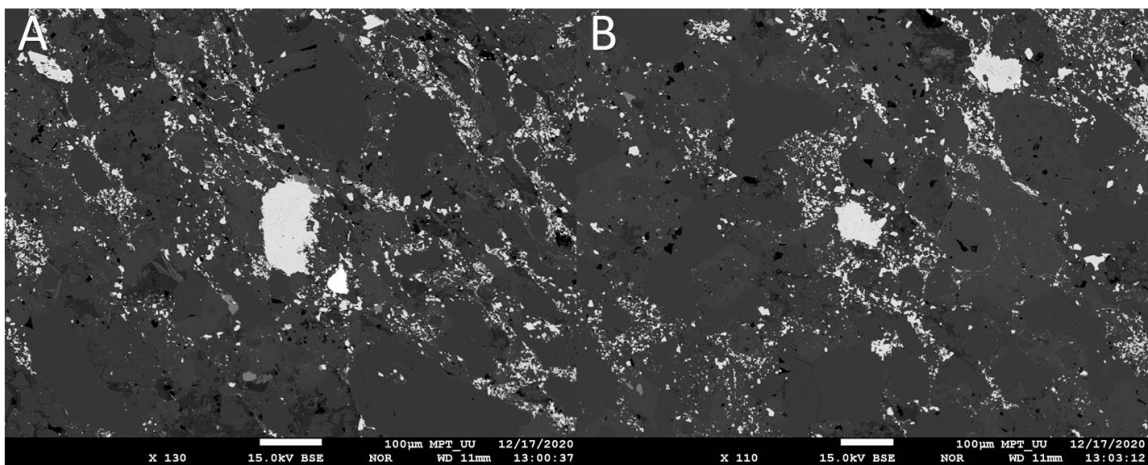


Fig 27. SEM images of hematite (white) in ferruginous diamictite from the Disrupted Beds of the Carvellachs displaying pore filling morphology and hematite cement between grains.

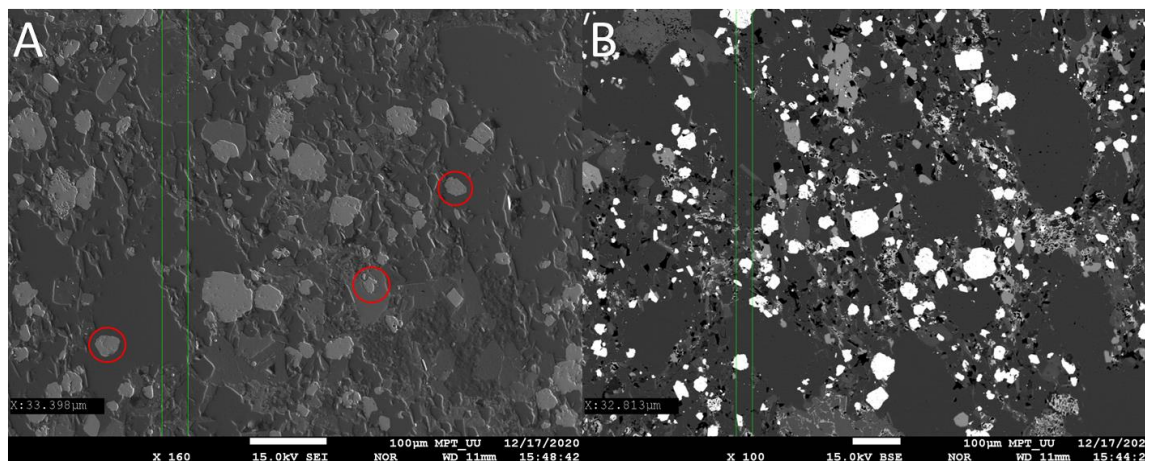


Fig.28. SEM image of D19 (A) and D20(B) from Member 2 showing rounded hematite grains. Red circles in (A) show hematite enclosed by quartz and carbonate cement.

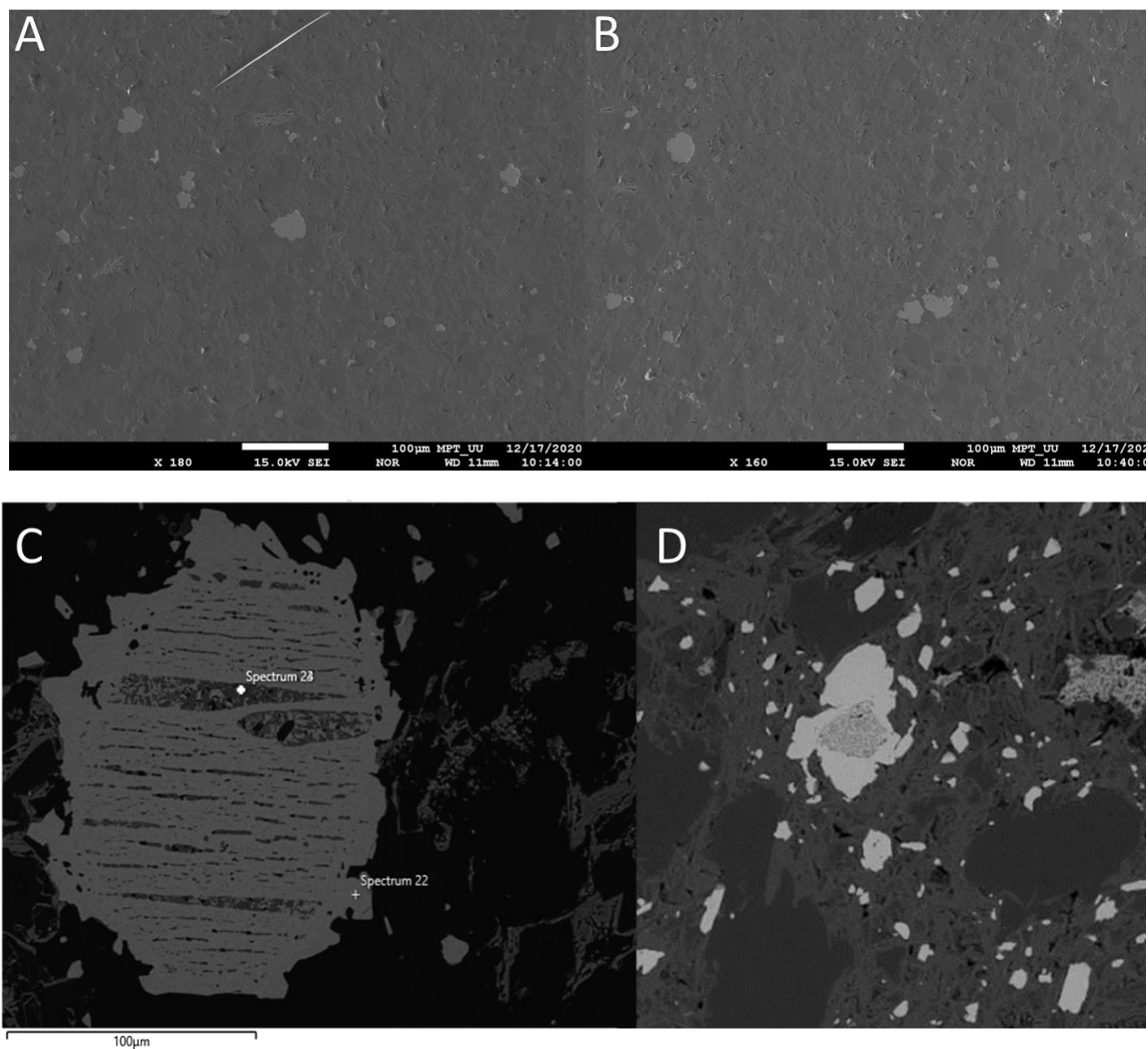


Fig. 29. A and B: SEM image of hematite (light grey) in sample from breccia with pebbles and cobbles below Disrupted Beds. C. SEM image of hematite (light grey) with lamellae of ilmenite. D. “Armored” ilmenite grain surrounded by hematite (light grey)

3.7 Geochemistry of the Islay and Garvellachs Fe formations

3.7.1 Major oxides

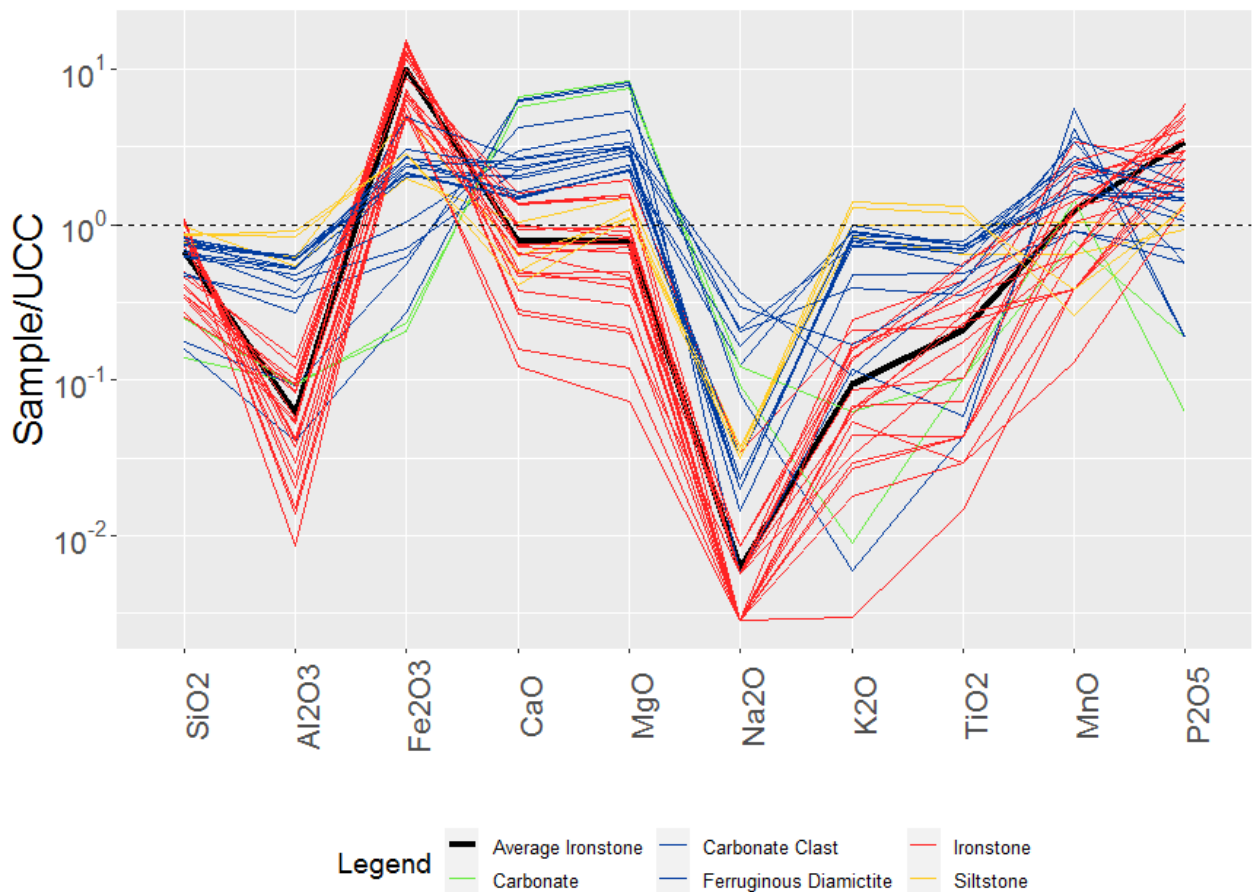


Fig. 30. Spidergram showing the major oxide components normalized to UCC. Dashed line represents UCC average.

Major oxide values were normalized to the upper continental crust composite (UCC) of Kamber (2005) and show the majority of the samples are enriched in Fe₂O₃ with the exception of the carbonate and some diamictite samples. The ferruginous diamictites range in Fe₂O₃ from 5-34 wt.% on the Garvellachs, to 15 wt.% in the Islay samples. The ironstone varies in Fe₂O₃ from 25-73 wt.% and Al₂O₃ is in low concentrations in the ironstones (mean 0.92 wt.%) and near average shale values in the ferruginous diamictite of the Garvellachs. The ironstone is lower in concentration in TiO₂ and K₂O relative to UCC, while the diamictite shows average UCC values. All samples show very low concentrations of Na₂O relative to UCC. CaO and MgO are elevated in the diamictite samples due to the high proportion of dolomitic clasts and carbonate component in the matrix.

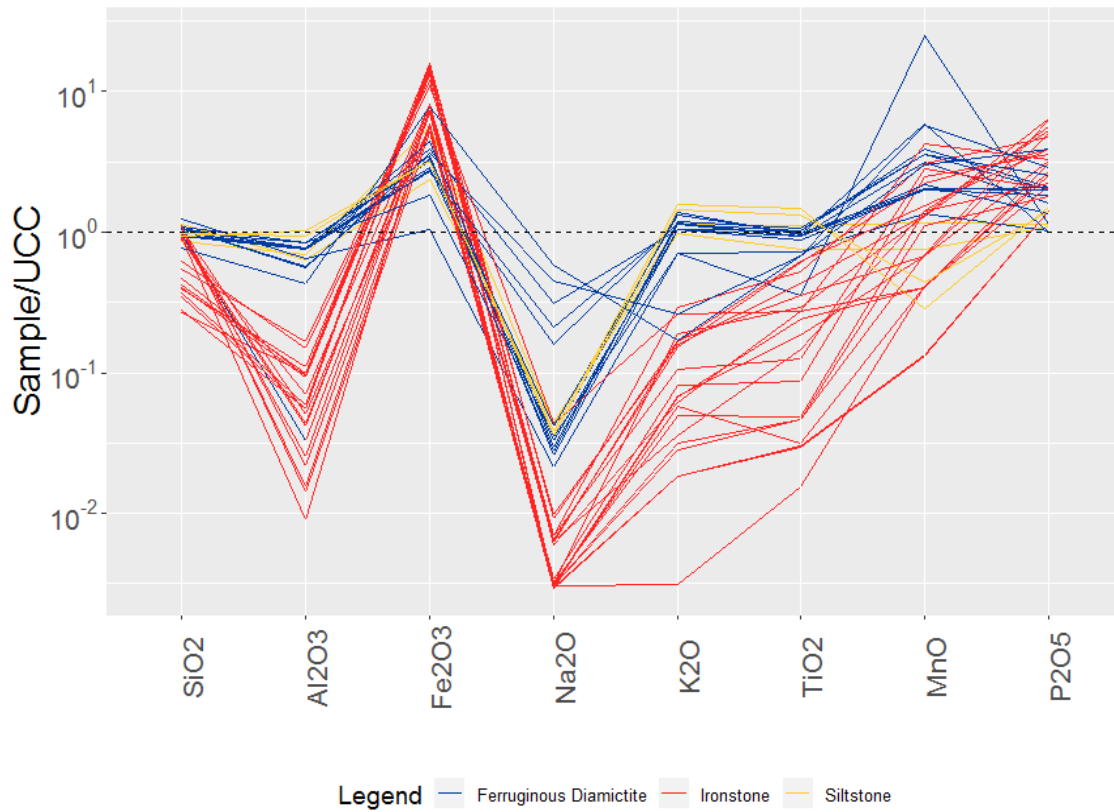


Fig. 31. Major oxides normalized on a carbonate free basis. Dashed line represents UCC average.

To account for the high proportion of carbonate clasts in the diamicrite and veins in the ironstone, the sample compositions were normalized to remove the carbonate. CaO , MgO and LOI were removed, and the data was normalized to UCC. The spidergram in Fig. 31. shows these values after recalculation, which shows that with the exception of Na_2O and Fe , the siltstone and ferruginous diamicrite better follow the UCC average(dashed line) . There is an increase in the proportion of Fe in the diamicrite and siltstones in the carbonate normalized pattern indicating that the matrix of the clastic rocks is strongly enriched in Fe and despite the care taken to avoid clasts in the analyzed samples, carbonate clasts and matrix still play a role in dilution of the geochemical composition of the diamicrites.

3.7.2 Major oxide correlations.

	SiO ₂	Al ₂ O ₃	Fe ₂ O ₃	CaO	MgO	Na ₂ O	K ₂ O	MnO	TiO ₂	P ₂ O ₅
SiO ₂	1	.248	-.6045	-.2802	-.2079	-.0168	.248	-.3695	.0428	-.3916
Al ₂ O ₃		1	-.6382	.2019	-.3594	.3019	.9765	.1029	.9272	-.5387
Fe ₂ O ₃			1	-.5365	-.6305	-.3097	-.578	-.3232	-.371	.6883
CaO				1	.9842	.3342	.122	.8217	.0597	-.3916
MgO					1	.3575	.282	.7933	.2037	-.5067
Na ₂ O						1	.1378	.3759	.2419	-.1905
K ₂ O							1	.0505	.9256	-.5081
MnO								1	.049	-.2158
Ti ₂ O ₃									1	-.3397
P ₂ O ₅										1

Table 2. Pearson correlation coefficients for major oxides from the Disrupted Beds clastic rocks. Strong positive correlations >.6 are marked in blue and negative correlations <.6 are marked in red. (Full dataset can be found in appendices)

Correlations between the major oxides are presented in Table 2. Fe₂O₃ shows little positive correlation with any oxide with the exception of P₂O₅, which points to the possibility of preferential absorption of phosphate onto ferrihydrites. A strong negative correlation between Fe₂O₃ and SiO₂ and Al₂O₃ is observed.

Calcium and Mg show strong positive correlations indicating the dominant carbonate in the system is dolomite. Mn shows a negative correlation with Fe, however there is a fairly strong positive correlation between Mg, Ca and Mn.

	SiO ₂	Al ₂ O ₃	Fe ₂ O ₃	CaO	MgO	Na ₂ O	K ₂ O	MnO	TiO ₂	P ₂ O ₅
SiO ₂	1	-.5558	-.8793	-.1276	-.0918	-.2696	-.6859	-.2242	-.8026	-.4036
Al ₂ O ₃		1	.1236	.8085	.8155	.523	.9897	.6539	.7898	.0924
Fe ₂ O ₃			1	-.5365	-.3105	-.2536	-.4460	-.203	-.5878	.3828
CaO				1	.9843	.5413	.5975	.9556	.2708	.233
MgO					1	.5667	.5766	.9738	.2198	.0697
Na ₂ O						1	.5329	.6292	.211	.0389
K ₂ O							1	.6729	.7642	.420
MnO								1	.4603	.0946
Ti ₂ O ₃									1	-.3397
P ₂ O ₅										1

Table 3. Pearson correlation coefficients for major oxides of the ironstones. Strong positive correlations >.6 are marked in blue and negative correlations <.6 are marked in red. (Full dataset can be found in appendices)

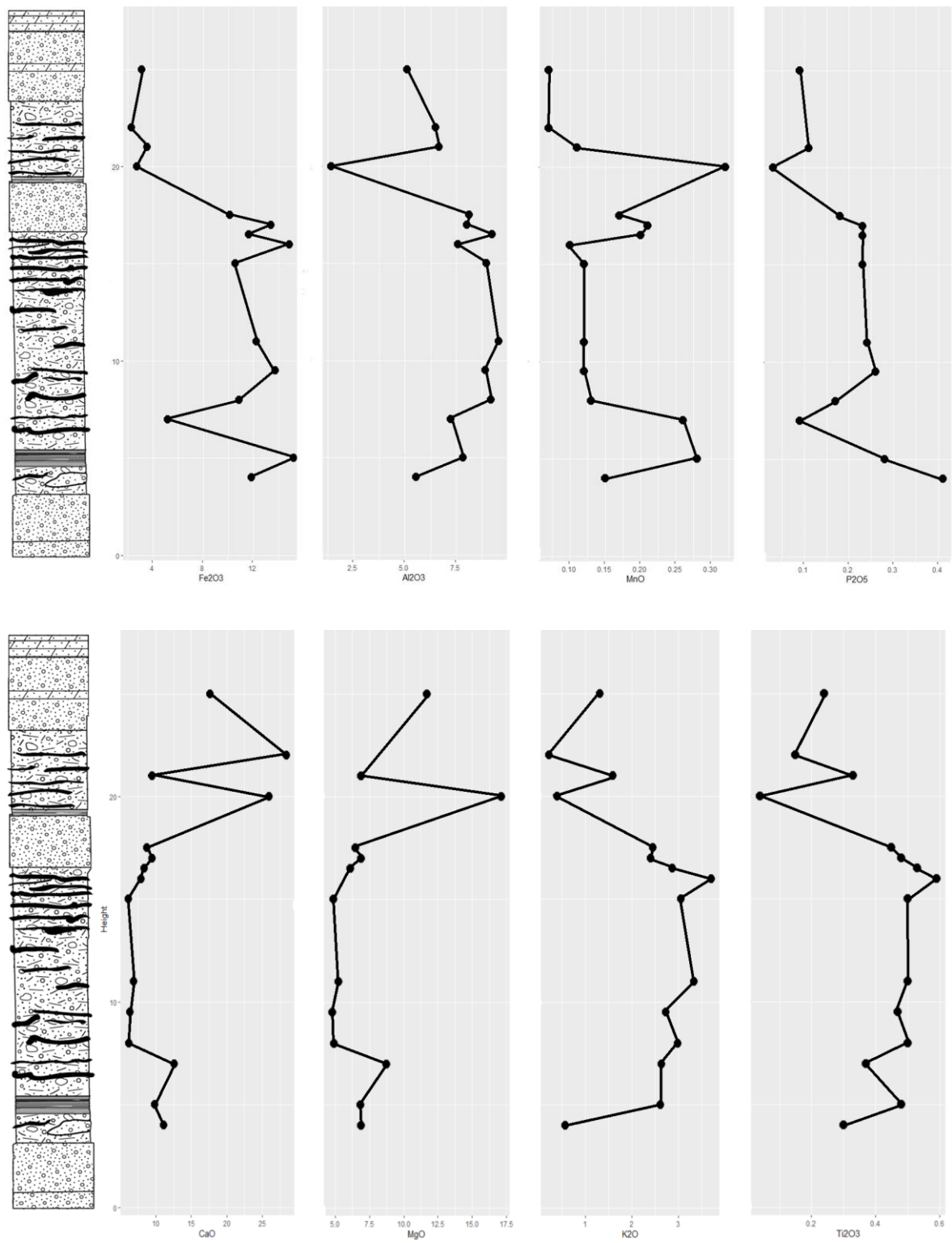


Fig. 32. Major oxides by wt% plotted against the stratigraphic log of Bealach an Tarabrit. Column redrawn from Spencer (1971).

The major oxides of the Disrupted Beds samples at Bealach an Tarabairt are plotted against the stratigraphic column in Fig. 32. Iron, P and Mn show a decreasing trend upwards through the stratigraphy, where they are enriched in the first two diamictite beds, and decrease in concentration in the uppermost diamictite bed. CaO increases in moving up section, while Al, K and Ti decrease, a reflection of the increasing proportion of carbonate in the matrix of the diamictites and a decrease in the clastic proportion.

3.8 REY geochemistry

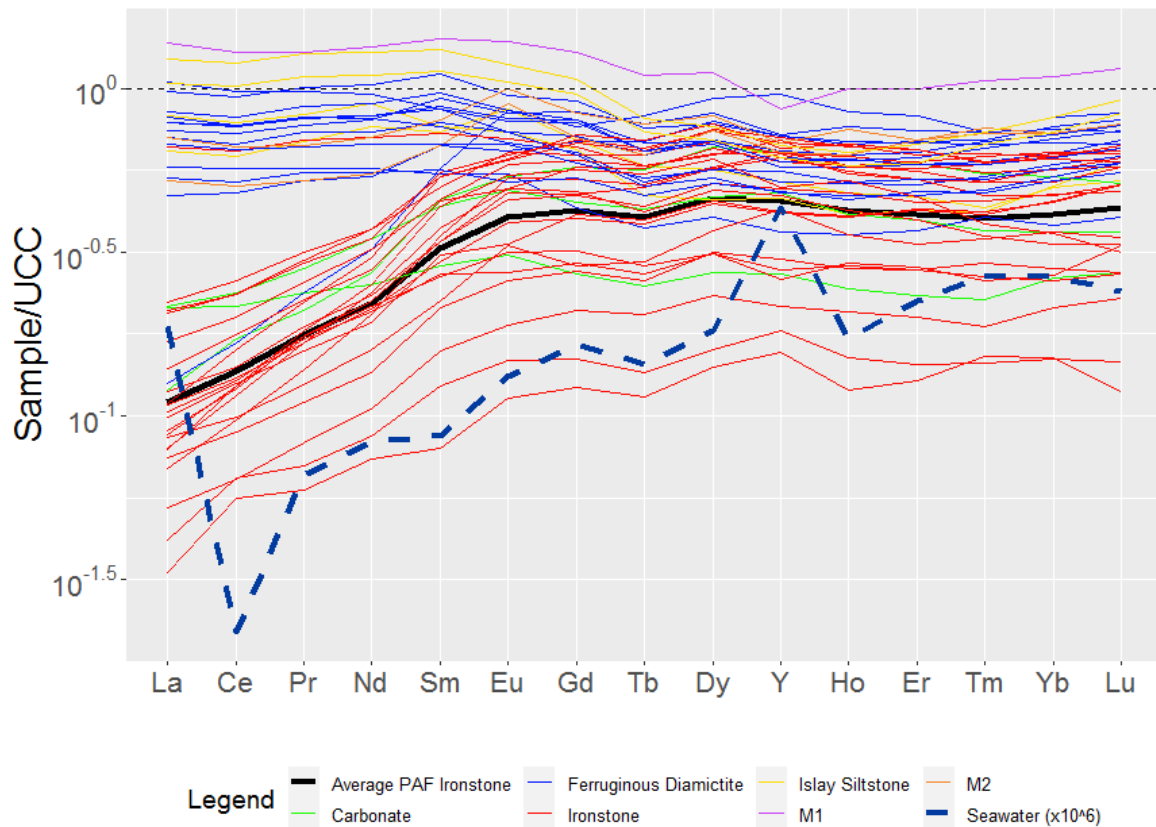


Fig. 33. REE + Y from whole rock analysis. Dashed line represents UCC average.

The spidergram in Fig. 33 shows the REE+Y of the samples from the Garvellachs and Islay normalized to the UCC composite from Kamber (2005). Samples from the Islay siltstone and the Garvellachs ferruginous diamictites show REE patterns close to that of UCC.

The iron formation (red) from the Garvellachs shows the typical depletion in LREE values of BIFs (Baldwin, 2012; Ilyin 2009). The ferruginous diamictite show enriched levels of LREE compared to HREE typical of detrital provenance. The REY patterns of the carbonate samples shows a similar pattern to that of the ironstones. The diamictite outlier is sample G14, which contained a high proportion of carbonate clasts. A single outlier of the ironstone is observed with a REE pattern close to UCC. This sample, G29 is a breccia with carbonate clasts and an ironstone matrix above the uppermost ironstone which contained 8 wt.% Al_2O_3 .

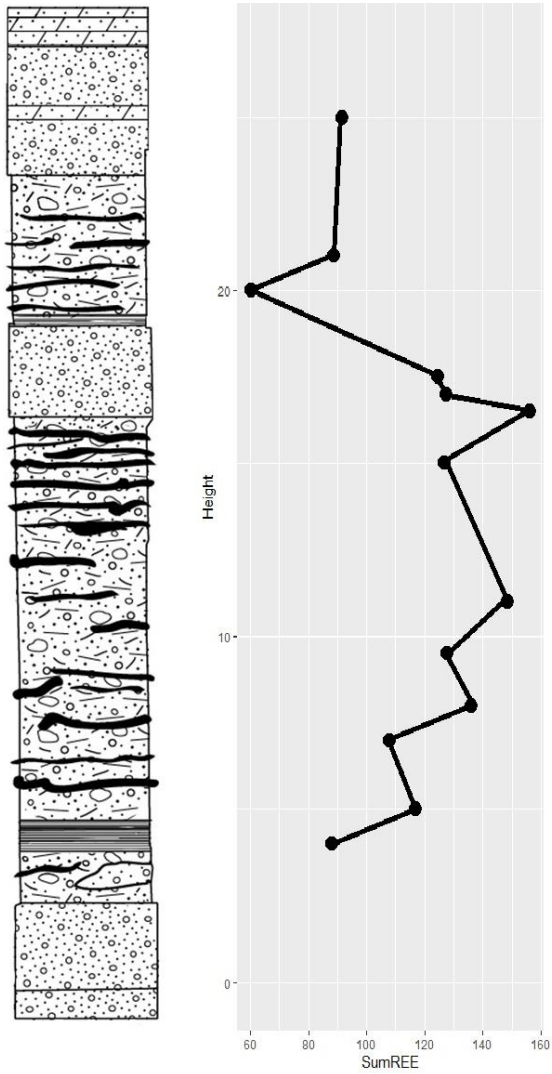


Fig.34. Σ REE plotted against stratigraphic height at Bealach an Tarabairt

Figure 34. Shows the sum of REE in the samples from Bealach an Tarabairt plotted against the stratigraphy. A trend of increasing Σ REE is seen in the clastic samples before decreasing as the percentage of carbonate minerals increases.

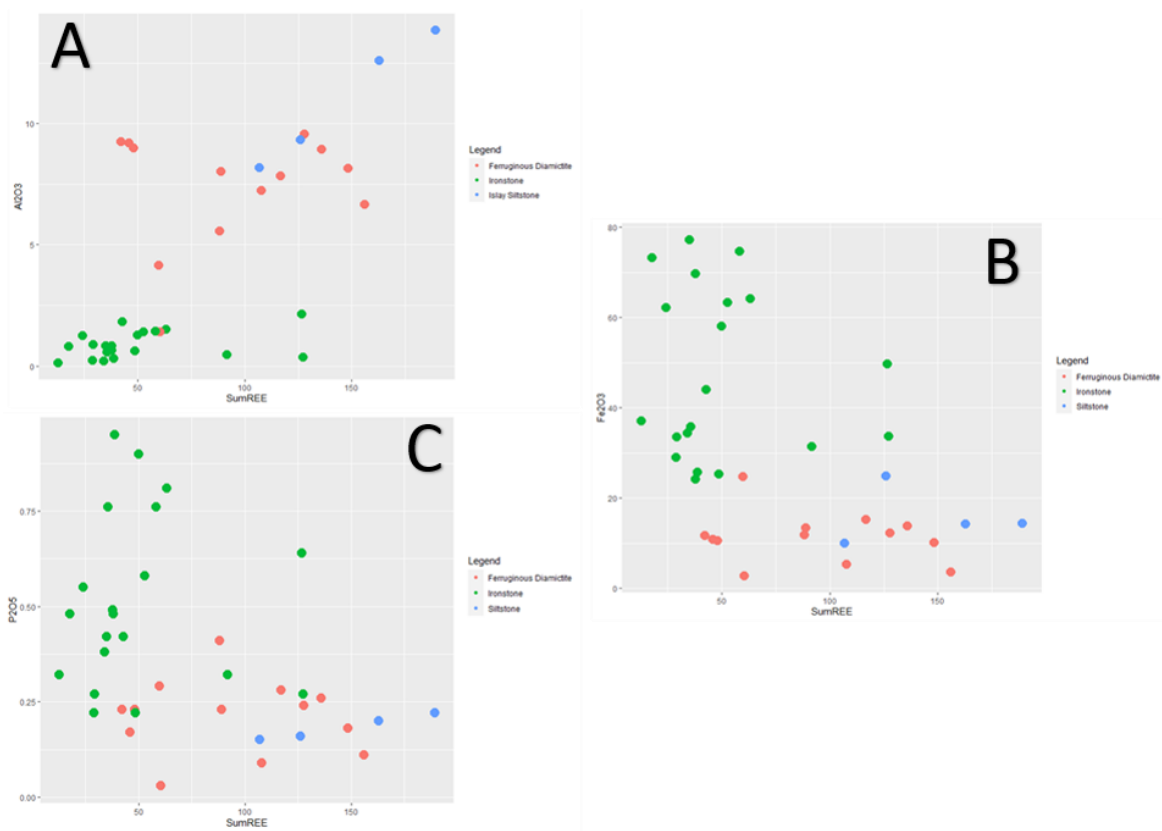


Fig. 35. Covariance plots examining the relationship of major oxide (A. Al₂O₃ B. Fe₂O₃ c. P₂O₅) control over Σ REE. Al₂O₃ shows the strongest control over REE concentration in the diamictites, with Fe and P exhibiting some correlation in the ironstones and a potential trend expressed between P₂O₅ and REE in the Islay siltstones.

3.8.1 REE correlation coefficients

	SiO ₂	Al ₂ O ₃	Fe ₂ O ₃	CaO	MgO	Na ₂ O	K ₂ O	MnO	TiO ₂	P ₂ O ₅
ΣLREE	.1951	.983	-.6135	.2301	.3841	.3665	.948	.1555	.9217	-.4931
ΣHREE	-.5123	.3934	-.1216	.5475	.5629	.2474	.3851	.5938	.4883	.0711
ΣREE	.2214	.7034	-.4925	.1603	.2721	.0362	.6875	.0231	.654	-.3957

Table 4. Pearson correlation coefficients for major oxides vs REE for all clastic samples. Strong positive correlations >.6 are marked in blue and negative correlations <.6 are marked in red.

Table 4 presents the REY data for all clastic samples from the Disrupted Beds. The strongest correlations are shown between the detrital proxies of Al, K and Ti pointing to a strong control over the REE budget, in particular over the LREEs. The carbonate proxies of Ca, Mg and Mn show a moderate correlation between their HREE values.

	SiO ₂	Al ₂ O ₃	Fe ₂ O ₃	CaO	MgO	Na ₂ O	K ₂ O	MnO	TiO ₂	P ₂ O ₅
ΣLREE	-.6542	.8041	.5651	.2454	.1724	.179	.8096	.2986	.7815	.6463
ΣHREE	-.6659	.8182	.4925	.5406	.4504	.3303	.8137	.548	.7564	.7103
ΣREE	-.6785	.8339	.5539	.3679	.2859	.2434	.8356	.4048	.7953	.6907

Table 4. Pearson correlation coefficients for REE+Y in the ironstones. Strong positive correlations >.6 are marked in blue and negative correlations <.6 are marked in red.

Table 4 shows the correlation coefficients for REY samples of the ironstones. A strong negative correlation with Si is observed. Moderate positive correlations are seen with regards to Fe and REY values, and strong correlation with P and REY. ΣREE average of the ironstones is volumetrically minor compared to the diamictites and siltstones of the Disrupted Beds (mean 37ppm and 123ppm respectively).

3.9 Phosphate petrology results

3.9.1 Xenotime

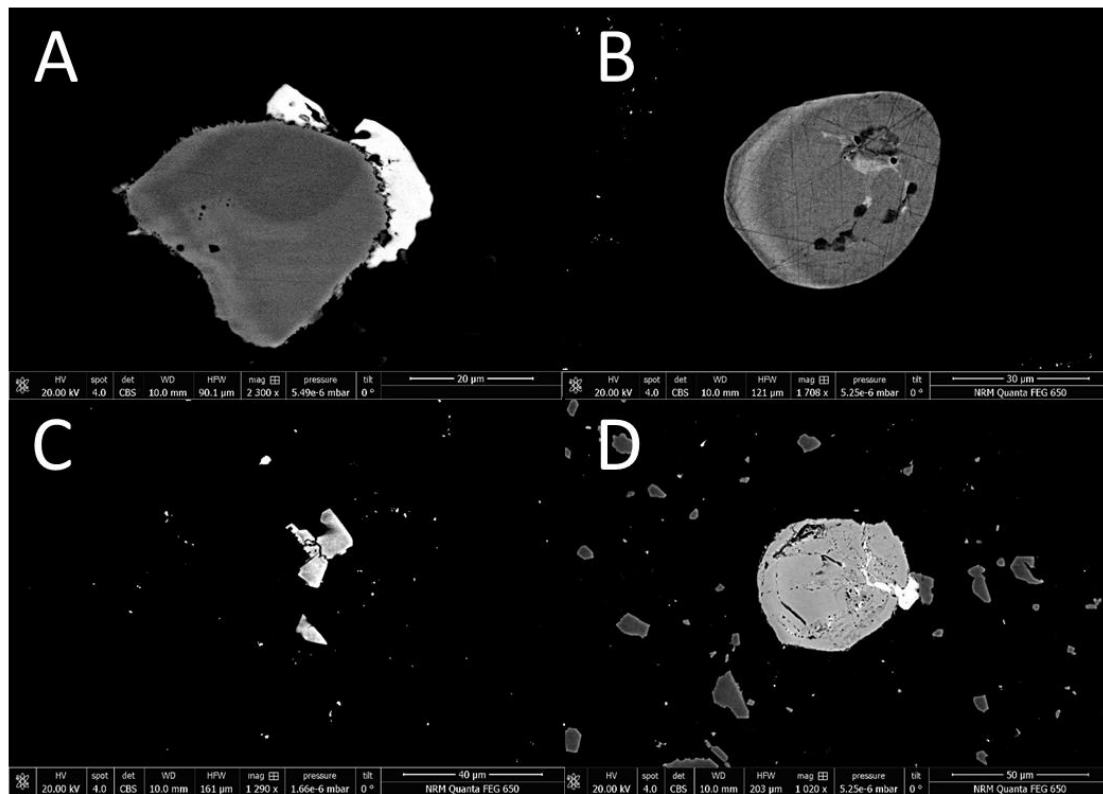


Fig. 36. Xenotime captured in backscattered electron imaging. A. Xenotime (white) overgrowth on detrital zircon. B. Rounded detrital(?) xenotime. C. Pyramidal xenotime overgrowths on zircon. D. Zircon (light grey) with xenotime infill in fracture (white) with numerous hematite crystals (dark grey)

Xenotime was observed in almost all clastic samples from Islay and the Garvellachs, while not present in the ironstones. Xenotime was predominantly found as $<20\mu\text{m}$ overgrowths on detrital zircon, with occasional xenotime infill of fractures in zircon (see Fig. 36D.). Occasional growth of xenotime separate from zircon were observed often occupying pore space between the grains, or as growths associated with hematite. One large ($<40\mu\text{m}$) xenotime was observed (Fig. 36B.) showing a rounded morphology and apparent overgrowths on a core.

Y_2O_3 is the dominant component of the xenotime, comprising between 42-47 wt.% of the analyzed samples. P_2O_5 is the dominant non-REE fraction of the xenotime with values between 33-56 wt.%. Table 5. shows the REE element distribution in the studied xenotime. Dy_2O_3 (4.5-5.3 wt.%) is the second most abundant REE oxide, followed by Er_2O_3 , Yb_2O_3 , and Gd_2O_3 . The elements La, Ce, and Pr were below detection limit and are likely fractionated into other REE phosphate phases such as monazite. Uranium had an abundance between .03-.2 %wt.

Sample	Nd	Sm	Eu	Gd	Tb	Dy	Ho	Er	Tm	Yb	Lu
Xtm 1	3142	4892	2830	23633	5542	47625	11250	36550	5173	34533	4910
Xtm 2	1150	2800	1675	17250	4613	46013	11000	36688	4775	28750	4100
Xtm 3	843	3200	3171	18014	5314	49043	10943	35843	4343	26914	2600
Xtm 4	2075	3075	1475	15150	4275	45575	11975	36250	4825	30325	3050
Xtm 5	1240	3300	1820	17260	4400	46760	11360	36480	4500	31180	3580
Xtm 6	800	3000	2100	17833	4033	46867	11233	37867	5033	29200	2267
Xtm 7	1575	3213	1963	18575	4613	48663	11925	35650	4975	28013	2600
Xtm 8	1650	3350	2225	19075	5025	48400	11425	34850	2950	28050	3600
Xtm 9	1800	3133	2067	16967	4233	48700	10400	34733	5100	25600	2450
Xtm 10	929	3171	2257	17971	4700	49629	11800	38886	5114	28929	3086
Xtm 11	800	3350	3300	18200	4850	49300	10100	34650	3000	23450	2800
Xtm 12	1900	2800	2000	17000	6200	47400	12600	37700	4700	28900	4200
Xtm 13	2200	3300	2700	18800	3500	53700	14300	39600	4900	28200	6200
Xtm 14	900	2700	1100	15800	4800	46200	9400	35400	4000	26400	3800
Xtm 15	800	3300	900	17100	4700	46600	10000	36700	5700	32600	3900

Table 5. EDS trace element data (REE + U) of xenotime in the PAF in ppm.

3.9.2 Monazite

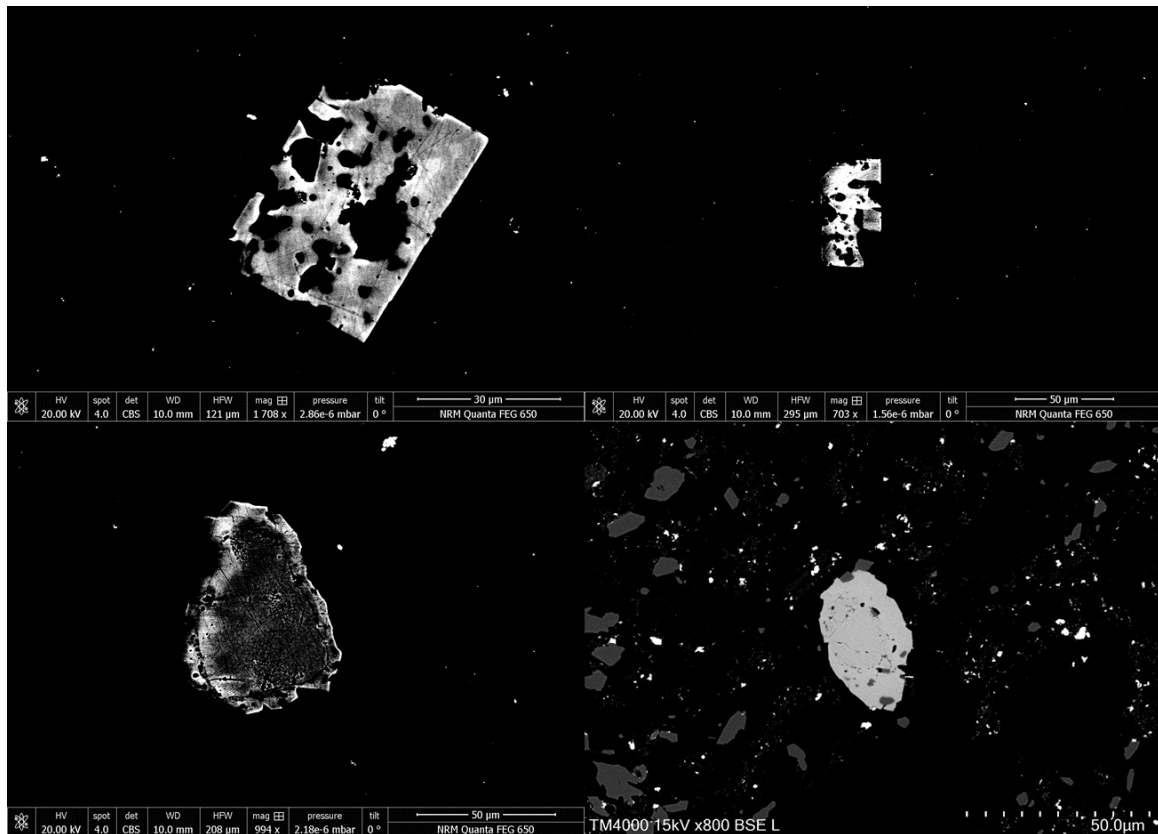


Fig. 37. Monazite crystals imaged in BSE showing various observed morphologies. A, B. Orthogonal monazite showing “Swiss cheese” pattern indicative of metamorphic growth. C. Ultra high contrast image of Monazite was observed in every sample analyzed, often small with a rounded morphology that may be indicative of a detrital source. Larger monazite crystals were observed, often in a distinctly euhedral rectangular pattern with a “Swiss cheese” appearance (see Fig. 37A. and B.) that is common amongst metamorphic monazite (Majka et al. 2008) indicating the monazite is not useful for determining the age of deposition.

4. Discussion

4.1 Background

The Disrupted Beds present a challenge in the interpretation of paleoenvironment during their deposition. The heterogeneity displayed in their 35 m of exposure alternating between ironstone, diamictite, ferruginous diamictite and siltstone, carbonates and carbonate conglomerate/diamictite, and sandstone are evidence of shifting changes in their depositional environment and clastic provenance (e.g. Spencer, 1971; Benn and Prave, 2006; Ali, 2019). The general consensus since the work of Benn and Prave (2006) has interpreted the Disrupted Beds as an ice marginal to sub-ice depositional environment. Due to the SARS-CoV-2 pandemic, the two planned field study trips were not conducted due to travel restrictions. Therefore, this study relies upon observations from earlier published studies, as well as field observations collected since 2012 by other field workers, and samples collected by Iain Pitcairn that were analyzed by the author. Due to the more complete exposure of the Disrupted Beds on the Garvellachs, the discussion will predominantly focus on those sampled localities.

4.2 Sedimentology

The general trend of clastic input in the Disrupted Beds on the Garvellachs indicates changes in the depositional environment both in the energy regime and clastic makeup of the beds. The base of the Disrupted Beds at both study localities is a conglomerate, at Bealach an Tarabairt the conglomerate is overlain by a stratified diamictite and a laminated siltstone layer (Fig. 18A; C.). At Eileach an Naoimh the conglomerate is thicker, and is overlain by a sandstone followed by a finely laminated siltstone layer that appears to correlate across both localities. This points to a possible period of decreasing energy in the basin before the deposition of the ironstones, and a possible increase in sea level. Floating ice is interpreted as being present at this time interval as evidenced by the limestones in the siltstone sampled from Bealach an Tarabairt and observed in the laminated siltstone (Fig. 23A.) below the ironstones on Eileach an Naoimh interpreted as ice-rafted debris.

The high iron content of the diamictites, and the apparent genetic relationship between NIFs and glaciogenic deposits in other localities leads to the question - do the Disrupted Beds represent a NIF? To answer this question the major and trace elements contents of the rocks are investigated and compared to those from other NIFs.

4.2 Major Oxides.

4.2.1 Clastic Samples.

Clastic samples in the Disrupted Beds generally show variation in their major oxide components in the non-carbonate normalized plot. Iron shows steep enrichment in most of these samples, as do Ca, Mg as well as Mn. The high proportion of dolomitized carbonate minerals in the matrix are likely responsible for these enrichments, and thus the values were normalized on a carbonate free basis to present a clearer image of the relative abundances of the major elements (Fig. 31.). After this normalization a trend closer to the UCC average is observed, demonstrating the influence that the carbonate minerals have on the major oxide geochemistry. Iron and P are enriched relative to UCC in the clastic samples, potentially indicating the precipitation of Fe from the water column in these beds.

Na is the only element that is shown to be strongly anomalous in the clastic samples relative to UCC which has been previously interpreted to be caused by later removal of Na during

metasomatism (Dahlgren, 2020). Manganese shows a stronger enrichment in the carbonate free plot, which points a relationship between Mn and the carbonate minerals. The carbonate bodies and large carbonate clasts in the Disrupted Beds as well as other diamictite beds in the PAF have been interpreted as concretions (Ian Fairchild, personal communication) which the strong connection of Mn to the carbonate minerals supports (see section 4.5.1 for further discussion).

Very strong correlation is seen in Table 2 between the elements Al, Ti, and K. Aluminum is commonly used in other studies of BIFs as a proxy for the detrital component in the system (e.g. Klein and Beukes, 1993; Baldwin et al., 2012; Lechte et al., 2018) as Al is an immobile element in aqueous systems. The strong correlation of Al with Ti and K indicates that these two elements, of which Ti is typically immobile while K is mobile in seawater, are both appropriate proxies for detrital input in the PAF along with Al.

The general trends in the major oxide components of the PAF in the clastic and carbonate samples are shown in Fig. 32. plotted against the stratigraphic column of Bealach an Tarabairt. General trends observed are decrease in the concentrations of the detrital proxies Al, Ti and K moving upwards through through the stratigraphy, along with an increase in Ca, and Mg, pointing to an increasing carbonate component in the diamictites. In Fig. 18D. the uppermost sample of diamictite (G17) is shown, displaying a cream colored matrix that is dominantly carbonate. This change in the composition of the matrix points to a shift in the either the provenance of the clastic input, or a shift to carbonate precipitation with the clastic component representing ice-rafted debris, however, the lack of clear bedding hinders observations to determine if the stones are ice-rafted. Iron concentration in the clastic samples of the Disrupted Beds decreases higher in the stratigraphy, until reaching below shale values, pointing to possible exhaustion of Fe supply in the basin. The large euhedral pyrite observed, as well as other smaller pyrite crystals in the carbonate diamictite coincides with the trend of decreasing Fe concentration.

4.3.2 Ironstone samples

Major oxide analysis of the ironstone samples showed very strong enrichment in Fe, up to one order of magnitude above UCC. Phosphorus is enriched in the ironstone, a typical feature of BIFs and NIFs (Ilyin, 2009). The low concentration of the detrital proxies of Al, Ti, and K indicate that there is only a small amount of detrital input in the ironstones ($\sum \text{Al}_2\text{O}_3 + \text{K}_2\text{O} + \text{TiO}_2 = 0.15\text{-}3.25\%$). Calcium is shown be enriched slightly above UCC, possibly due to the presence of carbonate veins in many of the samples, as well as abundant apatite in the ironstones.

Major oxide correlations shown in Table. 3. demonstrate a strong negative correlation of Fe and silica, and expected result as Fe and Si are the dominant components of the ironstones. The detrital proxy of Al showed very strong correlation with the other established detrital proxies of Ti and K, however Al also showed very strong correlation with the carbonate proxies of Ca and Mg, as well as Mn. This indicates that the dominant carbonate delivery to the ironstones may have been detrital in origin. The lack of Mn correlation with Fe may point to a diagenetic or carbonate hosted source for Mn rather than a hydrothermal source for Mn. Phosphorus showed little correlation with any major oxide with the exception of a moderate correlation with Fe.

4.2 REE Discussion

4.2.1 Indicators of seawater origin of REE patterns in the Ironstones.

The use of REE+Y systematics in the study of NIFs has been well established as a proxy for the redox conditions of seawater and the depositional conditions of NIFs (Klein and Beukes, 1993; Klein, 2005; Baldwin et al., 2012; Cox et al., 2015; Gaucher et al., 2015). LREEs (La-Sm) show depletion while the heavier elements show enrichment in both iron formations and seawater. A test used to determine enrichment is by using the UCC normalized (denoted by subscript n) Pr_n/Yb_n ratio, as these are

respectively the lightest and heaviest REEs whose behavior in seawater is based on their atomic radius (Lawrence and Kamber, 2006). A low Pr_n/Yb_n ratio indicates enrichment in HREE over LREE and thus indicates a seawater signal. The samples from the ironstones show Pr_n/Yb_n values between ~ 0.34 at the base, rising to 0.65 in the uppermost ironstone bed indicating strong to moderate enrichment of HREE over LREE. Samples from the clastic beds of the Disrupted Beds are not included in these analyses due to clastic contamination producing near UCC trends for REE+Y patterns.

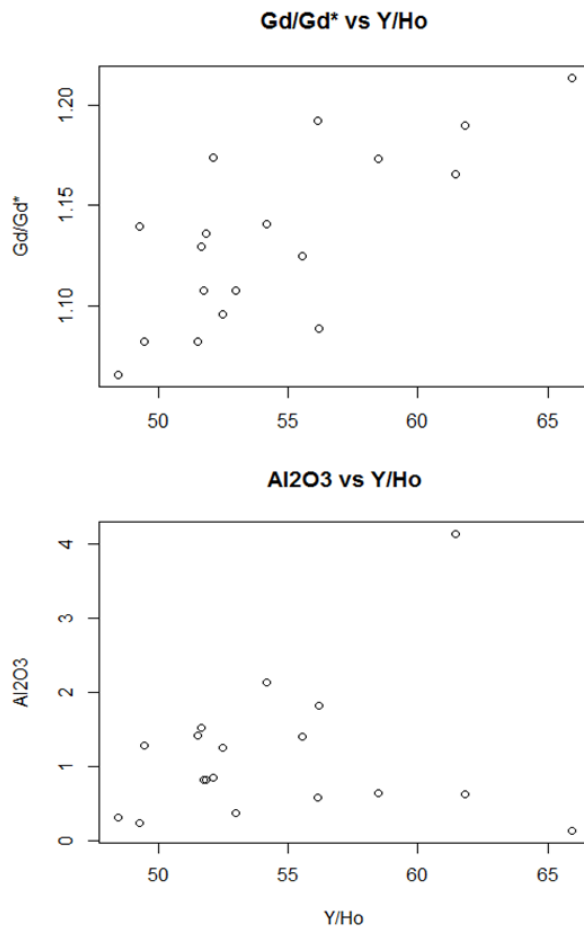


Fig. 38. Top; Gd/Gd* vs Y/Ho in the ironstones. Bottom: test on seawater control over the Y/Ho ratio versus detrital control using Al as a proxy.

The systematics of the molar Y/Ho ratio and the gadolinium anomaly (Gd/Gd*) have been used as indicators of seawater origin of Fe formations (Bau, 1993; Kato et al., 2006; Planavsky et al., 2010; Baldwin et al., 2012). In seawater Y behaves conservatively while Ho is rapidly fractionated from the water column, within meters distance from hydrothermal sources, leading to enrichment in Y over Ho in seawater (Bau and Dulski, 1996; 1999). Igneous rocks and rocks derived from continental crust typically demonstrate near chondritic values (~ 26) as Y and Ho demonstrate

similar behavior during crystallization and thus do not strongly fractionate (Bau and Dulski, 1996; Planavsky et al., 2010). Rock precipitated from seawater, such as BIFs and carbonates will thus show super chondritic Y/Ho ratios over >26 , with BIFs showing typically ratios of >44 .

Gadolinium also behaves anomalously in seawater when compared to shale, UCC and chondrite normalized patterns, producing positive anomalies that are also reflected in BIFs and are thus

interpreted as a sign of a seawater origin for BIFs (de Baar et al., 1985; Bau et al., 1995; Baldwin et al., 2012).

Previous works (e.g. Bau and Dulski, 1996; Planavsky et al., 2010; Baldwin et al., 2012) have used this system to determine the marine signature of BIFs, and this method has been applied to the ironstones of the PAF. The PAF ironstone shows superchondritic Y/Ho values ranging from 45.1 - 61.8 and positive Gd/Gd* anomalies (1.08-1.21). Figure 38A. shows the Gd/Gd* plotted against the Y/Ho ratios. While the processes leading to the fractionation of Y/Ho and the enrichment of Gd in seawater are unrelated, the fairly strong positive correlation of the Gd anomaly and the Y/Ho ratio ($r^2=.54$) shows evidence for seawater origin for the REE patterns in the ironstones in that there is a correlation between the magnitudes of two independent REE fractionation processes occurring in seawater reflected in the PAF ironstones. Figure 38B. shows the Y/Ho ratio compared to Al_2O_3 , where Al is used as a proxy for detrital input.

There is no evidence of correlation between Y/Ho and Al_2O_3 ($r^2=.03$), which further provides support for the Fe formations preserving a seawater chemical signal with detrital input having no control on the Y/Ho ratio. Ironstones are typically poor in REE and therefore a small detrital component can mask any marine REE signal in ironstone with clastic contamination >1-2% (Bau, 1993) and thus additional tests are important to determine what effect detrital

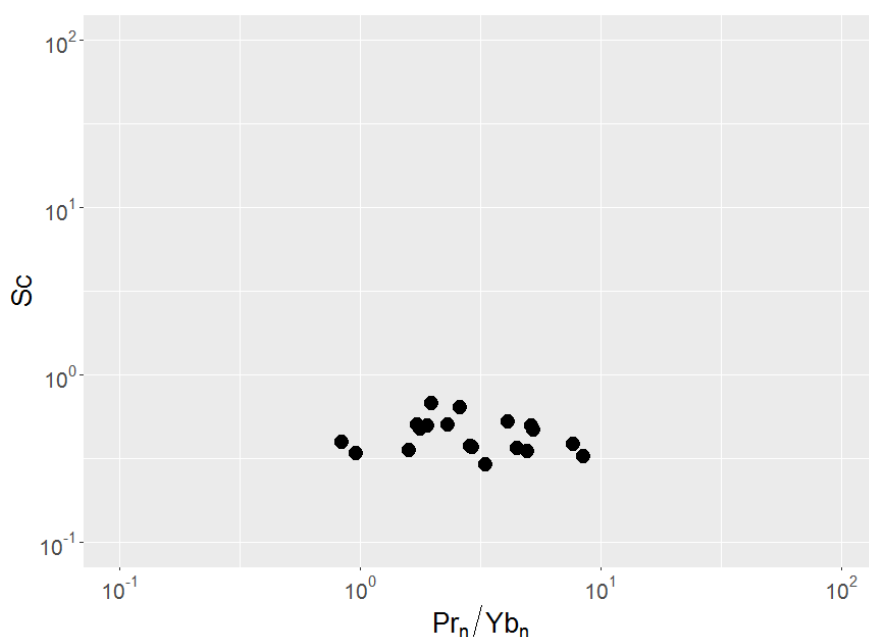


Fig. 39. Scandium and Pr_n/Yb_n showing no correlation, indicating lack of detrital control on REE fractionation in the ironstones.

contaminants may have on the REE fractionation.

The covariation of Sc with REE has been used as an additional test on detrital influence after Bau (1993) by determining correlation between Sc and the Pr_n/Yb_n ratio. Scandium is a trace element that is immobile in aqueous solution, and thus higher levels are not likely to have originated from seawater (Bau, 1993). A positive correlation between Sc and Pr_n/Yb_n is an indication that the ratio of the enrichment of the REEs has a detrital influence. There is no correlation of Sc and the REE ratio observed in the ironstones (Fig. 39.), further evidence of a lack of detrital controls on the REE fractionation.

As demonstrated in Fig. 35, the REE pattern of the ironstones is more closely tied to Fe_2O_3 and P_2O_5 , indicating that Fe-oxhydroxides and phosphates adsorbed REE from the water column

There is continued debate over the depositional environment of the Disrupted Beds (Benn and Prave, 2006; Ali et al., 2018) with arguments for both a lacustrine and marine environment. The marine signals in the ironstone of LREE depletion and relative HREE enrichment are indicative of a marine environment during deposition of the Disrupted Beds.

4.2 Redox conditions during ironstone deposition

4.2.1 Cerium anomaly

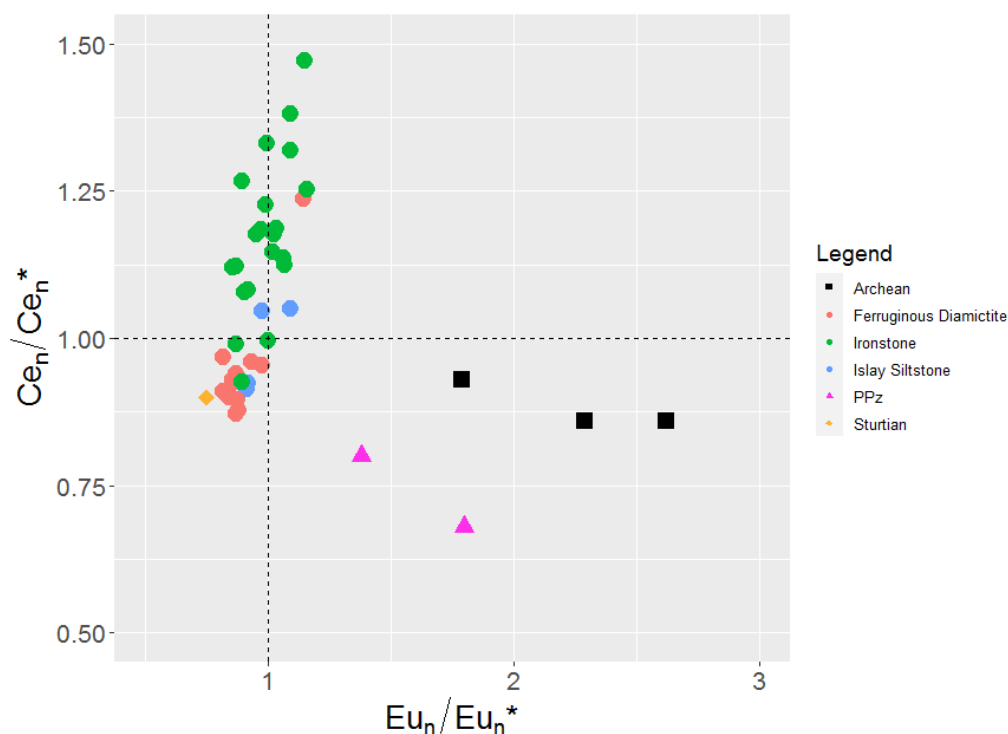


Fig. 40. Cerium and Eu anomalies in the Disrupted Beds compared to other BIFs. Dashed lines represent boundaries of anomalous behavior in the elements (>1).

Cerium is a useful indicator of paleo-redox conditions (Kato et al., 2006). Modern seawater is characterized by a negative Ce anomaly due to trivalent Ce readily oxidizing to tetravalent Ce, which is less soluble, and subsequently scavenged by particulates and falling out of solution (Bolhar et al., 2004; Kato et al., 2006) preventing long distance transport in seawater. In anoxic environments Ce remains in solution in seawater. It is apparent from Fig. 40. that there is a strong positive Ce anomaly in the PAF ironstones, indicating anoxic conditions during deposition. It is apparent that the Ce anomaly of the PAF ironstones is significant compared to other BIFs from the Proterozoic and Cryogenian. The presence of strongly negative Ce anomalies is an indication in the geologic record of the availability of free O_2 in the atmosphere and oceans, as shown in the modern seawater line in Fig. 33. This strongly positive Ce anomaly has not been observed in the NIF record and possibly points to specific basinal conditions leading to this extreme anoxia.

The behavior of Y across redoxclines is also well established in modern and late Paleoproterozoic basins (Bau et al., 1997; Planavsky et al., 2010). Strong positive Y anomalies

are reduced in magnitude when crossing redox boundaries, leading to less pronounced deviations of Y relative to seawater. This can be observed in Fig. 33. when comparing the pronounced Y anomaly in modern seawater to the minor positive Y anomalies in the PAF ironstones.

The Ce/Ce* and Y signals point to a likely redoxcline in the depositional basin in which the ironstones precipitated. Manganese and Fe can serve as particle shuttles across a redox boundary in marine systems, where the oxyhydroxide form readily adsorbs particulates such as Mo and Ce. The oxyhydroxides subsequently settle through the water column where they re-dissolve upon crossing the redoxcline, releasing adsorbed material and concentrating them in the sediment. A steady supply of replenished seawater in the upper column can lead to over-enrichment of redox sensitive trace metals such as Mo in anoxic bottom waters. The relative enrichment of these metals can be used to further examine the seawater chemistry during the time of deposition. (Algeo and Tribovillard, 2009)

4.2.1 U-Mo as an indicator of basin redox conditions.

Molybdenum and U are sensitive to redox conditions of a basin. Under oxidizing conditions Mo forms a soluble ion scavenged by Mn and to a lesser extent Fe oxides, and will typically show no enrichment in sediments deposited in O₂ rich environments (Morford et al., 2009). Under anoxic/euxinic conditions Mo forms the highly reactive thiomolybdate which is removed from the water column via adsorption onto Mn/Fe oxides as well as sulfides in minor euxinic conditions (Tribovillard et al., 2006; Algeo and Tribovillard, 2009). Therefore elevated Mo enrichment factor (MO_{EF}) can be seen as a sign of anoxia. Uranium fixation occurs under any anoxic/oxic conditions with no need of a particle shuttle. Thus the particle shuttle increases the rate of Mo fixation, while U fixation occurs at a steady rate and an increase of Mo over U indicates replenishment of seawater in the basin refreshing the Mo supply leading to overenrichment. Thus the covariation of these two trace metals can provide insight to the redox conditions and potentially the structure of the basin.

To measure the enrichments of the U and Mo, the standard enrichment factor calculation is used:

$$X_{EF} = \frac{\frac{X_{Sample}}{Al_{Sample}}}{\frac{X_{PAAS}}{Al_{PAAS}}}$$

Detectible enrichment is shown at a factor of X_{EF} >3 and substantial enrichment occurs at X_{EF} >10 (Algeo and Tribovillard, 2009). Using this enrichment factor model, Algeo and Lyons (2006) examined three modern oceanic basins: the Eastern Tropical Pacific (E.T.P.) for open marine conditions with mildly anoxic bottom waters, the Black Sea (B.S.) an isolated basin with total anoxia, and the Cariaco Basin (C.B.) a partially silled basin with anoxic bottom waters. Each of these basins has a distinct pattern of Mo/U enrichment factors. The E.T.P. is typified by low Mo/U ratios in sediments, typically below that of the Mo/U ratio in seawater. Uranium is typically enriched over Mo in these sediments. The B.S. is typified by Mo/U ratios below that of seawater, with stronger enrichment in U, while displaying some covariance. In the C.B. sediments show a strong enrichment in Mo/U over that of modern seawater, with a substantial enrichment of Mo/U. Therefore a pattern of enrichment of Mo above modern seawater can point to low oxygen conditions below a redoxcline.

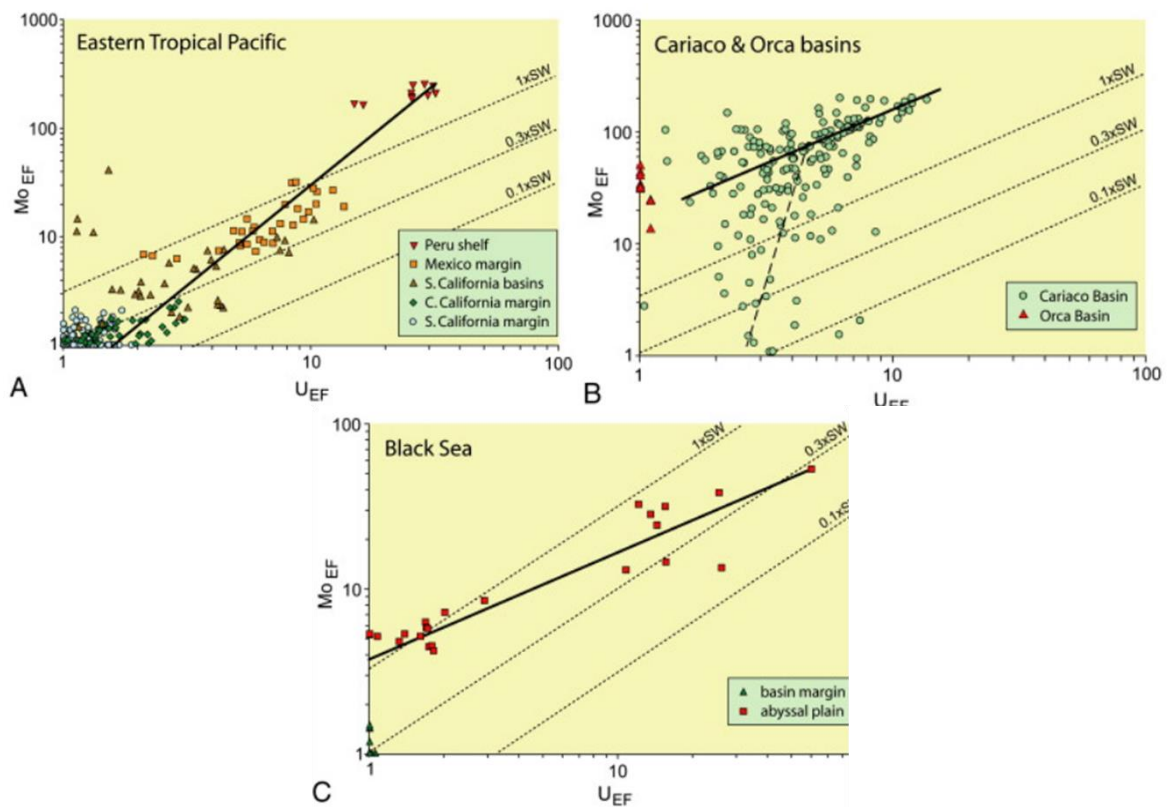


Fig. 41. Mo_{EF}/U_{EF} covariation in modern low to sub-oxic basins. Modified from Algeo and Tribouillard (2009)

Molybdenum and U enrichment factors (EF) have been used as proxies to compare the redox conditions across the modern ocean with those of Mesozoic oceans (Algeo and Tribouillard et al., 2009) and with Cryogenian oceans (Baldwin et al., 2012; Ye et al., 2018) as it is presumed unlikely that the processes leading to Mo_{EF}/U_{EF} have changed throughout geologic history.

Baldwin et al. (2012) found enrichment in Mo over U and interpreted this result as the Rapitan iron formation having formed in a partially restricted basin with a strong redoxcline. Of particular note in that study was the Fe concentrations at which the particulate shuttle was active. Whereas Mn is often established as acting as a shuttle for Mo, in the Rapitan basin there was no indication of a Mn shuttle, and instead Fe acted as a shuttle for Mo at middle concentrations (20-30% Fe_2O_3). This particular effect is also reflected in the PAF ironstones (Fig. 42.) where a strong correlation between Mo and Fe_2O_3 is seen in medium concentrations, indicating a similar particulate shuttle mechanism. No correlation between Mn and Mo was seen in the PAF, indicating Fe was responsible for Mo fixation across the redox boundary.

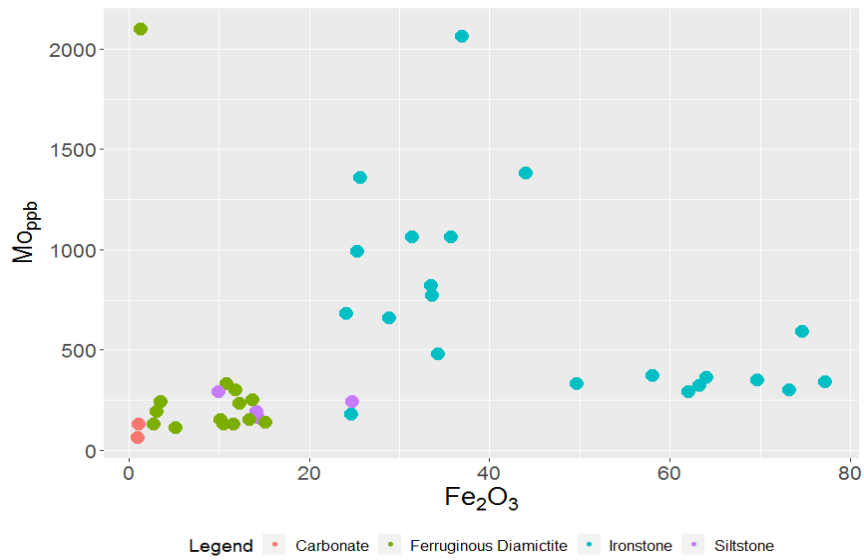


Fig. 42. Covariance of Mo and Fe₂O₃ in the PAF samples demonstrating increase in concentration of Mo at middle concentrations of Fe, similar to the Rapitan formation (Baldwin et al., 2012).

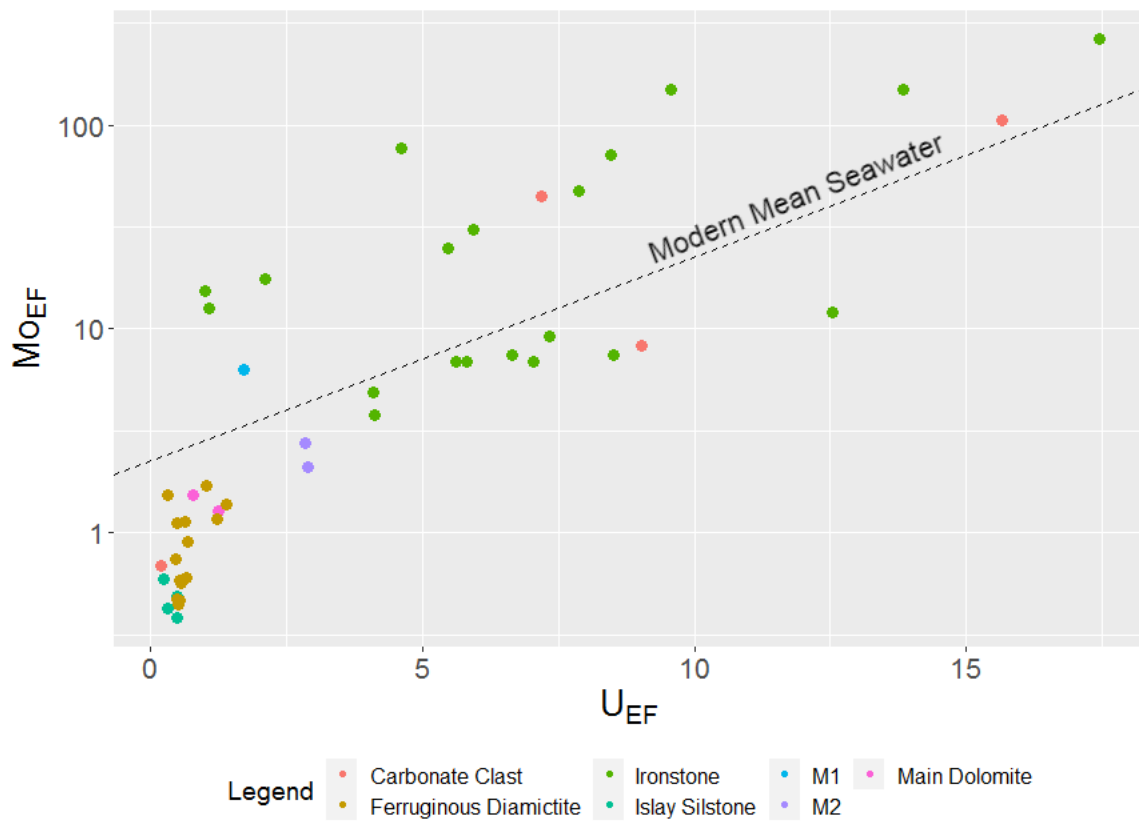


Fig. 43. Mo-U enrichment factor in the PAF. Ironstones generally trend above modern seawater showing enrichment in Mo over U.

Molybdenum and U enrichment factor trends in the studied samples are shown in Fig. 43. Clastic samples as well as the Main Dolomite demonstrate little enrichment in either Mo or U, a sign that the dominant signals in these rocks are controlled by detrital input or open marine conditions rather than redox control. The ironstone demonstrates strong enrichment in Mo over U similar to the modern partially restricted Cariaco Basin as demonstrated by Algeo and Tribovillard (2009). In the PAF this indicates that the ironstone deposition may have occurred in a partially restricted basin with Mo fixation controlled by an Fe particulate shuttle.

Evidence of the preferential enrichment of Mo over U in the PAF ironstone demonstrates that the basin was not entirely isolated from an open marine environment, as a constant renewal of the supply of Mo is needed to replenish sequestered Mo. While total oceanic anoxia is suggested in depositional models for Cryogenian iron formations (Hoffman et al., 1998; 2017) a fully anoxic basin would exhaust its supply of Mo relative to U, showing no enrichment in Mo with greater enrichment in U as demonstrated in the modern Black Sea (Fig.41C).

This partially restricted basin model for the PAF ironstones fits with the depositional environment of the Dalradian. The Dalradian is interpreted as having been deposited in an active continental rift, which provided accommodation for the thick glacial units (PAF) and post-glacial margin deposits (Jura quartzite). It is conceivable that this rifting could produce a horst and graben sequence through normal faulting, forming deeper silled depressions where a chemocline and bottom water could form under a thick sheet of floating ice and accumulate Fe before introduction of O₂ rich meltwaters.

4.3 Additional REY discussion.

The ironstones of the PAF shares many similarities with other NIFs. The REE profile of the ironstones of the Garvellachs shares the typical depletion in LREE and enrichment in HREE as expressed by the Pr/Yb ratio, and a lack of a Eu anomaly similar to other NIFs (Baldwin et al., 2012; Lechte et al., 2017). There are numerous formulae available for calculating the Eu anomaly expressed as Eu/Eu*.

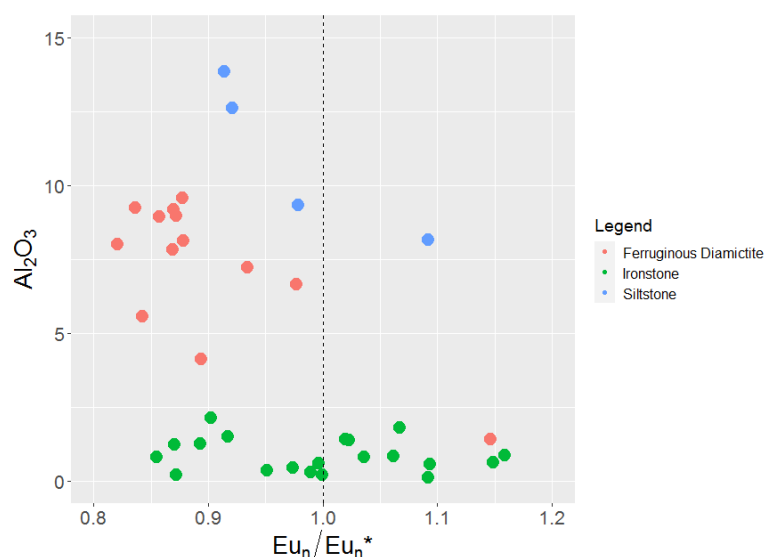


Fig. 44. Aluminum plotted against the Eu anomaly to evaluate detrital control over the Eu anomaly.

The choice of formula to use is dependent on relative over or under abundances of neighboring non-anomalous REEs (McLennon, 1989; Shields and Stille, 2001; Lawrence and Kamber 2006; Lawrence et al., 2006). The most commonly used equation for calculating the Eu anomaly in NIFs is that from Lawrence et al. (2006) who provide 2 equations to use based on relative abundances of either Gd or Nd. A simple visual method can be used to

determine the proper equation using a normalized REE plot based on the apparent behavior of

Eu relative to neighboring REEs, a positive trend necessitates the use of equation 8a, and a negative trend necessitates the use of equation 8b from Lawrence et al. (2006).

$$8a. Eu^* = (Sm_n^2 * Tb_n)^{\frac{1}{3}}$$

$$8b. Eu^* = Sm \left(\frac{Sm_n}{Nd_n} \right)^{\frac{1}{2}}$$

An examination of the REE spidergram in Fig. 33 shows that there are two trends based on the facies. The clastic rocks show a slight downward Eu trend, while the ironstone average shows a slight positive Eu trend relative to the surrounding elements and therefore equation 8a is used.

As Eu^{2+} can replace Ca in plagioclase phases during crystallization it been suggested that feldspar in the detrital fraction could be responsible for positive Eu anomalies in NIFs. (Weill and Drake, 1973; Klein and Beukes, 1993; Baldwin et al., 2012). Figure 44. shows that there is no correlation between the concentration of Al_2O_3 and the Eu anomaly indicating that the detrital component was not a significant factor in the elevated Eu anomaly in some samples.

The lack of Eu anomaly in the Garvellachs ironstones (mean 1.05) points to either a low temperature hydrothermal source for the Fe in NIFs (Klein and Beukes, 1993; Baldwin et al., 2012; Cox et al., 2013; Lechte et al., 2017), or Fe derived from glacially transported material.

4.4 Diagenetic and Metamorphic Effects on Geochemistry

4.4.1 Carbonate diagenesis

Diagenetic and metamorphic effects on rocks can alter the geochemical signatures of major and trace element geochemistry as well as induce the formation of dolomitic concretions and Fe/Mn oxide concretions (Mavotchy et al., 2016). Dolomite concretions are typically enriched in Mn by a factor of 3 when compared to primary carbonate beds (Mavotchy et al., 2016).



Fig. 45. Dolomite growths with siderite halos in diamictite sample G5

In the PAF the strong covariance between CaO, MgO and MnO implies a diagenetic influence on Mn values in carbonate bodies in the Disrupted Beds. The dolomite “blobs” as named by Spencer (1971) seen in Fig. 7A. showed enrichment above shale values of Mn, as did numerous diamictites with abundant carbonate clasts. The primary dolomite beds below and in the Disrupted Beds contain around ~0.10 wt.% MnO, while the dolomite from the disrupted dolomite bodies and outsized carbonate clasts from the Garvellachs range from ~0.3 to 0.5 wt.% MnO. This is an indication that diagenetic

fluids may have played a role in their formation. Minor enrichment in Fe is seen in the disrupted dolomite bodies on the Garvellachs, with higher Fe enrichment in the disrupted carbonate bodies at Beannan Buidhe (Ian Fairchild personal communication, 2020). Several outsized clasts of dolomite observed in the diamictites and siltstone facies show evidence of in-situ formation. In Fig. 45 two similar dolostone blobs are seen showing the typical light colored

core with siderite alteration extending into the matrix. The upper dolomite blob is notably truncated by an amphibolite clast and elongated grains show a preferred orientation pointing towards displacement growth of the dolomite blobs, pointing to their in-situ formation. The magnitude of Ce and Eu anomalies in the dolomite “clasts” and blobs from the diamictites show positive anomalies of similar magnitudes to the ironstones, while the Main Dolomite shows non-anomalous values (see appendix 8.1.4 for values). The similar magnitudes of these anomalies in the dolomite clasts and the ironstones points to co-genetic formation from the same fluid source, pointing to an authigenic origin for the disrupted dolomite bodies and the oversized carbonate bodies previously interpreted as clasts.

Dolomite concretions can form during diagenesis particularly in pore waters with excess alkalinity (Hoareau et al., 2009) and can form differing morphologies, from round to oval, or elongated bodies. Therefore this study suggests that disrupted dolomite bodies are not syndimentary deformation and are instead syn-diagenetic features. Diagenetic boudinage has been observed in Fe formations in the Hamersley Basin of Western Australia, where extensional movement created accommodation space for concretions to form. Thus the “disrupted” morphology of the Disrupted Beds need not be explained by submarine movement (Eyles and Januszczak, 2004) or ice sheet loading (Benn and Prave, 2006) but rather from diagenetic displacement growth of concretions bounded by less permeable Fe rich layers.

4.4.2 Diagenesis and hematite

EPMA analysis of hematite in the ferruginous diamictite units of the Disrupted Beds and samples from lower in M1 and in M2 were conducted for use as an internal standard for LA-ICP-MS analysis of the hematite. Unfortunately the REE concentrations in the hematite proved too low for analysis at the LA-ICP-MS at Stockholm University. Nonetheless, EPMA analysis showed that the hematite occurs as a solid solution with ilmenite, ranging up to ~2 wt.% with minor Ti in the ironstones. This differs from the hematite in Fe rich diamictites of M2, which show only trace amounts of Ti. Titanium concentrations in hematite shows contrasting trends when compared to whole rock TiO_2 values. In the Disrupted Beds Ti_{hem} shows a strong positive correlation with $\text{Ti}_{(\text{tot})}$ whereas in the M1 and M2 there is no correlation (Fig. 46).

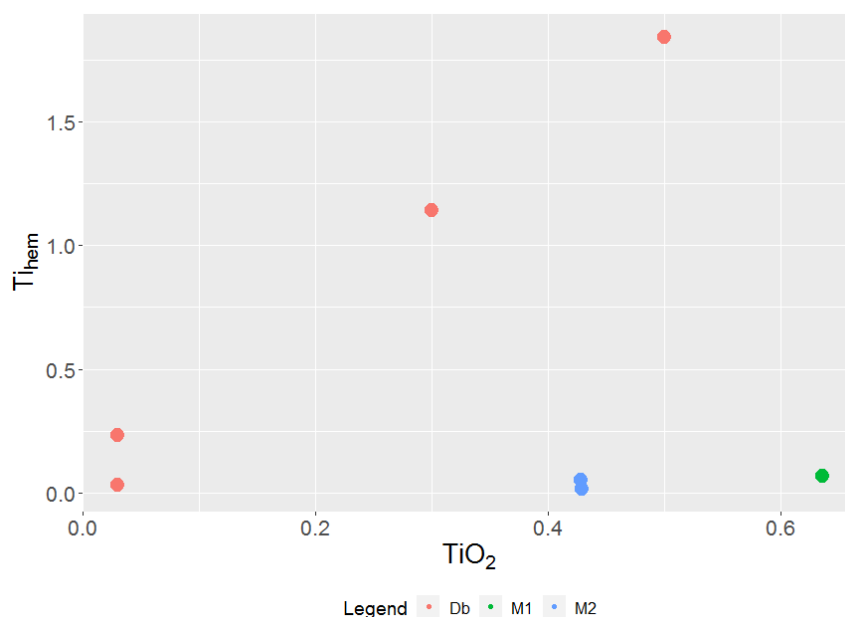


Fig. 46. Covariance of Ti content in whole rock versus Ti in hematite. Correlation is seen in the samples from the Disrupted Beds, while not observed in other Fe rich strata.

This indicates that Ti may have been mobilized from the detrital component of the diamictites during diagenesis in the Disrupted Beds, leading to the formation of the solid solution of ilmenite and hematite. The formation of hematite-ilmenite solid solution during diagenesis has been observed in modern anoxic Fe-rich sediments off the coast of western Africa (Dillon and Franke, 2009) which mirrors the apparent depositional setting of the Disrupted Beds. The lack of this trend in the hematite of M1 and M2 likely points to a non-authigenic origin for the hematite. Additionally, the morphological differences in the formation of the hematite in these beds, with hematite from the Disrupted Beds showing pore filling morphology as well forming as a cement between grains, whereas the hematite from the M1 and M2 beds displays a rounded morphology with larger average grain size (Fig. 28;29). Hematite in the samples from M2 can be observed enclosed entirely by cement minerals formed during diagenesis, further evidence of a detrital origin for this hematite.

These observations of the M2 hematite are at odds with the interpretation presented by Dahlgren (2020) who conducted principle component analysis of the Fe-rich rocks of M2 and concluded that based on the strong correlation of Fe and P that the Fe is not detrital in origin in the basal units of M2 as it is in the younger units of the PAF.

An explanation for these differences is that there is potentially a mixed origin for the hematite in the M2 samples, and that a selection bias occurred when selecting the hematite for EPMA analysis. Hematite crystals >40 μm were selected at random for LA-ICP-MS REE analysis to ensure that the crystals were large enough to be analyzed by the laser. This may have given a bias to larger detrital hematite in the samples and overlooked analysis of smaller, potentially authigenic hematite. These same criteria were used to select hematite crystals in the Disrupted Beds samples, however the consistent high-Ti results indicate differing origins for the hematite possibly reflecting the proposed shift in sediment provenance for M2 as proposed in Benn and Prave (2006). Based on the lack of Ti present in the hematite in the M2 basal units, this potentially detrital hematite is unlikely to be reworked Fe from the Disrupted Beds. An

additional factor may be a lack of a component in the diagenetic fluids of the M2 Fe-rich rocks capable of mobilizing Ti. Strongly reducing diagenetic fluids have been proposed to mobilize titanium from clastic material (Galvez et al., 2012) and differences in the composition of the diagenetic fluids during diagenesis of the Disrupted Beds and M2 may have played a role in the differing hematite compositions.

Siderite was observed in several ironstone (G23b; G25; G26) and ferruginous diamictite (G5, see Fig. 45.) samples in alteration zones along veins, which corresponds to the samples with the highest Mn values, implying that Mn, which forms rhodochrosite in solid solution with siderite, is an alteration product possibly related to fluid flow during diagenesis or metamorphism and not related to hydrothermal Fe sources.

4.5 Model for the formation of the ironstones and ferruginous diamictites of the Port Askaig formation.

4.5.1 Key Observations

To create a model for ironstone formation in the PAF an understanding of both the mineral and geochemical observations of the rocks must be synthesized with an understanding of the behavior of Fe in the oceans, and the environment of deposition during the Cryogenian. The ironstones of the PAF sit near the base of the Disrupted Beds on Eileach an Naoimh above a conglomerate and siltstone and are not seen throughout the Garvellachs, and are instead limited only to certain outcrops. The ironstones are dominantly composed of Fe and Si, and show some evidence of banding implying a low energy depositional environment with some clastic input, typical features of NIFs. The uppermost bed of ironstone is a breccia/diamictite of ironstone matrix and clastic debris, apparent evidence of reworking of the sediments by either debris flow or ice re-advance as evidenced by a preferred orientation of elongated clasts/grains (Fig. 26). Evidence of an anoxic depositional environment is seen in the ironstones based on Ce anomalies and evidence of a redoxcline shown by steep enrichment of Mo over U and above modern seawater enrichment of Mo. The limited extent of the ironstones within the PAF is an indicator that topography may have played a role in their formation. The ferruginous diamictites and siltstones occur throughout the Disrupted Beds and show evidence of authigenic hematite growth based on their pore filling morphology (Fig. 27) that continued during deposition of clastic material. With this evidence in mind the source of the Fe²⁺ and its oxidizing mechanism will now be examined.

4.5.2 Source of free Fe in the PAF depositional basin

The behavior of Fe in the modern ocean is fairly well understood and can be used as a proxy for Neoproterozoic ocean chemistry. Fe makes up ~3.5% of continental crust (Taylor and McLennan, 1985) and ~10% of MORB (Gale et al, 2014), however the concentration of Fe is several orders of magnitude lower in the ocean: ~0.6-0.8 nM in the North Atlantic and Pacific, and as low as ~0.3-0.4 nM in the Southern Ocean (Moore and Braucher, 2007). The primary sources of Fe in the modern oceans is from detrital input (riverine and aeolian) with hydrothermal activity contributing a lower amount of Fe. Due to the rapid rate at which ferrous iron oxidizes (minutes to hours) an oxygenated ocean prevents the formation of ferruginous seawater without anoxic conditions (Millero et al., 1987).

Numerous models have been put forth for the formation of NIFs: glaciogenic-hydrothermal models (e.g. Kirschvink 1992; Hoffman et al., 1998), glaciogenic-terrestrial Fe models (Baldwin et al., 2012), rift-related hydrothermal processes (e.g. Eyles and Januszczak, 2004; Freitas et al., 2011; Halverson et al., 2011) and later post-depositional Fe enrichment due to regional volcanism (Mrofka and Kennedy, 2011). Of these models, post-depositional enrichment can be immediately discounted in the PAF due to the presence of the “podded” ironstones on Eileach an Naoimh (see Fig. 23C) which display synsedimentary deformation and are intraclasts in the sediments overlying the ironstones and point to coeval formation of the Disrupted Beds and the iron deposition.

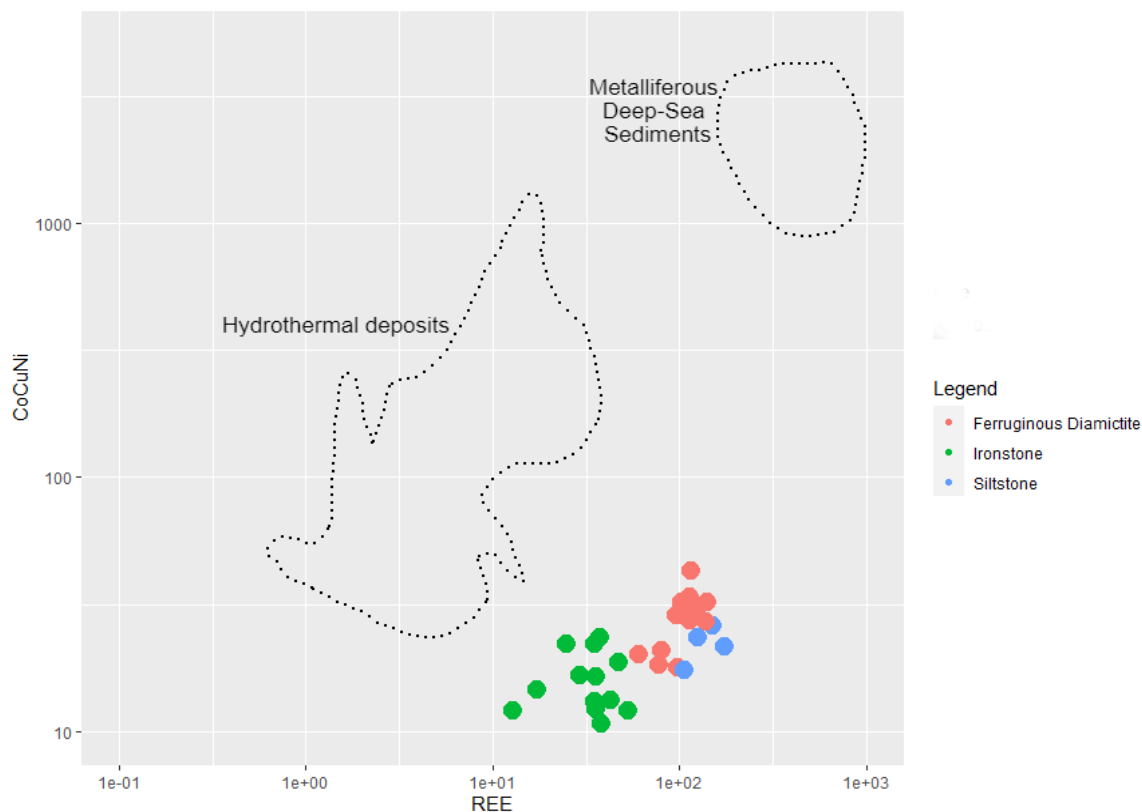


Fig. 47. Base metal versus REE content in the PAF compared to hydrothermal vent deposits

A hydrothermal iron source for NIFs does not necessitate high temperature exhalative fluid models as discussed by Halverson et al. (2011) and Cox et al. (2013) who invoke low temperature alteration of oceanic crust as a source of Fe into the Neoproterozoic oceans. A low temperature hydrothermal fluid is expected to have a lower Eu anomaly than high temperature fluids as trivalent Eu dominates over divalent Eu at temperatures of under 250°C (Sverjensky, 1984). Trace metal enrichment in the Garvellachs ironstones compared to high temperature hydrothermal fluids from mid-ocean ridges is shown in Fig 47. comparing of $\sum\text{CoCuNi}$ (ppm) and $\sum\text{REE}$ (ppm) of the Garvellachs samples compared to hydrothermal deposits and metalliferous deep-sea sediments.

The ironstones from Disrupted Beds show significantly lower $\sum\text{CoCuNi}$ than in typical hydrothermal deposits, with elevated $\sum\text{REE}$ concentrations in the diamictites and siltstones likely due to detrital input. This evidence also points to a lack of a high temperature hydrothermal source for the Fe. Table 2. shows a lack of Al and Ti with Fe also indicates a lack

of high temperature hydrothermal input of Fe as Fe from near field hydrothermal fluids will typically display high Al/Fe and Ti/Fe ratios (Cox et al., 2013).

The close association of NIFs with glacial diamictites with worldwide distribution thus points to a model that brings the effects of the hypothesized snowball Earth to the forefront. A frozen ocean with glaciated continents during the initiation of a “snowball” event would have limited input of fluvial and aeolian sediments, and therefore the best modern analogue to the Cryogenian oceans is the Southern Ocean surrounding Antarctica. Indeed, ice sheets in Antarctica and Greenland are a major source of iron flux in high latitude oceans as a result of the transport of glacial runoff with Fe fluxes of 0.06 - 0.17Tg and 0.4 – 2.5Tg respectively per annum (Hawkins et al., 2014). Antarctic glaciers have been shown to deliver ferrous iron to the ocean via photo-reduction of magnetite and goethite (Kim et al., 2010) and through microbial reduction in subglacial brines e.g. Blood Falls (Mikucki et al., 2009).

The absence of a clear hydrothermal signature in the ironstones and the lack of other evidence of contemporaneous hydrothermal activity in relation to the PAF indicates that the Fe source for the PAF ironstones is not likely related to any local rift related hydrothermal system. Therefore, the lack of a significant Eu anomaly in the ironstones points to either low temperature hydrothermal alteration of oceanic crust or glacially derived Fe. A dominantly glaciogenic source of Fe in NIFs is proposed by Baldwin et al. (2012) wherein iron originates from glacial erosion of bedrock during ice sheet advance, which is then reduced in an anoxic ocean system by microbial activity similar to the modern analogue of Blood Falls in Antarctica. A thorough study of the matrix of the PAF was conducted by Dahlgren (2020) which found that the matrix of the diamictites below M3 of the PAF is dominated by carbonate, which if the carbonates were dolomitized before the snowball event, may have provided a source of easily mobilized Fe into the basin.

4.6 Oxidizing mechanism

4.6.1 Sub- ice shelf model of ironstone formation

The oxidation mechanism that triggered the deposition of Fe formations after the Sturtian glaciation is currently unclear, however is one of the most important factors in understanding NIFs. According to the “hard snowball” theory, Sturtian ironstones are the “last gasp” of the snowball glaciation where the Fe rich ocean is rapidly oxidized and subsequently “rusts” (Hoffman et al., 1998; Hoffman and Schrag, 2002), explaining the occurrence of NIFs intercalated with the uppermost diamictite facies Sturtian glacial formations, and the method of delivery of the oxygen is an important component of understanding the nature of NIFs. The evidence of floating ice as well as anoxia during the formation of the Disrupted Beds (Spencer, 1971; Benn and Prave, 2006; Ali, 2017) leads this study to focus on models presented for sub-ice shelf deposition of ironstones and ferruginous diamictites.

There are two models presented by Lechte et al. (2015; 2017) for sub-ice shelf ironstone deposition demonstrated in Fig. 48. The first model is the brine pump model where melting and refreezing of sea ice near the terminus of the marine ice shelf and sea ice expels dense, highly saline, oxygen rich water which subsequently sinks and oxidizes the ferruginous pool. The lack of dropstones in ironstones is explained by the refreezing of the base of the ice shelf as less dense oxic water moves along the base trapping the clastic load. The second model is glacial meltwater outwash during the termination of the snowball event, which brings oxygen rich meltwater into the basin, as well as turbidity flows carrying sediment loads.

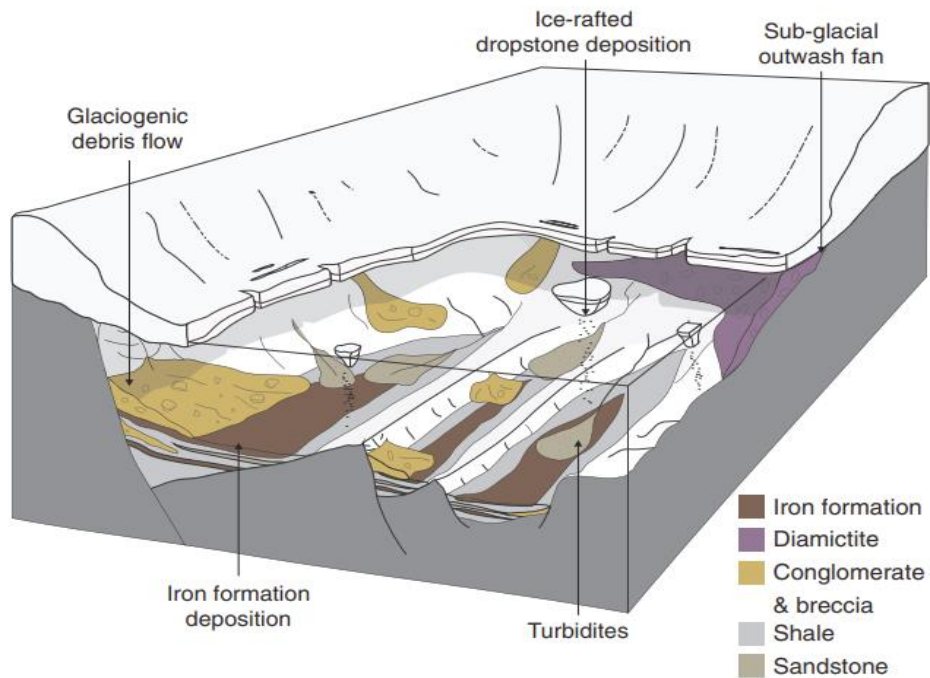
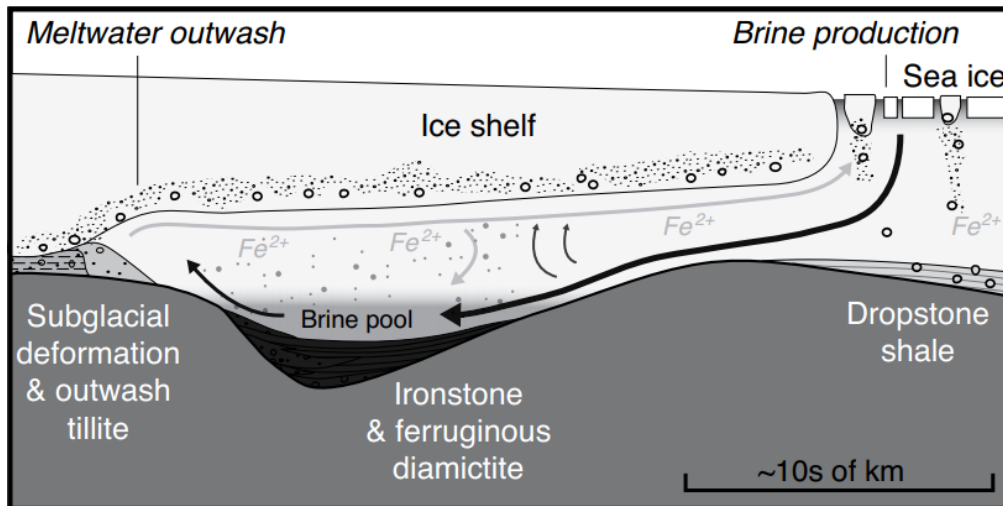


Fig. 48. Top: Model of NIF formation via a brine pump in the Chuos formation of Namibia from Lechte and Wallace (2016). Bottom: glacial meltwater outwash model from Lechte et al. (2018)

The “brine pump” model does not appear to fit the PAF ironstones, though testing the particular model is difficult. The presence of a detrital component in the ironstones represented by Al, K, Ti and Sc better fit the model of dense, oxic glacial meltwater flowing from the terminus of the glacier into the basin. Glacial meltwater contains a high proportion of suspended fine particulates, exemplified by the milky blue waters seen in modern glacial lakes that may have been incorporated into the ironstones.

The stages of iron formation are proposed to have occurred as follows: as the rate of melting increased, the lowest beds of the ferruginous diamictites formed in a sub-ice shelf environment. Correlation of the stratigraphy between the Disrupted Beds on Garbh Eileach and Eileach an Naoimh both point to low energy deposition at the base. The lowest beds sampled at Bealach an Tarabairt are two Fe rich units, a stratified diamictite with evidence of small scale turbidity flows that contains occasional outsized clasts interpreted as dropstones overlain by a thinly laminated siltstone with occasional dropstones also showing upwards fining of the sediments. Correlation of these two beds between Bealach an Tarabairt and Eileach an Naoimh places these low energy beds as forming before the ironstone, pointing to decreasing energy in the system enabling ironstone formation as dense detritus poor, oxygen rich meltwater entered the basin, oxidizing the Fe

The presence of podded ironstones and a breccia with an ironstone matrix at the top of the ironstones is evidence that mass sediment transport and ironstone deposition were either briefly coeval, or this unit represents a reworking of the ironstone sediment by subsequent ice advance, a process also observed in the Rapitan iron formation (Baldwin et al., 2016).

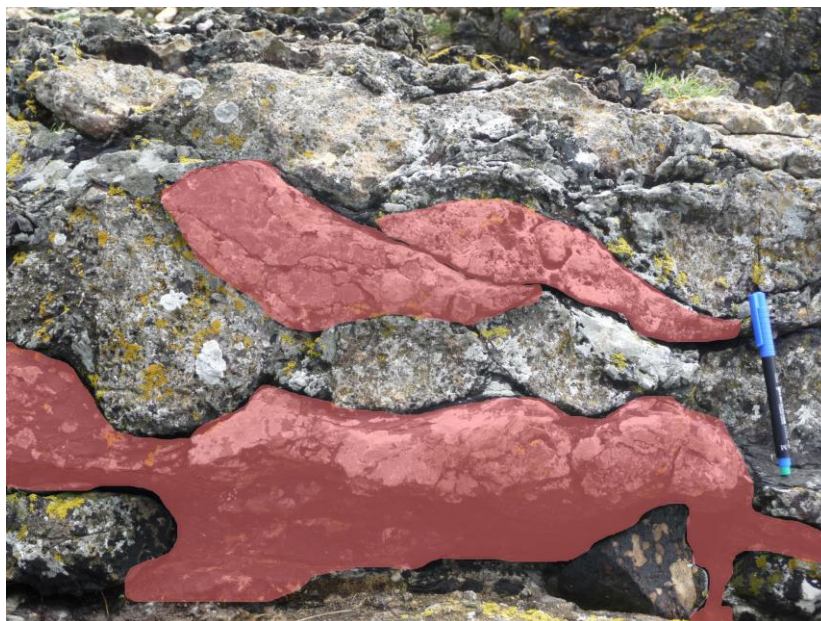


Fig. 49. Cartoon of Fig. 23C. highlighting the reworked podded ironstones (middle red) surrounded by carbonate (grey)

After the deposition of the ironstone there increase in sediment loading into the basin, and as noted previously a possible re-advance of the ice sheet. As melting continued the input of glaciogenic material increased forming the unstratified ferruginous diamictites and blue siltstones as the oxygenated water they carried with them removed Fe from the water, until the Fe^{2+} was exhausted, shifting towards deposition of non-ferruginous and dolostone matrix

diamictites of bed 3 and upwards. The increase in crystalline clasts starting around bed 3 as observed by Spencer (1971) and Benn and Prave (2006) indicate a shift to sediment sourced from distal ice sheet discharge and increased iceberg production, a sign of ice shelf retreat and opening of the seas, meaning the seawater would have reached equilibrium with atmospheric O₂ and free Fe was no longer available, or another disruption in Fe oxidation occurred.

The presence of pyrite beginning in the uppermost diamictite of the Disrupted Beds (G17; Fig 18D.) may point to a shift from anoxic to euxinic conditions after the exhaustion of Fe, which is supported by the apparent termination of authigenic hematite formation in Bed 3 of the Disrupted Beds. Abundant pyrite is observed in the Fe-rich samples collected from M2 identified as diagenetic by Dahlgren (2020), which points to euxinic conditions where sulfate reduction may have been occurring through bacterially mediated means. Wu et al. (2020) observed a similar cessation of Fe deposition coinciding with a shift towards pyrite rich beds immediately after the termination of the Xinju NIF in the Fulu formation of China.

Sulfate was depleted in the oceans during the Sturtian glaciation (Hoffman et al., 2017), and the reappearance of pyrite in the upper beds of the Disrupted Beds and later diamictites, combined with the increasing appearance of extra-basinal clasts and a shift in the detrital provenance of the matrix (Dahlgren, 2020) may point to increased riverine input delivering sulfate to the oceans as the terminating factor of authigenic Fe formation rather than exhaustion of the Fe budget, and strengthen the argument that the Great Breccia and Disrupted Beds are the primary snowball event stratigraphy.

When compared with previous interpretations of the processes forming the Disrupted Beds, this sub-ice shelf interpretation proves to be somewhat at odds with the interpretation of the Disrupted Beds as a sub-glacial or near shore depositional environment as iron formations are characteristic of low energy, deeper water (>100m) environments. Therefore, it is here proposed that the lowest units of the Disrupted Beds may represent a sub-ice shelf environment close to shore in a bathymetric low. This deeper water may have been a limited duration event during a transgressive period as ice sheets across the globe melted before isostatic rebound led to a shoaling of the water depth. Evidence of deep water is observed at the base of the Disrupted beds as shown in sample G3 and potentially in G4 (Fig 18A; C) where apparent turbidity flows are evident in the sediment. It is proposed here that these sediments were carried by mass flows from the base of the ice sheet down the slope of this depression, bringing with them oxygenated water, which oxidized Fe present in this basin. The extent of the ironstones is limited to the Disrupted Beds and the base of M2 of the southernmost island of the Garvellachs and to Islay, with minor occurrences on the island of A' Chuli (Fig. 16.) (Anthony Spencer, private communication) which appears to support that there was topographical constraint on their formation and may represent the deepest part of the basin.

4.6.2 Sub ice-sheet model for ironstone formation

Lechte et al. (2018) briefly proposed a third mechanism of ironstone formation where Fe oxidation occurs below a grounded ice sheet in sub-glacial cavities leeward of the grounding line and is examined briefly here. In this model these cavities contain glacial meltwater that is intruded by tidal action beneath the ice, providing a replenished source of Fe and seawater. This model fits with some aspects of the geochemistry of the PAF ironstones, particularly their limited extent, and evidence of grounded ice during some periods of the deposition of the Disrupted beds, however the geochemical data and evidence of floating ice does appear to

support this model. The strongly positive Ce anomaly (>1.1) in the ironstones is likely an indication of extreme anoxia a depositional sub-basin, whereas influx of seawater into a cavity filled with glacial meltwater that was already oxygenated would likely give a strong negative Ce anomaly. Therefore the proposed model of formation for the PAF ironstones invokes that of Baldwin et al. (2012) and Lechte et al. (2017) of a topographic low of strongly anoxic seawater below a redoxcline is the best fit for the formation of the PAF ironstones.

4.7 Do the Disrupted Beds represent a NIF?

NIFs associated with Neoproterozoic glaciations differ from the classic Archean and Paleoproterozoic BIFs. The banded nature of NIFs is typically poorly expressed, though there are some exceptions; e.g. the Rapitan and Holowilena ironstones (Lechte et al., 2017). Iron rich beds in NIFs are typically Fe-rich mud/siltstones and ferruginous diamictites (Cox et al., 2013). The Fe rich rocks of the Disrupted Beds of the PAF meet these qualifications, and share similar characteristics in their geochemistry to other NIFs: enrichment in P, lack of a Eu anomaly, superchondritic Y/Ho ratio, and positive Gd anomaly, however with some exceptions such as the strong positive Ce anomaly.

The ironstones of the Chuos formation of the Sturtian Usakos subgroup of Namibia, provide a reasonable comparison to the ironstones of the PAF. The Chuos ironstone formation is composed of laminated ironstones, ferruginous siltstone and ferruginous diamictite deposited above the Pulaco Tillite (Lechte et al., 2018). These ironstones are interpreted as having been deposited in a sub-ice shelf environment based on the presence of dropstones. These similarities in the varied nature of NIFs demonstrate that an NIF does not need to fit the ideal model of BIFs formed during the Archean and Paleoproterozoic, and the similarities between the ironstones of the Chuos formation and the PAF indicate that the Fe-rich facies of the Disrupted Beds reflect known NIFs.

The Disrupted Beds do not represent the beginning nor termination of Fe-rich strata in the PAF. The lowest identified bed Fe rich strata lies above the Great Breccia as a mudstone sequence overlying a dolostone approximately 1m above the Great Breccia and 3m below the Disrupted Beds on Islay (Dahlgren, 2018) and the uppermost Fe-rich strata reappear in M2 of the Garvellachs (Dahlgren, 2020). EPMA analysis showed that the origin of Fe-oxides in the other Fe-rich strata differ from that of the Disrupted Beds based on the lack of ilmenite in solid solution with hematite, pointing to a likely detrital origin of the analyzed hematite from M2. As noted previously, this is at odds with the results presented by Dahlgren (2020). The presence of an Fe-rich siltstone below D19 as well as potential ironstones bands observed in D19 indicate authigenic Fe formation occurred again after the cessation of Fe formation in the Disrupted Beds. The transition to low energy deposition of siltstones and ironstones at the base of M2 reflects the shift to low energy ironstone deposition occurring near the base of the Disrupted Beds. Thus the transgressive model of seawater delivering ferruginous waters is again invoked for potential authigenic Fe formation at the base of M2. The presence of pyrite may be explained by mixing of sulfate rich riverine water invoked in section 4.6.1 with the ferruginous seawater brought into the basin during the transgression. Further analysis of these Fe rich beds, including sampling of the potential ironstones described by Spencer (1971) is needed.

Later alteration of hematite to magnetite on Islay likely occurred due to the presence of reducing fluids during Caledonian metamorphism. The lack of apparent magnetite in the Fe rich rocks of the Garvellachs may point to stronger metamorphic alteration of the PAF on Islay by structurally controlled fluid flow due to proximity to the Islay anticline (Pitcairn et al., 2010; Skelton et al., 2015). A similar mechanism of metamorphic alteration of hematite to magnetite is proposed for the Chuos Formation (Lechte et al., 2018)

Thus, the evidence clearly indicates that the Fe-rich units in the Disrupted Beds represent a post-glacial NIF associated with the re-oxidation of ferruginous waters based on their

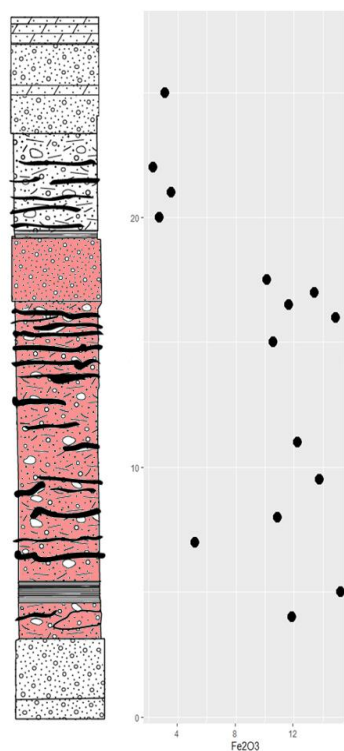


Fig. 50. Proposed extend of the NIF (red) of the Port Askaig Formation in the Disrupted Beds at Bealach an Tarabairt plotted against Fe content in the analyzed samples.

geochemistry. Therefore, in the context of the SEH, this study puts the extent of the post-glacial iron formation from the Ironstones on Eileach an Naoimh through the base of bed 3 of the Disrupted Beds. A tentative assignment of the base of M2 as a part of the NIF of the PAF is also given here with the caveat that additional study and field observations are required during future fieldwork.

Thus, the small “iron ore” bands of magnetite and beds of magnetite and hematite bearing siltstones at Beannan Buidhe and the Garvellachs described by Spencer (1971) and later interpreted as bearing Fe of detrital origin (Spence et al., 2016) have been shown by this study to likely be authigenic Fe formed during the post-snowball period. The near

universal occurrence of NIFs in Sturtian deposits provides further support for the assertion by Fairchild et al. (2018) that the PAF is a Sturtian rather than Marinoan deposit. Analysis of the xenotime present in the Disrupted Beds may provide a better constraint of the age of deposition.

4.8 Diagenetic or Hydrothermal Origin of Xenotime in the PAF

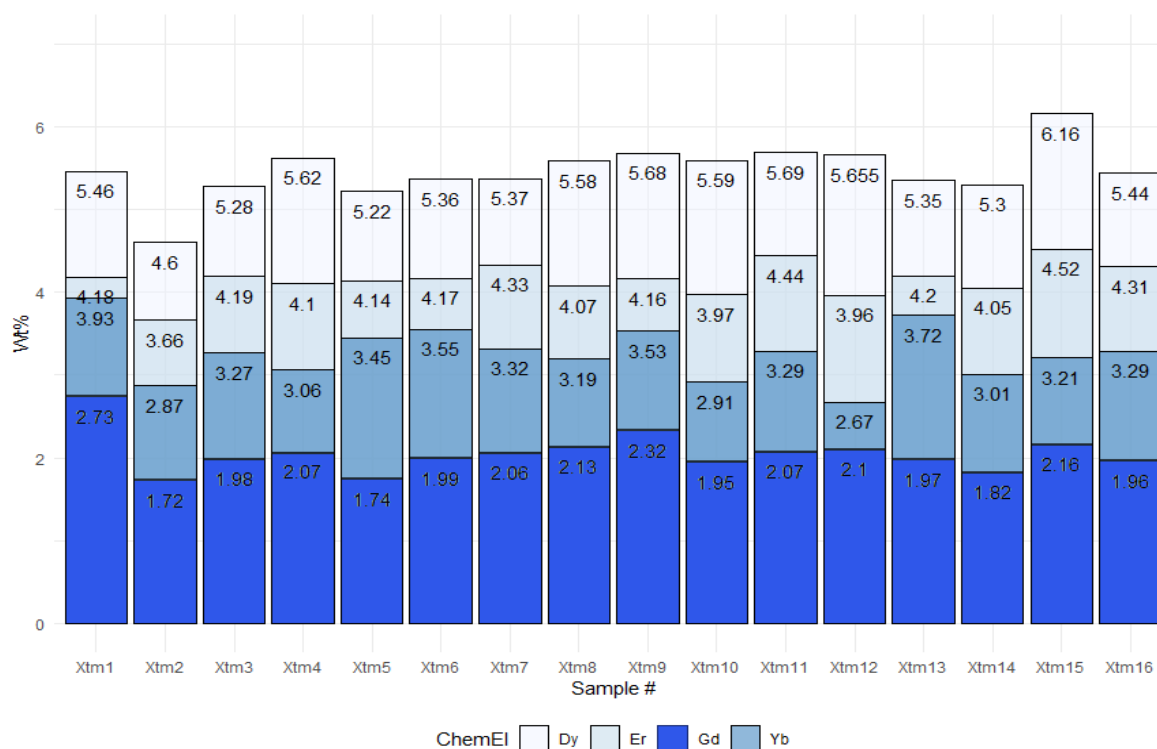


Fig. 51. Concentration of REE substituting for Y in the PAF xenotime in wt%. Xtm 1 is the core of the large rounded xenotime seen in Fig. 36B. and Xtm 2 is the rim.

Analysis of the morphology of monazite indicates a metamorphic and detrital origin for the studied grains. Therefore xenotime is the best candidate to conduct radiometric dating of the PAF. With the exception of three xenotime grains, including one large rounded grain interpreted as detrital, as well as one apparently nucleated on hematite, and one filling pore spaces, the remainder of the xenotime were associated with zircon, pointing to a clear authigenic origin. Temperatures during peak metamorphism on Islay were in the range of 400-470°C (Skelton et al., 1995), below the typical temperatures of xenotime dissolution and Pb loss (Cherniak 2006). REE values of the analyzed xenotime grains were normalized to chondrite values from Taylor and McLennan (1985). The trend shown in the normalized values shows enrichment in MREE and HREE over LREE, minor negative Eu anomaly, a slight positive Dy and Er anomaly.

When compared to xenotime from prior studies as shown in Fig. 53., the PAF xenotime shows a pattern similar to that of the diagenetic xenotime of the sedimentary Prichard formation of the Belt-Purcell Supergroup of Idaho, USA (individual curves) from Aleinikoff et al. (2015) and diagenetic xenotime from the Witwatersrand basin, South Africa (Kositcin et al., 2003). The PAF xenotime reflects the pattern of a slight negative Eu anomaly and slight positive Dy anomaly in the diagenetic xenotime of the Witwatersrand Basin. In metamorphic xenotime shown in Fig. 53B. a strong Gd anomaly is clear, as well as a steep decrease in abundances of M-HREE due to the “garnet” effect, where at higher metamorphic grades HREE is fractionated into garnet. Despite the name of this effect, the xenotime shown in Fig. 53B. were collected from greenschist facies rocks, indicating that the depletion of HREE begins at lower temperatures in xenotime formed during metamorphism (Aleinikoff et al., 2015) an indication

that the PAF xenotime was unlikely to have been formed or altered during post-diagenetic metamorphism.

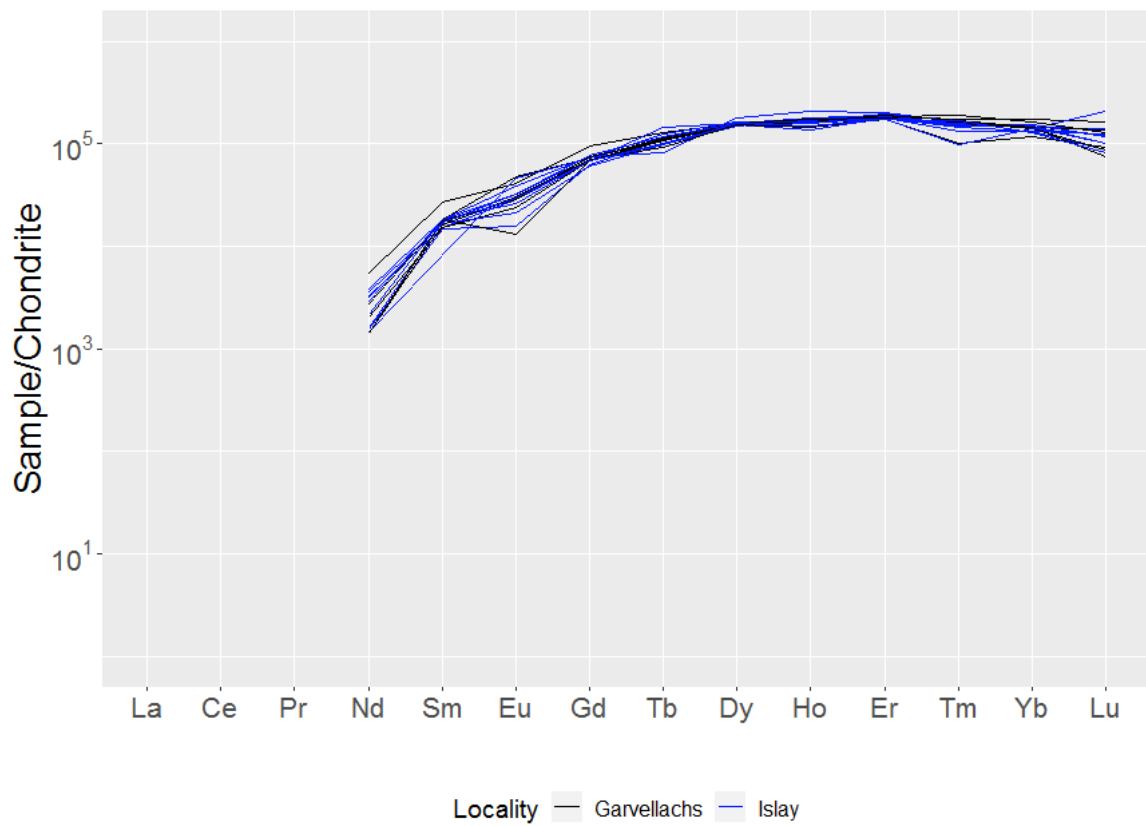


Fig. 52. REE content of analyzed xenotime normalized to chondrite. LREE < Nd were below detection limit.

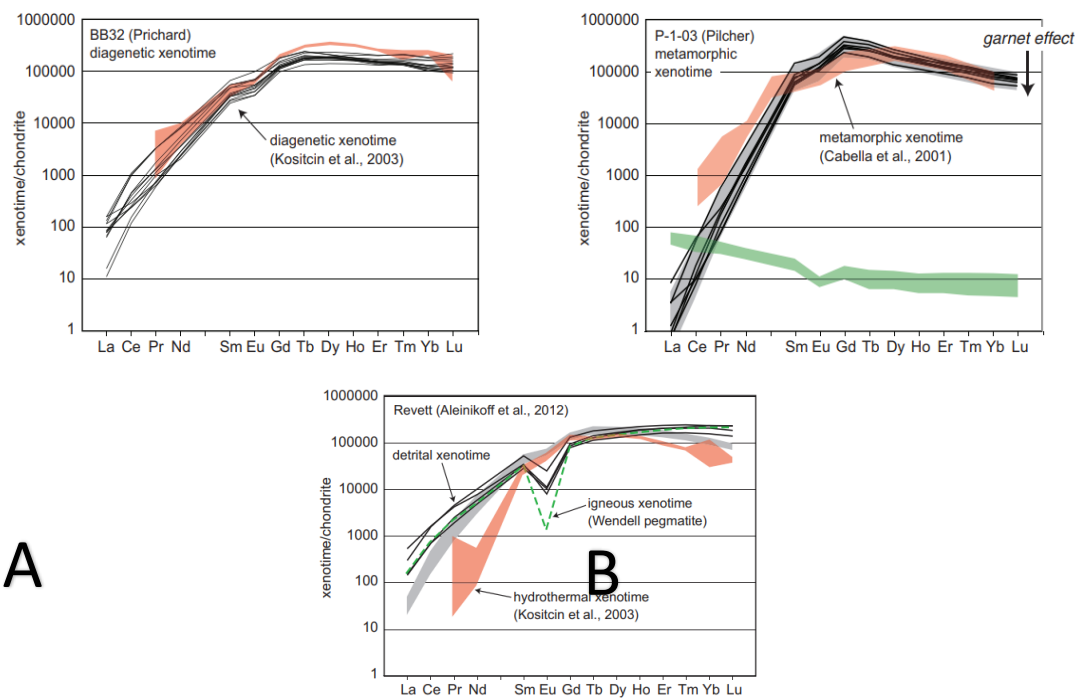


Fig. 53. Chondrite normalized REE patterns of xenotime of various origins. Modified from McNaughton and Rasmussen (2018).

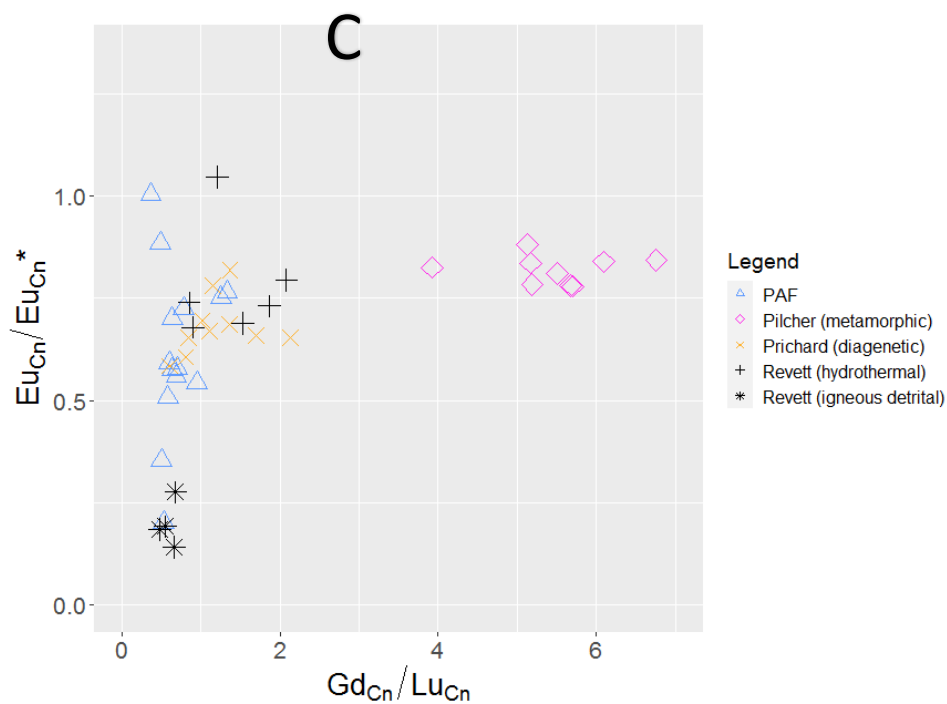


Fig. 54. REE ratios of xenotime from the PAF (blue triangles) compared to diagenetic, metamorphic (Aleinikoff et al., 2015) hydrothermal and igneous (Aleinikoff et al., 2012) xenotime. Samples from Aleinikoff et al. (2012; 2015) were normalized to the chondrite of Anders and Grevesse (1989) modified by Korotev, (1996) by the authors.

It is clear based on the REE chemistry that the xenotime in the PAF is unlikely to be metamorphic, further emphasized by the low Gd/Lu ratio. This is a common indicator of diagenetic or hydrothermal xenotime as shown in Fig. 54. Discriminating hydrothermal xenotime however, is less clear than proposed by Kositsin et al. (2003) as later studies of hydrothermal xenotime has shown that Dy can also be the dominant substitution over Y instead of Gd in hydrothermal xenotime. Therefore, as seen in the similarities in hydrothermal and diagenetic xenotime in Fig. 45. distinguishing between diagenetic and hydrothermal xenotime in the PAF is a murkier proposition. Hydrothermal xenotime shows similar morphology and affinity for nucleation on zircon as diagenetic xenotime as well as a rather similar geochemistry. This is not surprising as they form under similar conditions of phosphate and REE enriched pore waters.

In Fig. 53C. hydrothermal xenotime REE patterns are shown from two separate studies, one with a predominance of Dy over Gd from the Revett formation (Aleinikoff et al., 2012) and the other with a predominance of Gd over Dy (Kositsin et al., 2003). Each show an anomaly in the respective dominant substitution. Hydrothermal xenotime differs from diagenetic xenotime by typically expressing a very slight no Eu anomaly. The PAF xenotime shows a rather stronger negative Eu anomaly in most samples compared to hydrothermal xenotime, providing support for a diagenetic origin over hydrothermal. Hydrothermal xenotime additionally shows a steeper depletion in HREE relative to MREE when compared to diagenetic xenotime, particularly in Lu, providing a right dipping trend in the normalized diagrams. The xenotime of the PAF does not show this pattern, and instead has a flatter MREE to HREE trend similar to diagenetic xenotime patterns.

An additional confounding factor for determination of the genesis of the PAF xenotime, particularly for the samples from Beannan Buidhe, Islay, is the presence of base metal (Pb-Zn-Cu) mineralization dating to the Carboniferous (Cressely, 1996) as evidenced by the mine at the base of the study site shown in Fig. 13. This hydrothermal event may have also formed the xenotime, meaning a date would establish only base metal mineralization. Xenotime from hydrothermal base metal deposits show distinct patterns of enrichment in U dependent on the salinity of the hydrothermal fluids. In low to moderate salinity environments xenotime formed from these fluids typically contains very low (<500ppm) U (McNaughton and Rasmussen, 2018). Analysis of fluid inclusions sampled from the Ballygrant and Killslevy sulfide deposits pointed to low temperature and salinity fluids (Bolton and Parnell, 2005). The xenotime of the PAF has significantly higher concentrations of U (up to 2000ppm), a value more in line with diagenetic xenotime from other studies (McNaughton and Rasmussen, 2018). Finally, there is no appreciable difference in REE patterns based on sample location seen in the chondrite normalized pattern in Fig. 51. Both the Islay samples and the Garvellachs samples display nearly identical chondrite normalized values, where the Garvellachs have no observed base metal mineralization in the vicinity.

Based on these observations it appears likely, though not definitive that the xenotime in the PAF is diagenetic rather than hydrothermal or metamorphic in origin, and is expected to provide an age of diagenesis during dating with SIMS geochronology.

5. Conclusions:

- The ironstones of the Disrupted Beds show similarities to Archean, Paleoproterozoic and Neoproterozoic iron formations in their chemical composition and REE patterns. Like the earlier BIFs and contemporaneous NIFs, the PAF ironstones LREE depletion, positive Gd anomalies, and superchondritic Y/Ho ratios, all indicators of a preservation of seawater REE patterns that typifies BIFs. This indicates that the PAF ironstones are true chemically precipitated rocks
- The lack of any significant Eu anomaly in the ironstones is comparable to other NIFs and suggests a high temperature hydrothermal Fe-source is unlikely. Possible Fe sources are a low-temperature hydrothermal alteration of oceanic crust and Fe derived from sediments.
- A positive Ce anomaly is a sign of anoxic conditions in the depositional basin. Redox sensitive trace metals and a lower Y anomaly point to a redoxcline with an Fe-particle shuttle active at lower Fe concentrations. Mo-U enrichment may indicate a partially restricted marine depositional basin.
- Oxidation of the basin likely occurred through the low energy influx of glacial meltwater near the grounding line of the ice sheet before shifting to higher energy/higher sediment load regime.
- A trend of decreasing Fe in the ferruginous diamictites moving upwards through the Disrupted Beds through bed 3 points to either exhaustion of the Fe in the basin or a shift to a shift to euxinic conditions brought about by the reemergence of the hydrological cycle, delivering sulfur to the basin, indicated by pyrite formation occurring above bed 3.
- The iron rich diamictites of M2 contain hematite of differing morphology and pyrite is also abundant in these samples, indicating euxinic conditions. A lack evidence of authigenic formation in this study contrasting with previous work. More evidence is needed from the M2 Fe-rich beds to place them firmly into the framework of a NIF.
- The iron bearing strata of the Disrupted Beds show similar morphology to other NIFs including ferruginous diamictites and ferruginous siltstones with dropstones, and therefore should be considered a Neoproterozoic iron formation. Dating carried out on other Cryogenian formations bearing NIFs shows that they are limited to the Sturtian glaciation (716-659 Ma), pointing to a relative Sturtian date for the PAF based on the correlation of the NIF of Islay and the Garvellachs with other studied NIFs.
- Xenotime is present in the Disrupted Beds, and the enrichment of Dy over Gd and a flat HREE trend, along with U contents greater than 1000 ppm points to a diagenetic origin. If the Disrupted Beds are the product of the end stage of the glaciation, a minimum age of termination for the glaciation can be established.

6. Potential future studies

Several lines of inquiry arising from this study are a potential source of investigation for the future.

First and foremost is a detailed investigation of the sedimentology of the layers directly bounding the ironstones in the Disrupted Beds and M2. Due to the inability to conduct fieldwork in relation to this project, this is a vital aspect of building a more complete model of the formation of the ironstones.

LA-ICP-MS trace element analysis of REEs was attempted of hematite in samples from the ferruginous diamictites, and M1 and M2. The instrument at Stockholm University proved to lack the sensitivity to measure the low concentrations of REE in Fe oxides, and thus reattempting this experiment may prove useful to further test the seawater pattern of REE in Fe-oxides in the clastic samples of the PAF and strengthen the argument that hematite from M2 is detrital in origin.

Isotopic studies of $\delta^{56}\text{Fe}$ after Cox et al. (2016) may help to further constrain the source of Fe in the system by looking for other signs of hydrothermal Fe.

A full geochemical examination of the carbonate bodies in the Disrupted Beds, including the disrupted carbonate bodies and large clasts should be conducted to provide a history of their formation.

7. Acknowledgements

This project could not have been conducted without the help of advisor Iain Pitcairn, who collected the samples and helped to guide this work. Other thanks are given to Anthony Spencer, whose tireless work on the PAF continues to inspire new generations of geologists to shed light on these fascinating rocks. Andreas Karlsson of the Swedish Natural History Museum is thanked for his assistance with the SEM and EDS analysis, and Kerstin Lindén is thanked for her work in preparation of sample mounts. Jaroslaw Majka of Uppsala University is thanked for his assistance with the EPMA analysis of hematite. Finally, fellow Stockholm University students Martin Dahlgren is thanked for his input and samples provided, and Charlotte Fredriksson, who despite her best efforts could not get the hematite to yield its secrets to the ICP-MS.

This work was funded in part by a Bolin Centre for Climate Research RA-6 grant.

8. Appendices

8.1 Whole rock analysis data

8.1.1 Major oxide data

	SiO ₂	Al ₂ O ₃	Fe ₂ O ₃	CaO	MgO	Na ₂ O	K ₂ O	TiO ₂	MnO	P ₂ O ₅
	%	%	%	%	%	%	%	%	%	%
Is-1	56.7	12.6	14.2	1.71	2.43	0.11	4.29	0.81	0.03	0.2
Is-2	55.9	13.85	14.35	2.08	2.74	0.12	4.74	0.9	0.02	0.22
Gaa	26.9	1.28	58.1	4.12	1.81	0.03	0.47	0.26	0.09	0.9
Gab	66.9	0.31	25.7	2.78	1.0	0.01	0.09	0.03	0.05	0.95
G1	9.1	1.46	1.03	27.8	18.55	0.32	0.03	0.07	0.06	0.03
G3	45.2	5.56	11.85	11.1	6.92	1.02	0.57	0.3	0.15	0.41
G4	41.7	7.84	15.2	9.86	6.88	0.07	2.61	0.48	0.19	0.28
G5a	40.7	7.23	5.19	12.6	8.73	0.07	2.64	0.37	0.26	0.09
G5b	18.9	0.26	2.33	24.3	16.0	0.01	0.02	0.01	0.5	0.03
G6	53.5	9.19	10.85	6.22	4.93	0.57	2.98	0.5	0.13	0.17
G7a	51.6	8.93	13.75	6.36	4.81	0.07	2.73	0.47	0.12	0.26
G7b	15.2	0.54	2.1	25.3	16.75	0.02	0.03	0.02	0.52	0.01
G8	49.2	9.57	12.25	6.87	5.28	0.11	3.33	0.5	0.12	0.24
G10	47.8	9.24	11.65	8.33	6.14	0.07	2.87	0.53	0.2	0.23
G11	48.1	8.14	10.15	8.73	6.49	0.08	2.45	0.45	0.17	0.18
G12	10.5	0.62	1.36	26.5	18.05	0.28	0.02	0.03	0.43	0.03
G15	54.7	6.66	3.52	9.5	6.89	0.05	1.59	0.33	0.07	0.11
G17	30.7	5.11	3.09	17.65	11.7	0.71	1.31	0.24	0.07	0.09
G18	54.1	8.98	10.55	6.13	4.89	0.43	3.05	0.5	0.12	0.23
G20	43.4	8.02	13.4	9.5	6.92	0.75	2.4	0.48	0.21	0.23
G21	58.1	0.45	31.4	3.08	1.77	0.01	0.15	0.03	0.1	0.32
G22	29.7	2.13	49.7	5.8	3.44	0.02	0.82	0.3	0.2	0.64
G23b	59.0	0.36	33.6	2.73	1.58	0.01	0.1	0.03	0.08	0.27
G24	23.2	1.25	62.1	3.91	2.11	0.02	0.45	0.37	0.15	0.55
G25	23.3	1.52	64.1	3.03	1.44	0.01	0.58	0.18	0.09	0.81
G26	22.0	0.81	73.3	1.2	0.47	0.01	0.22	0.16	0.03	0.48
G27	71.4	0.21	25.3	0.66	0.26	<0.01	0.06	0.02	0.01	0.22
G29a	31.6	4.14	24.7	11.2	7.49	1.27	0.36	0.29	0.28	0.29
G29b	17.4	3.21	2.77	23.2	15.7	1.49	0.19	0.03	0.55	0.03
G30	57.7	0.62	34.3	2.03	1.08	0.01	0.18	0.02	0.03	0.38
DL-01-09	49.8	9.33	24.8	2.63	2.42	0.13	3.35	0.68	0.08	0.16
DI-02-09	63.2	8.17	9.98	4.35	3.3	0.13	2.81	0.44	0.05	0.15
G2	16.35	1.4	1.18	24.1	16.65	0.42	0.21	0.07	0.11	0.01
G14	11.5	1.41	2.74	26.0	17.1	0.02	0.39	0.04	0.32	0.03
G21a	47.0	0.88	33.5	5.57	3.4	0.02	0.29	0.07	0.18	0.27
G23a	53.2	0.57	35.7	4.06	1.98	0.02	0.11	0.09	0.1	0.76
G24a	16.7	1.42	74.7	2.15	0.86	0.03	0.54	0.23	0.05	0.76
G24b	32.3	1.82	44.0	6.72	4.21	0.12	0.7	0.15	0.26	0.42
G25b	25.7	1.4	63.3	3.15	1.65	0.02	0.52	0.39	0.11	0.58
G26a	17.75	0.82	77.2	1.11	0.44	0.02	0.2	0.18	0.03	0.42
G26b	23.1	0.84	69.7	1.57	0.67	0.01	0.22	0.12	0.05	0.49
G27a	68.5	0.23	28.9	0.51	0.16	0.01	0.06	0.02	0.01	0.22
G28	58.2	0.64	24.1	5.64	3.26	0.01	0.23	0.05	0.16	0.48
G30a	57.0	0.13	37.0	1.94	0.97	<0.01	0.01	0.01	0.03	0.32

8.1.2 Trace element data

Sample	Sc	V	W	Zr	Mo	U	Ni	Co	Cu
	ppm	ppm	ppm	ppm	ppm	ppm	ppm	ppm	ppm
Is-1	15.1	134.5	0.448	139.5	0.19	1.1	13.15	4.21	8.55
Is-2	16.55	145.0	0.45	157.0	0.16	1.21	12.55	3.66	5.21
Gaa	4.47	105.5	1.375	81.3	0.37	1.71	8.0	2.74	1.4
Gab	1.73	43.2	0.879	12.2	1.36	0.5	5.63	1.305	2.21
G1	2.15	6.5	0.146	20.2	0.06	0.34	15.45	2.79	1.59
G3	5.08	80.0	0.28	83.7	0.3	1.04	13.45	3.34	1.44
G4	9.29	68.8	0.482	97.4	0.14	0.81	23.2	6.14	2.74
G5a	7.43	46.6	0.412	68.2	0.11	0.67	17.5	6.69	4.34
G5b	1.98	2.9	0.023	12.7	0.38	0.35	11.6	11.0	4.32
G6	9.59	63.1	0.356	93.8	0.33	1.07	20.7	6.61	2.17
G7a	8.48	69.8	0.301	86.4	0.25	1.1	15.75	7.36	19.9
G7b	1.64	9.6	0.036	15.9	0.14	0.88	12.3	11.0	6.87
G8	8.98	74.4	0.414	89.9	0.23	0.83	20.3	5.23	1.45
G10	10.3	74.0	0.41	93.5	0.13	0.88	21.4	7.61	3.12
G11	8.62	68.1	0.365	75.4	0.15	0.81	19.65	5.81	1.82
G12	1.36	2.2	0.034	12.0	2.1	1.8	7.7	13.35	2870.0
G15	5.66	38.8	0.233	53.0	0.24	0.59	7.35	2.61	10.8
G17	4.76	25.5	0.22	57.7	0.19	1.15	5.22	1.61	4.24
G18	8.79	60.8	0.366	87.1	0.13	0.86	21.2	7.73	4.64
G20	9.0	66.5	0.313	84.7	0.15	0.94	21.2	7.84	2.65
G21	2.32	63.7	0.998	42.2	1.06	0.37	6.75	1.65	6.13
G22	7.71	116.5	1.345	67.6	0.33	1.6	14.3	3.16	1.11
G23b	1.6	75.7	0.964	64.4	0.77	0.53	7.73	1.61	2.71
G24	5.25	139.5	1.485	94.2	0.29	1.93	9.44	2.29	1.29
G25	4.96	144.0	2.57	83.1	0.36	1.85	6.25	1.515	0.73
G26	2.61	136.0	2.89	64.2	0.3	1.79	20.1	1.045	0.86
G27	1.77	40.0	0.726	29.9	0.99	0.53	5.16	0.821	1.65
G29a	5.55	79.8	0.221	89.2	0.18	1.05	12.6	4.04	1.23
G29b	5.23	3.8	0.04	14.4	0.07	0.11	10.2	4.98	1.33
G30	0.96	87.4	0.75	105.0	0.48	0.61	2.56	0.599	1.85
DL-01-09	9.24	180.0	0.404	115.0	0.24	1.03	14.25	5.03	4.11
DI-02-09	9.03	75.2	0.301	76.9	0.29	0.72	9.96	3.38	4.12
G2	2.57	4.9	0.127	26.2	0.13	0.38	11.9	3.14	0.63
G14	3.56	9.7	0.061	12.4	0.13	0.15	10.85	8.23	1.06
G21a	4.04	75.3	0.935	53.5	0.82	0.31	11.1	3.52	1.88
G23a	1.91	91.8	1.37	68.2	1.06	1.18	11.15	2.77	2.53
G24a	4.13	165.5	3.73	79.5	0.59	2.78	6.43	1.35	0.81
G24b	8.48	104.5	1.28	48.6	1.38	0.68	8.92	3.78	0.57
G25b	5.14	145.5	1.495	61.3	0.32	2.01	8.95	2.33	0.73
G26a	2.86	151.0	3.13	90.0	0.34	2.01	20.2	1.22	0.54
G26b	2.93	140.0	3.06	79.4	0.35	1.7	21.2	1.435	0.66
G27a	1.97	52.0	0.73	40.1	0.66	0.63	4.37	0.606	0.87
G28	3.32	41.5	0.738	92.4	0.68	0.47	7.06	3.06	0.61
G30a	0.84	84.1	0.896	127.5	2.06	0.79	3.41	0.845	1.86

8.1.3 REE data

Sample	Sample Description	La ppm	Ce ppm	Pr ppm	Nd ppm	Sm ppm	Eu ppm
Is-1	Islay Siltstone	31.2	65.3	7.69	28.6	5.09	0.923
Is-2	Islay Siltstone	37.0	76.2	9.05	33.6	5.92	1.045
Gaa	Ironstone	3.26	10.15	1.58	7.91	2.43	0.537
Gab	Ironstone	2.36	7.9	1.295	6.55	1.96	0.476
G1	Main Dolomite	6.4	13.8	1.685	6.55	1.29	0.272
G3	Ferruginous Diamictite	16.05	33.0	3.92	14.45	2.53	0.457
G4	Ferruginous Siltstone	21.2	43.3	5.24	19.2	3.55	0.65
G5a	Ferruginous Diamictite	20.2	41.7	4.72	17.55	3.05	0.597
G5b	Carbonate Body	2.2	6.57	1.01	5.52	2.03	0.548
G6	Ferruginous Diamictite	25.4	52.5	6.25	23.4	4.36	0.752
G7a	Ferruginous Diamictite	23.7	49.4	5.78	21.5	3.98	0.711
G7b	Carbonate Body	3.06	7.98	1.13	5.53	1.875	0.502
G8	Ferruginous Diamictite	31.4	62.4	6.98	24.9	3.91	0.65
G10	Ferruginous Diamictite	29.5	60.3	7.17	26.6	5.0	0.836
G11	Ferruginous Diamictite	24.6	49.6	5.81	21.0	3.43	0.603
G12	Disrupted Dolomite	3.59	11.05	1.485	7.13	2.06	0.472
G15	Ferruginous Diamictite	17.2	36.3	4.04	14.85	2.47	0.483
G17	Carbonate Diamictite	14.15	30.6	3.72	13.95	3.02	0.565
G18	Ferruginous Diamictite	23.7	49.1	5.75	21.5	3.91	0.701
G20	Ferruginous Diamictite	22.3	46.6	5.47	20.8	4.22	0.74
G21	Ironstone	2.24	5.7	0.777	3.52	0.967	0.228
G22	Ironstone	6.66	16.55	2.24	9.65	2.43	0.529
G23b	Ironstone	1.565	4.08	0.588	2.73	0.71	0.167
G24	Ironstone	4.19	11.3	1.61	7.26	2.04	0.435
G25	Ironstone	6.15	15.05	2.08	9.07	2.49	0.549
G26	Ironstone	2.97	8.05	1.125	5.02	1.395	0.294
G27	Ironstone	2.62	7.86	1.22	5.39	1.22	0.242
G29a	Ironstone Matrix Diam	19.8	41.4	4.93	18.45	3.28	0.617
G29b	Carbonate Clast	7.03	16.55	2.13	9.12	2.35	0.524
G30	Ironstone	1.245	4.14	0.5	2.26	0.556	0.13
DL-01-09	Islay Siltstone	24.8	50.6	5.91	23.3	3.43	0.65
DI-02-09	Islay Siltstone	19.3	39.6	4.88	19.8	3.3	0.759
G2	Main Dolomite	6.47	15.2	2.01	8.99	1.965	0.43
G14	Ferruginous Diamictite	3.78	10.65	1.68	8.37	2.56	0.754
G21a	Ironstone	2.57	6.32	0.881	4.15	1.01	0.292
G23a	Ironstone	2.38	7.38	1.185	6.15	1.68	0.435
G24a	Ironstone	6.27	15	2.12	9.62	2.24	0.561
G24b	Ironstone	3.57	9.02	1.325	6.07	1.54	0.423
G25b	Ironstone	5.06	12.75	1.82	8.41	2.06	0.518
G26a	Ironstone	3.24	8.35	1.19	5.52	1.33	0.342
G26b	Ironstone	3.1	8.18	1.245	5.84	1.53	0.401
G27a	Ironstone	2.7	7.72	1.24	5.59	1.2	0.279
G28	Ironstone	2.07	6.23	0.978	5.3	1.59	0.469
G30a	Ironstone	0.994	3.59	0.421	1.91	0.357	0.1

	Gd	Tb	Dy	Y	Ho	Er
Sample	ppm	ppm	ppm	ppm	ppm	ppm
Is-1	3.65	0.47	2.43	13.55	0.466	1.355
Is-2	4.07	0.516	2.68	14.7	0.511	1.55
Gaa	2.75	0.446	2.73	14.45	0.539	1.49
Gab	2.14	0.351	2.14	10.95	0.417	1.07
G1	1.03	0.16	0.958	5.95	0.196	0.536
G3	2.03	0.302	1.8	10.7	0.366	1.11
G4	2.73	0.402	2.44	14.15	0.499	1.475
G5a	2.25	0.34	1.98	12.25	0.413	1.21
G5b	2.62	0.455	2.88	17.85	0.585	1.65
G6	3.04	0.412	2.44	13.5	0.482	1.41
G7a	3.05	0.436	2.42	13.2	0.485	1.345
G7b	2.07	0.351	2.13	14.5	0.439	1.225
G8	2.37	0.322	1.865	10.6	0.376	1.08
G10	3.48	0.484	2.72	15.7	0.541	1.58
G11	2.43	0.333	2.01	11.35	0.41	1.165
G12	2.18	0.362	2.31	14.0	0.465	1.36
G15	1.645	0.24	1.41	8.0	0.287	0.846
G17	2.61	0.44	2.79	15.8	0.55	1.57
G18	3.0	0.411	2.36	12.65	0.462	1.345
G20	3.24	0.499	2.94	15.9	0.609	1.705
G21	1.055	0.166	1.105	6.65	0.226	0.641
G22	2.59	0.413	2.62	15.6	0.531	1.49
G23b	0.8	0.13	0.816	4.77	0.166	0.462
G24	2.19	0.363	2.3	13.2	0.464	1.375
G25	2.65	0.419	2.61	14.95	0.534	1.435
G26	1.565	0.253	1.58	9.2	0.328	0.971
G27	1.115	0.174	1.095	5.72	0.234	0.652
G29a	2.53	0.37	2.2	15.25	0.458	1.305
G29b	2.19	0.375	2.4	15.4	0.517	1.525
G30	0.565	0.087	0.556	4.02	0.12	0.33
DL-01-09	0.65	0.302	1.605	10.2	0.331	0.977
DI-02-09	0.759	0.373	1.975	11.35	0.383	1.075
G2	0.43	0.273	1.625	10.55	0.331	0.909
G14	0.754	0.526	3.26	21.1	0.678	1.9
G21a	0.292	0.19	1.285	9.4	0.287	0.772
G23a	0.435	0.27	1.715	10.35	0.34	0.909
G24a	0.561	0.402	2.41	13.85	0.496	1.36
G24b	0.423	0.318	2.0	13.55	0.445	1.215
G25b	0.518	0.371	2.21	14.0	0.465	1.28
G26a	0.342	0.246	1.555	9.13	0.325	0.989
G26b	0.401	0.279	1.795	10.85	0.384	1.03
G27a	0.279	0.183	1.09	6.12	0.229	0.64
G28	0.469	0.326	2.01	13.95	0.44	1.215
G30a	0.1	0.073	0.494	3.43	0.096	0.294

	Tm	Yb	Lu	ΣREE
Sample	ppm	ppm	ppm	ppm
Is-1	0.223	1.62	0.27	162.837
Is-2	0.244	1.8	0.297	189.183
Gaa	0.198	1.335	0.192	49.997
Gab	0.127	0.795	0.101	38.632
G1	0.075	0.578	0.088	39.568
G3	0.159	1.155	0.177	88.206
G4	0.227	1.585	0.248	116.896
G5a	0.175	1.255	0.189	107.879
G5b	0.23	1.575	0.216	45.939
G6	0.217	1.54	0.237	135.94
G7a	0.194	1.355	0.211	127.767
G7b	0.175	1.175	0.172	42.314
G8	0.162	1.18	0.189	148.384
G10	0.229	1.69	0.257	156.087
G11	0.178	1.295	0.198	124.412
G12	0.181	1.185	0.164	47.994
G15	0.133	0.842	0.13	88.876
G17	0.222	1.495	0.217	91.699
G18	0.198	1.395	0.222	126.704
G20	0.243	1.8	0.27	127.336
G21	0.097	0.619	0.088	24.079
G22	0.196	1.385	0.206	63.09
G23b	0.062	0.469	0.073	17.588
G24	0.205	1.4	0.202	48.534
G25	0.208	1.37	0.21	59.775
G26	0.136	0.996	0.162	34.045
G27	0.085	0.59	0.106	28.323
G29a	0.193	1.365	0.215	112.363
G29b	0.215	1.465	0.203	61.994
G30	0.048	0.327	0.047	14.931
DL-01-09	0.138	1.11	0.192	124.195
DI-02-09	0.142	1.095	0.167	104.958
G2	0.121	0.799	0.117	50.22
G14	0.243	1.65	0.235	58.14
G21a	0.115	0.802	0.112	28.478
G23a	0.117	0.738	0.107	34.191
G24a	0.183	1.245	0.196	56.514
G24b	0.171	1.255	0.184	41.509
G25b	0.171	1.135	0.184	50.952
G26a	0.138	0.986	0.162	33.845
G26b	0.15	1.045	0.155	36.385
G27a	0.088	0.571	0.087	28.016
G28	0.156	1.04	0.162	36.405
G30a	0.05	0.33	0.038	12.277

8.1.4 Anomalies in ironstone and carbonate

Sample	Sample Description	Eu/Eu*	Gd/Gd*	Ce/Ce*	Y/Ho	Pr/Yb
Gaa	Ironstone	1,04	1,13	1,33	49,46	0,37
Gab	Ironstone	1,15	1,11	1,29	48,44	0,50
G1	Main Dolomite	1,13	1,04	1,02	56,00	0,90
G5b	Carbonate Body	1,19	1,13	1,61	56,29	0,20
G7b	Carbonate Body	1,25	1,09	1,40	60,93	0,30
G12	Disrupted Dolomite	1,09	1,09	1,42	55,54	0,39
G17	Carbonate Diamictonite	0,95	1,01	0,96	53,00	0,77
G21	Ironstone	1,13	1,14	1,25	54,28	0,39
G22	Ironstone	1,05	1,12	1,13	54,20	0,50
G23b	Ironstone	1,11	1,13	1,24	53,01	0,39
G24	Ironstone	1,01	1,09	1,18	52,48	0,36
G25	Ironstone	1,07	1,13	1,14	51,65	0,47
G26	Ironstone	0,99	1,13	1,18	51,74	0,35
G27	Ironstone	1,01	1,08	1,04	45,09	0,64
G29b	Carbonate Body	1,10	1,02	1,18	54,95	0,45
G30	Ironstone	1,16	1,13	1,40	61,80	0,47
G2	Main Dolomite	1,13	1,04	1,25	58,80	0,78
G21a	Ironstone	1,35	1,06	1,32	60,42	0,34
G23a	Ironstone	1,27	1,19	1,39	56,16	0,50
G24a	Ironstone	1,19	1,08	1,21	51,51	0,53
G24b	Ironstone	1,24	1,09	1,18	56,17	0,33
G25b	Ironstone	1,19	1,12	1,24	55,54	0,50
G26a	Ironstone	1,20	1,14	1,25	51,82	0,37
G26b	Ironstone	1,23	1,17	1,20	52,12	0,37
G27a	Ironstone	1,16	1,14	1,05	49,30	0,67
G28	Ironstone	1,34	1,17	1,55	58,49	0,29
G30a	Ironstone	1,27	1,21	1,45	65,91	0,40

Works Cited

- Aleinikoff, J.N., Schenck, W.S., Plank, M.O., Srogi, L., Fanning, C.M., Kamo, S.L. and Bosbyshell, H., 2006. Deciphering igneous and metamorphic events in high-grade rocks of the Wilmington Complex, Delaware: Morphology, cathodoluminescence and backscattered electron zoning, and SHRIMP U-Pb geochronology of zircon and monazite. *Geological Society of America Bulletin*, 118(1-2), pp.39-64.
- Aleinikoff, J.N., Hayes, T.S., Evans, K.V., Mazdab, F.K., Pillers, R.M. and Fanning, C.M., 2012. SHRIMP U-Pb ages of xenotime and monazite from the Spar Lake red bed-associated Cu-Ag deposit, western Montana: Implications for ore genesis. *Economic Geology*, 107(6), pp.1251-1274.
- Aleinikoff, J.N., Lund, K. and Fanning, C.M., 2015. SHRIMP U-Pb and REE data pertaining to the origins of xenotime in Belt Supergroup rocks: evidence for ages of deposition, hydrothermal alteration, and metamorphism. *Canadian Journal of Earth Sciences*, 52(9), pp.722-745.
- Allen, P.A. and Etienne, J.L., 2008. Sedimentary challenge to snowball Earth. *Nature Geoscience*, 1(12), pp.817-825.
- Ali, D.O., Spencer, A.M., Fairchild, I.J., Chew, K.J., Anderton, R., Levell, B.K., Hambrey, M.J., Dove, D. and Le Heron, D.P., 2018. Indicators of relative completeness of the glacial record of the Port Askaig Formation, Garvellach Islands, Scotland. *Precambrian Research*, 319, pp.65-78.
- Anders, E. and Grevesse, N., 1989. Abundances of the elements: Meteoritic and solar. *Geochimica et Cosmochimica acta*, 53(1), pp.197-214.
- Arnaud, E. and Eyles, C.H., 2002. Catastrophic mass failure of a Neoproterozoic glacially influenced continental margin, the Great Breccia, Port Askaig Formation, Scotland. *Sedimentary Geology*, 151(3-4), pp.313-333.
- Baldwin, G.J., Turner, E.C. and Kamber, B.S., 2012. A new depositional model for glaciogenic Neoproterozoic iron formation: insights from the chemostratigraphy and basin configuration of the Rapitan iron formation. *Canadian Journal of Earth Sciences*, 49(2), pp.455-476.
- Baldwin, G.J., Turner, E.C. and Kamber, B.S., 2016. Tectonic controls on distribution and stratigraphy of the Cryogenian Rapitan iron formation, northwestern Canada. *Precambrian Research*, 278, pp.303-322.
- Baron, M. and Parnell, J., 2005. Fluid evolution in base-metal sulphide mineral deposits in the metamorphic basement rocks of southwest Scotland and Northern Ireland. *Geological Journal*, 40(1), pp.3-21.
- Basta, F.F., Maurice, A.E., Fontboté, L. and Favarger, P.Y., 2011. Petrology and geochemistry of the banded iron formation (BIF) of Wadi Karim and Um Anab, Eastern Desert, Egypt: implications for the origin of Neoproterozoic BIF. *Precambrian Research*, 187(3-4), pp.277-292.
- Bau, M., 1993. Effects of syn- and post-depositional processes on the rare-earth element distribution in Precambrian iron-formations. *European Journal of Mineralogy*, 5(2), pp.257-267.
- Bau, M. and Dulski, P., 1995. Comparative study of yttrium and rare-earth element behaviours in fluorine-rich hydrothermal fluids. *Contributions to Mineralogy and Petrology*, 119(2), pp.213-223.
- Bau, M., Dulski, P. and Moeller, P., 1995. Yttrium and holmium in South Pacific seawater: vertical distribution and possible fractionation mechanisms. *Chem. Erde*, 55(1), p.1.

- Bau, M. and Dulski, P., 1996. Distribution of yttrium and rare-earth elements in the Penge and Kuruman iron-formations, Transvaal Supergroup, South Africa. *Precambrian Research*, 79(1-2), pp.37-55
- Bau, M., Möller, P. and Dulski, P., 1997. Yttrium and lanthanides in eastern Mediterranean seawater and their fractionation during redox-cycling. *Marine Chemistry*, 56(1-2), pp.123-131.
- Bau, M. and Dulski, P., 1999. Comparing yttrium and rare earths in hydrothermal fluids from the Mid-Atlantic Ridge: implications for Y and REE behaviour during near-vent mixing and for the Y/Ho ratio of Proterozoic seawater. *Chemical Geology*, 155(1-2), pp.77-90.
- Beddoe-Stephens, B., 1990. Pressures and temperatures of Dalradian metamorphism and the andalusite–kyanite transformation in the northeast Grampians. *Scottish Journal of Geology*, 26(1), pp.3-14.
- Benn, D.I. and Prave, A.R., 2006. Subglacial and proglacial glacial tectonic deformation in the Neoproterozoic Port Askaig Formation, Scotland. *Geomorphology*, 75(1-2), pp.266-280.
- Berner, R.A., 1978. Rate control of mineral dissolution under earth surface conditions. *American Journal of Science*, 278(9), pp.1235-1252.
- Bolhar, R., Kamber, B.S., Moorbath, S., Fedo, C.M. and Whitehouse, M.J., 2004. Characterisation of early Archaean chemical sediments by trace element signatures. *Earth and Planetary Science Letters*, 222(1), pp.43-60.
- Borah, P., Hazarika, P., Mazumdar, A.C. and Rabha, M., 2019. Monazite and xenotime U–Th–Pb_{total} ages from basement rocks of the (central) Shillong–Meghalaya Gneissic Complex, Northeast India. *Journal of Earth System Science*, 128(3), p.68.
- Budzyń, B. and Sláma, J., 2019. Partial resetting of U–Pb ages during experimental fluid-induced re-equilibration of xenotime. *Lithos*, 346, p.105163.
- Caldeira, K. and Kasting, J.F., 1992. Susceptibility of the early Earth to irreversible glaciation caused by carbon dioxide clouds. *Nature*, 359(6392), pp.226-228.
- Canfield, D.E., Poulton, S.W., Knoll, A.H., Narbonne, G.M., Ross, G., Goldberg, T. and Strauss, H., 2008. Ferruginous conditions dominated later Neoproterozoic deep-water chemistry. *Science*, 321(5891), pp.949-952.
- Chang, L.L., Deer, W.A., Howie, R.A. and Zussman, J., 1996. *Rock-forming minerals*. Geological Society Publishing House.
- Cressey, M., 1996. The identification of early lead mining: environmental, archaeological and historical perspectives from Islay, Inner Hebrides, Scotland.
- Cross, A.J. and Williams, I.S., 2018. SHRIMP U–Pb–Th xenotime (YPO₄) geochronology: A novel approach for the correction of SIMS matrix effects. *Chemical Geology*, 484, pp.81-108.
- Crowley, T.J., Hyde, W.T. and Peltier, W.R., 2001. CO₂ levels required for deglaciation of a “Near-Snowball” Earth. *Geophysical Research Letters*, 28(2), pp.283-286.
- Cox, G.M., Halverson, G.P., Minarik, W.G., Le Heron, D.P., Macdonald, F.A., Bellefroid, E.J. and Strauss, J.V., 2013. Neoproterozoic iron formation: an evaluation of its temporal, environmental and tectonic significance. *Chemical Geology*, 362, pp.232-249.

- Cox, G.M., Halverson, G.P., Stevenson, R.K., Vokaty, M., Poirier, A., Kunzmann, M., Li, Z.X., Denyszyn, S.W., Strauss, J.V. and Macdonald, F.A., 2016a. Continental flood basalt weathering as a trigger for Neoproterozoic Snowball Earth. *Earth and Planetary Science Letters*, 446, pp.89-99.
- Cox, G.M., Halverson, G.P., Poirier, A., Le Heron, D., Strauss, J.V. and Stevenson, R., 2016b. A model for Cryogenian iron formation. *Earth and Planetary Science Letters*, 433, pp.280-292.
- Cherniak, D.J., 2006. Pb and rare earth element diffusion in xenotime. *Lithos*, 88(1-4), pp.1-14.
- Dahlgren, M., 2018. A sedimentological study of Cryogenian glacial-interglacial cycles recorded by the Port Askaig Tillite Formation on Islay, Scotland, B.Sc Thesis, Stockholm University, Stockholm.
- Dahlgren, M., 2020. A geochemical study of diamictite matrix in the Port Askaig Tillite Formation in western Argyll, Scotland. M.Sc. Thesis, Stockholm University, Stockholm.
- De Baar, H.J., Brewer, P.G. and Bacon, M.P., 1985. Anomalies in rare earth distributions in seawater: Gd and Tb. *Geochimica et Cosmochimica Acta*, 49(9), pp.1961-1969.
- Dempster, T.J., Rogers, G., Tanner, P.W.G., Bluck, B.J., Muir, R.J., Redwood, S.D., Ireland, T.R. and Paterson, B.A., 2002. Timing of deposition, orogenesis and glaciation within the Dalradian rocks of Scotland: constraints from U–Pb zircon ages. *Journal of the Geological Society*, 159(1), pp.83-94.
- Dillon, M. and Franke, C., 2009. Diagenetic alteration of natural Fe–Ti oxides identified by energy dispersive spectroscopy and low-temperature magnetic remanence and hysteresis measurements. *Physics of the Earth and Planetary Interiors*, 172(3-4), pp.141-156.
- Eyles, C.H. and Eyles, N., 1983. Glaciomarine model for upper Precambrian diamictites of the Port Askaig Formation, Scotland. *Geology*, 11(12), pp.692-696.
- Eyles, N. and Januszczak, N., 2004. ‘Zipper-rift’: a tectonic model for Neoproterozoic glaciations during the breakup of Rodinia after 750 Ma. *Earth-Science Reviews*, 65(1-2), pp.1-73.
- Evans, J.A., Zalasiewicz, J.A., Fletcher, I., Rasmussen, B. and Pearce, N.J., 2002. Dating diagenetic monazite in mudrocks: constraining the oil window?. *Journal of the Geological Society*, 159(6), pp.619-622.
- Fairchild, I.J. and Kennedy, M.J., 2007. Neoproterozoic glaciation in the Earth System. *Journal of the Geological Society*, 164(5), pp.895-921.
- Fairchild, I.J., Spencer, A.M., Ali, D.O., Anderson, R.P., Anderton, R., Boomer, I., Dove, D., Evans, J.D., Hambrey, M.J., Howe, J. and Sawaki, Y., 2018. Tonian-Cryogenian boundary sections of Argyll, Scotland. *Precambrian Research*, 319, pp.37-64.
- Feng, L., Huang, J., Lu, D. and Zhang, Q., 2017. Major and trace element geochemistry of the Neoproterozoic syn-glacial Fulu iron formation, South China. *Geological Magazine*, 154(6), pp.1371-1380.
- Fletcher, I.R., McNaughton, N.J., Aleinikoff, J.A., Rasmussen, B. and Kamo, S.L., 2004. Improved calibration procedures and new standards for U–Pb and Th–Pb dating of Phanerozoic xenotime by ion microprobe. *Chemical Geology*, 209(3-4), pp.295-314.
- Fletcher, I.R., Rasmussen, B. and McNaughton, N.J., 2000. SHRIMP U–Pb geochronology of authigenic xenotime and its potential for dating sedimentary basins. *Australian Journal of Earth Sciences*, 47(5), pp.845-859.
- Freitas, B.T., Warren, L.V., Boggiani, P.C., De Almeida, R.P. and Piacentini, T., 2011. Tectono-sedimentary evolution of the Neoproterozoic BIF-bearing Jacadigo Group, SW-Brazil. *Sedimentary Geology*, 238(1-2), pp.48-70.

- Gale, A., Langmuir, C.H. and Dalton, C.A., 2014. The global systematics of ocean ridge basalts and their origin. *Journal of Petrology*, 55(6), pp.1051-1082.
- Galvez, M.E., Beyssac, O., Benzerara, K., Menguy, N., Bernard, S. and Cox, S.C., 2012. Micro- and nano-textural evidence of Ti (-Ca-Fe) mobility during fluid-rock interactions in carbonaceous lawsonite-bearing rocks from New Zealand. *Contributions to Mineralogy and Petrology*, 164(5), pp.895-914.
- Gourcerol, B., Thurston, P.C., Kontak, D.J., Côté-Mantha, O. and Biczok, J., 2016. Depositional setting of Algoma-type banded iron formation. *Precambrian Research*, 281, pp.47-79.
- Gaucher, C., Sial, A.N. and Frei, R., 2015. Chemostratigraphy of Neoproterozoic banded iron formation (BIF): types, age and origin. In *Chemostratigraphy* (pp. 433-449). Elsevier.
- Halliday, A.N., Graham, C.M., Aftalion, M. and Dymoke, P., 1989. Short paper: the depositional age of the Dalradian Supergroup: U-Pb and Sm-Nd isotopic studies of the Tayvallich Volcanics, Scotland. *Journal of the Geological Society*, 146(1), pp.3-6.
- Halverson, G.P., Poitrasson, F., Hoffman, P.F., Nédélec, A., Montel, J.M. and Kirby, J., 2011. Fe isotope and trace element geochemistry of the Neoproterozoic syn-glacial Rapitan iron formation. *Earth and Planetary Science Letters*, 309(1-2), pp.100-112.
- Hambrey, M.J. and Harland, W.B. eds., 2011. *Earth's pre-Pleistocene glacial record*. Cambridge University Press.
- Harland, W.B., 1964. Critical evidence for a great infra-Cambrian glaciation. *Geologische Rundschau*, 54(1), pp.45-61.
- Harrison, T.M., Catlos, E.J. and Montel, J.M., 2002. U-Th-Pb dating of phosphate minerals. *Reviews in Mineralogy and Geochemistry*, 48(1), pp.524-558.
- Hawkings, J.R., Wadham, J.L., Tranter, M., Raiswell, R., Benning, L.G., Statham, P.J., Tedstone, A., Nienow, P., Lee, K. and Telling, J., 2014. Ice sheets as a significant source of highly reactive nanoparticulate iron to the oceans. *Nature communications*, 5(1), pp.1-8.
- Henderson-Sellers, A. and Wilson, M.F., 1983. Albedo observations of the earth's surface for climate research. *Philosophical Transactions of the Royal Society of London. Series A, Mathematical and Physical Sciences*, 309(1508), pp.285-294.
- Hetherington, C.J., Jercinovic, M.J., Williams, M.L. and Mahan, K., 2008. Understanding geologic processes with xenotime: Composition, chronology, and a protocol for electron probe microanalysis. *Chemical Geology*, 254(3-4), pp.133-147.
- Hoffman, P.F., Kaufman, A.J., Halverson, G.P. and Schrag, D.P., 1998. A Neoproterozoic snowball earth. *Science*, 281(5381), pp.1342-1346.
- Hoffman, P.F., Macdonald, F.A. and Halverson, G.P., 2011. Chemical sediments associated with Neoproterozoic glaciation: iron formation, cap carbonate, barite and phosphorite. *Geological Society, London, Memoirs*, 36(1), pp.67-80.
- Hoffman, P.F., Abbot, D.S., Ashkenazy, Y., Benn, D.I., Brocks, J.J., Cohen, P.A., Cox, G.M., Creveling, J.R., Donnadieu, Y., Erwin, D.H. and Fairchild, I.J., 2017. Snowball Earth climate dynamics and Cryogenian geology-geobiology. *Science Advances*, 3(11), p.e1600983.
- Hood, A. and Wallace, M.W., 2015. Extreme ocean anoxia during the Late Cryogenian recorded in reefal carbonates of Southern Australia. *Precambrian Research*, 261, pp.96-111.

- Hoareau, G., Odonne, F., Debroas, E.J., Maillard, A., Monnin, C. and Callot, P., 2009. Dolomitic concretions in the Eocene Sobrarbe delta (Spanish Pyrenees): Fluid circulation above a submarine slide scar infilling. *Marine and Petroleum Geology*, 26(5), pp.724-737.
- Isley, A.E. and Abbott, D.H., 1999. Plume-related mafic volcanism and the deposition of banded iron formation. *Journal of Geophysical Research: Solid Earth*, 104(B7), pp.15461-15477.
- Ilyin, A.V., 2009. Neoproterozoic banded iron formations. *Lithology and Mineral Resources*, 44(1), p.78.
- James, H.L., 1954. Sedimentary facies of iron-formation. *Economic Geology*, 49(3), pp.235-293.
- Kamber, B.S., Greig, A. and Collerson, K.D., 2005. A new estimate for the composition of weathered young upper continental crust from alluvial sediments, Queensland, Australia. *Geochimica et Cosmochimica Acta*, 69(4), pp.1041-1058.
- Kato, Y., Yamaguchi, K.E. and Ohmoto, H., 2006. Rare earth elements in Precambrian banded iron formations: Secular changes of Ce and Eu anomalies and evolution of atmospheric oxygen. *Evolution of Early Earth's Atmosphere, Hydrosphere, and Biosphere: Constraints from Ore Deposits*, 198, p.269.
- Kilburn, C., Shackleton, R.M. and Pitcher, W.S., 1965. The stratigraphy and origin of the Portaskaig Boulder Bed series (Dalradian). *Geological Journal*, 4(2), pp.343-360.
- Kim, K., Choi, W., Hoffmann, M.R., Yoon, H.I. and Park, B.K., 2010. Photoreductive dissolution of iron oxides trapped in ice and its environmental implications. *Environmental science & technology*, 44(11), pp.4142-4148.
- Kirschvink, J.L., 1992. Late Proterozoic low-latitude global glaciation: the snowball Earth.
- Klein, C. and Beukes, N.J., 1993. Sedimentology and geochemistry of the glaciogenic late Proterozoic Rapitan iron-formation in Canada. *Economic Geology*, 88(3), pp.542-565.
- Klein, C., 2005. Some Precambrian banded iron-formation (BIFs) from around the world: Their age, geologic setting, mineralogy, metamorphism, geochemistry, and origins. *American Mineralogist*, 90(10), pp.1473-1499.
- Korotev, R.L., 1996. On the relationship between the Apollo 16 ancient regolith breccias and feldspathic fragmental breccias, and the composition of the prebasin crust in the Central Highlands of the Moon. *Meteoritics & Planetary Science*, 31(3), pp.403-412.
- Kositcin, N., McNaughton, N.J., Griffin, B.J., Fletcher, I.R., Groves, D.I. and Rasmussen, B., 2003. Textural and geochemical discrimination between xenotime of different origin in the Archaean Witwatersrand Basin, South Africa. *Geochimica et Cosmochimica Acta*, 67(4), pp.709-731.
- Lan, Z.W., Chen, Z.Q., Li, X.H., Li, B. and Adams, D., 2013. Hydrothermal origin of the Paleoproterozoic xenotime from the King Leopold Sandstone of the Kimberley group, Kimberley, NW Australia: implications for a ca 1.7 Ga far-field hydrothermal event. *Australian Journal of Earth Sciences*, 60(4), pp.497-508.
- Lang, X., Chen, J., Cui, H., Man, L., Huang, K.J., Fu, Y., Zhou, C. and Shen, B., 2018. Cyclic cold climate during the Nantuo glaciation: evidence from the Cryogenian Nantuo Formation in the Yangtze Block, South China. *Precambrian Research*, 310, pp.243-255.
- Lan, Z., Li, X.H., Sano, Y., Takahata, N., Kagoshima, T., Zhang, S., Zhang, G., Liao, X., Tang, X., Gu, L. and Mao, Q., 2019. Two kinds of authigenic xenotime overgrowths in response to an Early Paleozoic tectonothermal event in South China. *Journal of Asian Earth Sciences*, 172, pp.423-442.

- Lawrence, M.G., Greig, A., Collerson, K.D. and Kamber, B.S., 2006a. Rare earth element and yttrium variability in South East Queensland waterways. *Aquatic Geochemistry*, 12(1), pp.39-72.
- Lawrence, M.G. and Kamber, B.S., 2006b. The behaviour of the rare earth elements during estuarine mixing—revisited. *Marine Chemistry*, 100(1-2), pp.147-161.
- Lechte, M.A. and Wallace, M.W., 2015. Sedimentary and tectonic history of the Holowilena Ironstone, a Neoproterozoic iron formation in South Australia. *Sedimentary Geology*, 329, pp.211-224.
- Lechte, M. and Wallace, M., 2016. Sub-ice shelf ironstone deposition during the Neoproterozoic Sturtian glaciation. *Geology*, 44(11), pp.891-894.
- Lechte, M.A., Wallace, M.W., van Smeerdijk Hood, A. and Planavsky, N., 2018. Cryogenian iron formations in the glaciogenic Kingston Peak Formation, California. *Precambrian Research*, 310, pp.443-462.
- Lechte, M.A., Wallace, M.W. and Hoffmann, K.H., 2019. Glacio-marine iron formation deposition in a c. 700 Ma glaciated margin: insights from the Chuos Formation, Namibia. *Geological Society, London, Special Publications*, 475(1), pp.9-34.
- Le Heron, D.P., Eyles, N. and Busfield, M.E., 2020. The Laurentian Neoproterozoic Glacial Interval: reappraising the extent and timing of glaciation. *Austrian Journal of Earth Sciences*, 113(1), pp.59-70.
- Li, Z.X., Bogdanova, S.V., Collins, A.S., Davidson, A., De Waele, B., Ernst, R.E., Fitzsimons, I.C.W., Fuck, R.A., Gladkochub, D.P., Jacobs, J. and Karlstrom, K.E., 2008. Assembly, configuration, and break-up history of Rodinia: a synthesis. *Precambrian research*, 160(1-2), pp.179-210.
- Li, Q.L., Li, X.H., Lan, Z.W., Guo, C.L., Yang, Y.N., Liu, Y. and Tang, G.Q., 2013a. Monazite and xenotime U–Th–Pb geochronology by ion microprobe: dating highly fractionated granites at Xihuashan tungsten mine, SE China. *Contributions to Mineralogy and Petrology*, 166(1), pp.65-80.
- Li, Z.X., Evans, D.A. and Halverson, G.P., 2013b. Neoproterozoic glaciations in a revised global palaeogeography from the breakup of Rodinia to the assembly of Gondwanaland. *Sedimentary Geology*, 294, pp.219-232.
- Li, L.X., Zi, J.W., Meng, J., Li, H.M., Rasmussen, B., Sheppard, S., Wilde, S.A. and Li, Y.H., 2020. Using In Situ Monazite and Xenotime U-Pb Geochronology to Resolve the Fate of the “Missing” Banded Iron Formation-Hosted High-Grade Hematite Ores of the North China Craton. *Economic Geology*, 115(1), pp.189-204.
- Majka, J., Mazur, S., Manecki, M., Czerny, J. and Holm, D.K., 2008. Late Neoproterozoic amphibolite-facies metamorphism of a pre-Caledonian basement block in southwest Wedel Jarlsberg Land, Spitsbergen: New evidence from U–Th–Pb dating of monazite. *Geological Magazine*, 145(6), pp.822-830
- Mavotchy, N.O., El Albani, A., Trentesaux, A., Fontaine, C., Pierson-Wickmann, A.C., Boulvais, P., Riboulleau, A., Pemba, L.N., Pambo, F. and Gauthier-Lafaye, F., 2016. The role of the early diagenetic dolomitic concretions in the preservation of the 2.1-Ga paleoenvironmental signal: The Paleoproterozoic of the Franceville Basin, Gabon. *Comptes Rendus Géoscience*, 348(8), pp.609-618.
- Mikucki, J.A., Pearson, A., Johnston, D.T., Turchyn, A.V., Farquhar, J., Schrag, D.P., Anbar, A.D., Priscu, J.C. and Lee, P.A., 2009. A contemporary microbially maintained subglacial ferrous "ocean". *Science*, 324(5925), pp.397-400.
- Millero, F.J., Sotolongo, S. and Izaguirre, M., 1987. The oxidation kinetics of Fe (II) in seawater. *Geochimica et Cosmochimica Acta*, 51(4), pp.793-801.

- Milodowski, A.E. and Zalasiewicz, J.A., 1991. Redistribution of rare earth elements during diagenesis of turbidite/hemipelagite mudrock sequences of Llandovery age from central Wales. *Geological Society, London, Special Publications*, 57(1), pp.101-124.
- McNaughton, N.J., Rasmussen, B. and Fletcher, I.R., 1999. SHRIMP uranium-lead dating of diagenetic xenotime in siliciclastic sedimentary rocks. *Science*, 285(5424), pp.78-80.
- McNaughton, N.J. and Rasmussen, B., 2018. Geochemical characterisation of xenotime formation environments using U-Th. *Chemical Geology*, 484, pp.109-119.
- Moore, J.K. and Braucher, O., 2008. Sedimentary and mineral dust sources of dissolved iron to the world ocean. *Biogeosciences*, 5(3), pp.631-656.
- Morford, J.L., Martin, W.R., François, R. and Carney, C.M., 2009. A model for uranium, rhenium, and molybdenum diagenesis in marine sediments based on results from coastal locations. *Geochimica et Cosmochimica Acta*, 73(10), pp.2938-2960.
- North American Commission on Stratigraphic Nomenclature, 2005. North American stratigraphic code. *AAPG Bulletin*, 89(11), pp.1547-1591.
- Pitcairn, I.K., Skelton, A.D., Broman, C., Arghe, F. and Boyce, A., 2010. Structurally focused fluid flow during orogenesis: the Islay Anticline, SW Highlands, Scotland. *Journal of the Geological Society*, 167(4), pp.659-674.
- Planavsky, N., Bekker, A., Rouxel, O.J., Kamber, B., Hofmann, A., Knudsen, A. and Lyons, T.W., 2010. Rare earth element and yttrium compositions of Archean and Paleoproterozoic Fe formations revisited: new perspectives on the significance and mechanisms of deposition. *Geochimica et Cosmochimica Acta*, 74(22), pp.6387-6405.
- Prave, A.R., 1999. The Neoproterozoic Dalradian Supergroup of Scotland: an alternative hypothesis. *Geological Magazine*, 136(6), pp.609-617.
- Rasmussen, B., Buick, R. and Taylor, W.R., 1998. Removal of oceanic REE by authigenic precipitation of phosphatic minerals. *Earth and Planetary Science Letters*, 164(1-2), pp.135-149.
- Rasmussen, B., Fletcher, I.R. and McNaughton, N.J., 2001. Dating low-grade metamorphic events by SHRIMP U-Pb analysis of monazite in shales. *Geology*, 29(10), pp.963-966.
- Rasmussen, B. and Fletcher, I.R., 2002. Indirect dating of mafic intrusions by SHRIMP U-Pb analysis of monazite in contact metamorphosed shale: an example from the Palaeoproterozoic Capricorn Orogen, Western Australia. *Earth and Planetary Science Letters*, 197(3-4), pp.287-299.
- Rasmussen, B., 2005. Radiometric dating of sedimentary rocks: the application of diagenetic xenotime geochronology. *Earth-Science Reviews*, 68(3-4), pp.197-243.
- Rasmussen, B., Fletcher, I.R., Muhling, J.R., Thorne, W.S. and Broadbent, G.C., 2007. Prolonged history of episodic fluid flow in giant hematite ore bodies: evidence from in situ U-Pb geochronology of hydrothermal xenotime. *Earth and Planetary Science Letters*, 258(1-2), pp.249-259.
- Rasmussen, B., Fletcher, I.R., Muhling, J.R. and Wilde, S.A., 2010. In situ U-Th-Pb geochronology of monazite and xenotime from the Jack Hills belt: Implications for the age of deposition and metamorphism of Hadean zircons. *Precambrian Research*, 180(1-2), pp.26-46.
- Rasmussen, B., Fletcher, I.R. and Muhling, J.R., 2011. Response of xenotime to prograde metamorphism. *Contributions to Mineralogy and Petrology*, 162(6), pp.1259-1277.

- Rooney, A.D., Chew, D.M. and Selby, D., 2011. Re–Os geochronology of the Neoproterozoic–Cambrian Dalradian Supergroup of Scotland and Ireland: implications for Neoproterozoic stratigraphy, glaciations and Re–Os systematics. *Precambrian Research*, 185(3-4), pp.202-214.
- Rooney, A.D., Macdonald, F.A., Strauss, J.V., Dudás, F.Ö., Hallmann, C. and Selby, D., 2014. Re-Os geochronology and coupled Os-Sr isotope constraints on the Sturtian snowball Earth. *Proceedings of the National Academy of Sciences*, 111(1), pp.51-56.
- Rubatto, D., Putlitz, B., Gauthiez-Putallaz, L., Crépisson, C., Buick, I.S. and Zheng, Y.F., 2014. Measurement of in-situ oxygen isotope ratios in monazite by SHRIMP ion microprobe: Standards, protocols and implications. *Chemical geology*, 380, pp.84-96.
- Sawaki, Y., Kawai, T., Shibuya, T., Tahata, M., Omori, S., Komiya, T., Yoshida, N., Hirata, T., Ohno, T., Windley, B.F. and Maruyama, S., 2010. $^{87}\text{Sr}/^{86}\text{Sr}$ chemostratigraphy of Neoproterozoic Dalradian carbonates below the Port Askaig glaciogenic Formation, Scotland. *Precambrian Research*, 179(1-4), pp.150-164.
- Scherrer, N.C., Engi, M., Gnos, E., Jakob, V. and Liechti, A., 2000. Monazite analysis; from sample preparation to microprobe age dating and REE quantification. *Schweizerische mineralogische und petrographische Mitteilungen*, 80(1), pp.93-105.
- Schrag, D.P., Berner, R.A., Hoffman, P.F. and Halverson, G.P., 2002. On the initiation of a snowball Earth. *Geochemistry, Geophysics, Geosystems*, 3(6), pp.1-21.
- Shields, G. and Stille, P., 2001. Diagenetic constraints on the use of cerium anomalies as palaeoseawater redox proxies: an isotopic and REE study of Cambrian phosphorites. *Chemical Geology*, 175(1-2), pp.29-48.
- Skelton, A.D., Graham, C.M. and Bickle, M.J., 1995. Lithological and structural controls on regional 3-D fluid flow patterns during greenschist facies metamorphism of the Dalradian of the SW Scottish Highlands. *Journal of Petrology*, 36(2), pp.563-586.
- Skelton, A., Lewerentz, A., Kleine, B., Webster, D. and Pitcairn, I., 2015. Structural channelling of metamorphic fluids on Islay, Scotland: implications for paleoclimatic reconstruction. *Journal of Petrology*, 56(11), pp.2145-2172.
- Spence, G.H., Le Heron, D.P. and Fairchild, I.J., 2016. Sedimentological perspectives on climatic, atmospheric and environmental change in the Neoproterozoic Era. *Sedimentology*, 63(2), pp.253-306.
- Spencer, A.M., 1971. Late Precambrian glaciation in Scotland: *Geol. Soc. London, Mem*, 6.
- Sverjensky, D.A., 1984. Europium redox equilibria in aqueous solution. *Earth and Planetary Science Letters*, 67(1), pp.70-78.
- Taylor, S.R. and McLennan, S.M., 1985. The continental crust: its composition and evolution.
- Thomson, J., 1877. XIII. On the Geology of the Island of Islay. *Transactions of the Geological Society of Glasgow*, 5(2), pp.200-222.
- Trendall, A.F. and Morris, R.C. eds., 1983. *Iron-formation: facts and problems*. Elsevier.
- Vallini, D.A., Rasmussen, B., KRAPEŽ, B., Fletcher, I.R. and Mcnaughton, N.J., 2005. Microtextures, geochemistry and geochronology of authigenic xenotime: constraining the cementation history of a Palaeoproterozoic metasedimentary sequence. *Sedimentology*, 52(1), pp.101-122.
- Webster, D., Anderton, R. & Skelton, A., 2017, A guide to the geology of Islay (second edition): Ringwood Publishing, Glasgow, 178 p.

- Weill, D.F. and Drake, M.J., 1973. Europium anomaly in plagioclase feldspar: experimental results and semiquantitative model. *Science*, 180(4090), pp.1059-1060.
- Williams, M.L., Jercinovic, M.J. and Terry, M.P., 1999. Age mapping and dating of monazite on the electron microprobe: Deconvoluting multistage tectonic histories. *Geology*, 27(11), pp.1023-1026.
- Wu, C., Yang, T., Shields, G.A., Bian, X., Gao, B., Ye, H. and Li, W., 2020. Termination of Cryogenian ironstone deposition by deep ocean euxinia. *Geochemical Perspectives Letters*, 15, pp.1-5.
- Ye, Y., Wang, H., Zhai, L., Wang, X., Wu, C. and Zhang, S., 2018. Contrasting Mo–U enrichments of the basal Datangpo Formation in South China: Implications for the Cryogenian interglacial ocean redox. *Precambrian Research*, 315, pp.66-74. ating composition and chronology. *Annu. Rev. Earth Planet. Sci.*, 35, pp.137-175.
- Xu, D.R., Wang, Z.L., Chen, H.Y., Hollings, P., Jansen, N.H., Zhang, Z.C. and Wu, C.J., 2014. Petrography and geochemistry of the Shilu Fe–Co–Cu ore district, South China: implications for the origin of a Neoproterozoic BIF system. *Ore Geology Reviews*, 57, pp.322-350.
- Zhang, J. and Nozaki, Y., 1996. Rare earth elements and yttrium in seawater: ICP-MS determinations in the East Caroline, Coral Sea, and South Fiji basins of the western South Pacific Ocean. *Geochimica et Cosmochimica Acta*, 60(23), pp.4631-4644
- Zhu, X.K., O'Nions, R.K. and Gibb, A.J., 1998. SIMS analysis of U–Pb isotopes in monazite: matrix effects. *Chemical Geology*, 144(3-4), pp.305-312.